A Study of the Effects of Oxygen on Void Stability in an Ion-Irradiated Austenitic Stainless Steel

L.E. Seitzman

April 1988

UWFDM-762

Ph.D. thesis.

FUSION TECHNOLOGY INSTITUTE

UNIVERSITY OF WISCONSIN

MADISON WISCONSIN

A Study of the Effects of Oxygen on Void Stability in an Ion-Irradiated Austenitic Stainless Steel

L.E. Seitzman

Fusion Technology Institute
University of Wisconsin
1500 Engineering Drive
Madison, WI 53706

http://fti.neep.wisc.edu

April 1988

UWFDM-762

Ph.D. thesis.

A STUDY OF THE EFFECTS OF OXYGEN ON VOID STABILITY IN AN ION-IRRADIATED AUSTENITIC STAINLESS STEEL

BY

LARRY EDWARD SEITZMAN

A thesis submitted in partial fulfillment
of the requirement for the degree of

DOCTOR OF PHILOSOPHY

(Nuclear Engineering and Engineering Physics)

at the
UNIVERSITY OF WISCONSIN-MADISON

1988

A STUDY OF THE EFFECTS OF OXYGEN ON VOID STABILITY IN AN ION-IRRADIATED AUSTENITIC STAINLESS STEEL

Larry Edward Seitzman

Under the Supervision of Professor Gerald L. Kulcinski

A model investigating the role of oxygen in void nucleation is proposed and tested. A comparison of the energetic stability of a void versus other vacancy cluster species in type 316 stainless steel is made. It is calculated that the void is energetically unstable until the surface energy is lowered to 1 J/m^2. The required decrease in surface energy is calculated to occur when about a monolayer of oxygen adsorbs to the void embryo surface. The driving force for adsorption is calculated and the partitioning of oxygen from solution is determined. An initial concentration of 4 to 5 appm of unbound oxygen in solution is calculated to result in the stabilization of a high density ($\sim 10^{22}/m^3$) of voids over the temperature regime of 550 to 650°C.

This model is tested using 15 MeV Ni-ion irradiation of an Fe-17Ni-13Cr alloy from 550 to 650°C with room temperature oxygen preimplantation performed in some cases. The irradiated specimens are examined in cross-section. As little as 10 appm injected oxygen substantially increases the void density in this steel containing 160 appm residual oxygen. Oxygen implanted specimens generally show a void density increase of one to two orders of magnitude compared to

control specimens. Void density also appears to be mainly a function of injected oxygen concentration in the preimplanted alloy. Irradiation temperature only influences void diameter in these specimens. A region depleted of observable voids occurs in the oxygen implanted zone when 300 appm oxygen or more is injected. It is suggested that void nucleation is suppressed by an increase in the vacancy sink density when such high oxygen concentrations are present. Injecting oxygen also strongly affects the temperature dependence of the near-surface void denuded zone width.

This study indicates that the oxygen content is an important parameter in the swelling response of ion-irradiated steel and must be taken into account in future studies.

APPROVED:

April 4, 1988
Date

Professor Gerald L. Kulcinski
Nuclear Engineering Department

ACKNOWLEDGEMENTS

The path taken that has led to this thesis has crossed, and sometimes recrossed, the paths of many others. The individuals whom I met at these intersections have contributed to my growth, educational and otherwise. To all of these people I owe my thanks.

The guidance and support of Professor Gerald L. Kulcinski was instrumental and is greatly appreciated. Professor R.A. Dodd has provided invaluable advice and aid along the way. The advice and ideas of Dr. W.G. Wolfer have also been extremely helpful to me in my academic endeavors.

I would like to thank Dr. A. West and Mr. R. Casper for the time and talent they have devoted in teaching me electron microscopy. The technical support from the Wisconsin Nuclear Physics group during the ion irradiations is also appreciated. I would like to thank especially Dr. J.H. Billen, Mr. R. Schmidt, Mr. T. Rebholtz, and Mr. T. Finnesy for their assistance and technical advice. The advice of Mr. M. Mathias was very useful regarding electroplating.

The completion of this thesis would have required an additional decade, at least, without the aid of the Wisconsin Radiation Damage group, past and present. I would like to acknowledge the help of Dr. S.K. McLaurin, Dr. R.W. Knoll, Dr. D.B. Bullen, Dr. D.L. Plumton, Dr. C.D. Croessman, Dr. J.J. Kai, Mr. J.H. Liang, and Mr. M.H. Song. A special thank you is given to Mr. D.H. Plantz, Mr. D.J. Pertzborn, Ms. R.D. Griffin, Mr. S.H. Han, and Mr. L.M. Wang for their contributions to my work. This thesis follows directly from

the work of Dr. S.J. Zinkle and Dr. R.L. Sindelar. I owe immeasurable gratitude to these two individuals.

I would like to acknowledge Mr. D. Bruggink and Ms. H.A. Fack for their assistance in manuscript and graphics preparation. Thank you, also, to E. DuCharme who typed this thesis.

Finally, it is to friends and family that I give my last and largest thank you. The friendship of Dr. R.L. Sindelar, Dr. M.D. Carter, Dr. K.D. Siebert, Mr. M.K. Farrens, Ms. S.N. Farrens, and Mr. A.F. Smith have brought me through the difficult periods and have brought joy to my life. There is no way to express enough appreciation for the love and support of my brothers and sister and their spouses. Thank you. Finally, I dedicate this work to my parents, Leonard and Gloria Seitzman, for their love, support, and continuing faith in me.

This work was supported by the United States Department of Energy.

TABLE OF CONTENTS

LIST OF FIGURES

LIST OF TABLES

CHAPTER 1

INTRODUCTION

The problem of swelling due to cavity formation in irradiated metals has existed since 1967, when Cawthorne and Fulton [1] reported voids in stainless steel. Since then theories have been developed and experiments performed in an effort to eliminate swelling as a factor in nuclear materials performance. Recent evidence [2] indicates that for austenitic alloys, the swelling behavior can be separated into two distinct stages, the transient and the steady state. The steady state swelling rate is about 1%/dpa in irradiated steels [3] and for some nuclear applications, an accumulated dose of several hundred dpa is expected [4]. If an austenitic alloy is to be used in these kinds of applications, it is clear that the transient regime of swelling must be extended to very high doses. This can only be accomplished by a thorough understanding of the details of void formation.

In order to achieve this kind of understanding, each of the assumptions used in modelling void formation must be studied critically. For many years, void nucleation theories have required the use of unrealistic surface energy values in order to obtain realistic nucleation rates. This study attempts to deal with the physical basis for making such an assumption.

Oxygen has been known to promote void formation for many years [5-6]. Despite this knowledge and the fact that residual oxygen

occurs in many metals, the study of oxygen effects on swelling has been sparse. This thesis attempts to clarify the role oxygen plays in irradiated austenitic stainless steel.

First, the traditional void nucleation models are reviewed with an emphasis on the surface energy values chosen for the implementation of these theories. Next, a model is proposed to explain how these surface energies may be achieved in austenitic stainless steel. Specifically, the role oxygen plays in affecting the surface energy is examined. Oxygen is determined to be an agent that stabilizes void embryos against collapse by adsorption to the embryo surface. Small concentrations of oxygen (< 10 appm) are calculated to be capable of stabilizing a high void density (~ $10^{22}/m^3$). This model is then tested by 15 MeV Ni-ion irradiation of an Fe-17 Ni-13 Cr alloy over the temperature range 550 to 650°C. Several irradiated specimens receive a prior implantation of oxygen at room temperature up to a concentration of 1000 appm. A comparison of the resultant cavitation in the implanted and unimplanted specimens is made with respect to the derived model.

References for Chapter 1

1. C. Cawthorne and E.J. Fulton, Nature 216 (1967) 575-576.
2. F.A. Garner, J. Nucl. Mat., 122 & 123 (1984) 459-471.
3. B.B. Glasgow and W.G. Wolfer, "Modeling of Void Swelling in Irradiated Steels," in Effects of Radiation on Materials: Twelfth International Symposium, ASTM STP 870 (1985) 453-467.

4. B. Badger, et al., "Progress in Fusion Research, 1978-1982," UWFDM-496 (1983).

5. K.H. Westmacott, Phil. Mag. 24 (1971) 475-480.

6. R.S. Nelson, J.A. Hudson, D.J. Mazey, G.P. Walters, and T.M. Williams, "Void Formation in Metals During Ion Bombardment," in Radiation Induced Voids in Metals, J.W. Corbett and L.C. Ianiello, Eds. (1972) 31-83.

CHAPTER 2

RADIATION DAMAGE THEORY

The interaction of a metal with sufficiently energetic particle irradiation can result in the disturbance of the metal lattice. This disturbance takes the form of the creation of Frenkel pairs. If an incident particle strikes a lattice atom and, subsequently, transfers great enough energy to the lattice atom ($\gtrsim$ 20 eV), the lattice atom will depart from its original position and lodge elsewhere in the lattice. The relocated atom will occupy an interstitial site in the lattice and a vacancy will be left at the initial position. Two point defects, the interstitial and the vacancy, are thus formed by the collision of the irradiated particle with the metal lattice. This pair of point defects is called a Frenkel pair. An equilibrium number of point defects also exists in an unirradiated metal at a given temperature. Frenkel pairs formed by irradiation increase the number of point defects above the equilibrium value and, thereby, increase the free energy of the metal.

In order to reduce the free energy of the metal, the number of point defects needs to be reduced to the equilibrium value. This can be accomplished by the recombination of Frenkel pairs or the annihilation of point defects at defect sinks. Sinks include grain boundaries, dislocations, precipitates, loops, voids, and bubbles. If the temperature is sufficiently low to preclude atomic mobility, then no such annihilation or recombination occurs because the point

defects are immobile as well. At temperatures corresponding to stage I of isochronal recovery, usually around 0.04 T/T_M (T_M being the melting temperature in degrees absolute), the interstitial becomes mobile and will migrate to sinks. At stage III of recovery, typically ranging from 0.14 to 0.30 T/T_M, the vacancy is capable of migration and, therefore, of removal to sinks. Once the vacancies become mobile, the potential for vacancy agglomeration exists. An accumulation of vacancies is termed a void. The physics of vacancy clustering into voids is considered in this chapter.

A. Point Defect Generation

When a bombarding particle impinges upon and dislodges a lattice atom such that the dislodged atom creates additional Frenkel defects, that lattice atom is termed a primary knock-on atom or PKA. A PKA can be created by neutron, ion, or high-energy electron irradiation. Once a PKA is born, it travels through a metal as an ion losing energy by electronic and nuclear processes. The nuclear collisions usually give rise to Frenkel pairs and, quite possibly, higher order knock-ons. As the PKA slows, the ratio of nuclear to electronic energy losses is increased. The original bombarding particle may continue creating PKAs until it is depleted of most of its kinetic energy. The number of PKAs and the density of the resultant cascades depends on the mass and energy of the bombarding species and on the target material. A great deal of previous work has gone into

calculating all the factors involved. A general description of the basic physics involved is given by Robinson [1].

The comparison of the number of defects produced by different bombarding species can be assessed by using the modified Kinchen-Pease model of Torrens and Robinson [2]

$$N_d(x) = \frac{\Phi}{N} \frac{\kappa\, S_D(x)}{2E_d} \tag{2.1}$$

where $N_d(x)$ is the number of displacements per atom per second (dpa/sec) at a distance x in the target, Φ is the incident particle flux, N is the target atom number density, κ is the displacement efficiency, $S_d(x)$ is the damage energy (the amount of PKA energy available for damage) and E_d is a sharp isotropic displacement threshold energy for a target atom. The value of κ traditionally used for all forms of irradiation is $\kappa = 0.8$. This value is correct for high energy electron irradiation but recent evaluation [3] reveals that $\kappa \sim 0.3$ is a more realistic value for high energy neutron and ion irradiation. For $N_d(x) = 1$ dpa/sec, every atom in the target is being dislodged, on the average, from its lattice position once every second.

Evaluation of the damage energy, $S_d(x)$, is a complicated task involving the determination of the nuclear and electronic slowing-down processes. The Lindhard, Scharff, and Schiott (LSS) theory [4] is an early attempt to model the slowing down of an energetic ion in a solid target. A Thomas-Fermi atom with a screened Coulomb

potential is used to calculate nuclear stopping and an electronic stopping formula with an $E^{1/2}$ dependence is developed. Manning and Mueller [5] use LSS theory to calculate $S_d(x)$. Brice also uses LSS theory to evaluate $S_d(x)$ [6]. Recently, work has been undertaken to determine $S_d(x)$ with Monte Carlo calculations [7] and Figure 2.1 is an example of $N_d(x)t$ versus depth and range versus depth for 15 MeV nickel ions and 6 MeV oxygen ions on a austenitic steel ternary using the Monte Carlo approach. Figure 2.1a compares the range of injected nickel with the damage produced. Figure 2.1b plots the concentration of deposited oxygen versus depth as well as the damage profile of bombarding nickel ions. These results agree closely with similar calculations using the BRICE code.

The parameters used in evaluating the dpa equation for austenitic stainless steel are $\kappa = 0.8$ and $E_d = 40$ eV. As noted earlier $\kappa = 0.3$ is more appropriate for ion irradiation, but for the past decade most ion bombardment studies have used $\kappa = 0.8$. Therefore, for comparison with other data $\kappa = 0.8$ is used for the rest of this thesis. The displacement energy value is taken from the ASTM standard [8].

The evaluation of equation (2.1) gives the total number of Frenkel pairs generated. But this is not the same as the concentration of point defects under irradiation. Ion and neutron irradiation results in a heterogeneous distribution of localized damage, known as cascades [1]. Cascades result from the short range of higher-order knock-on atoms. Annealing within the cascades causes recombination

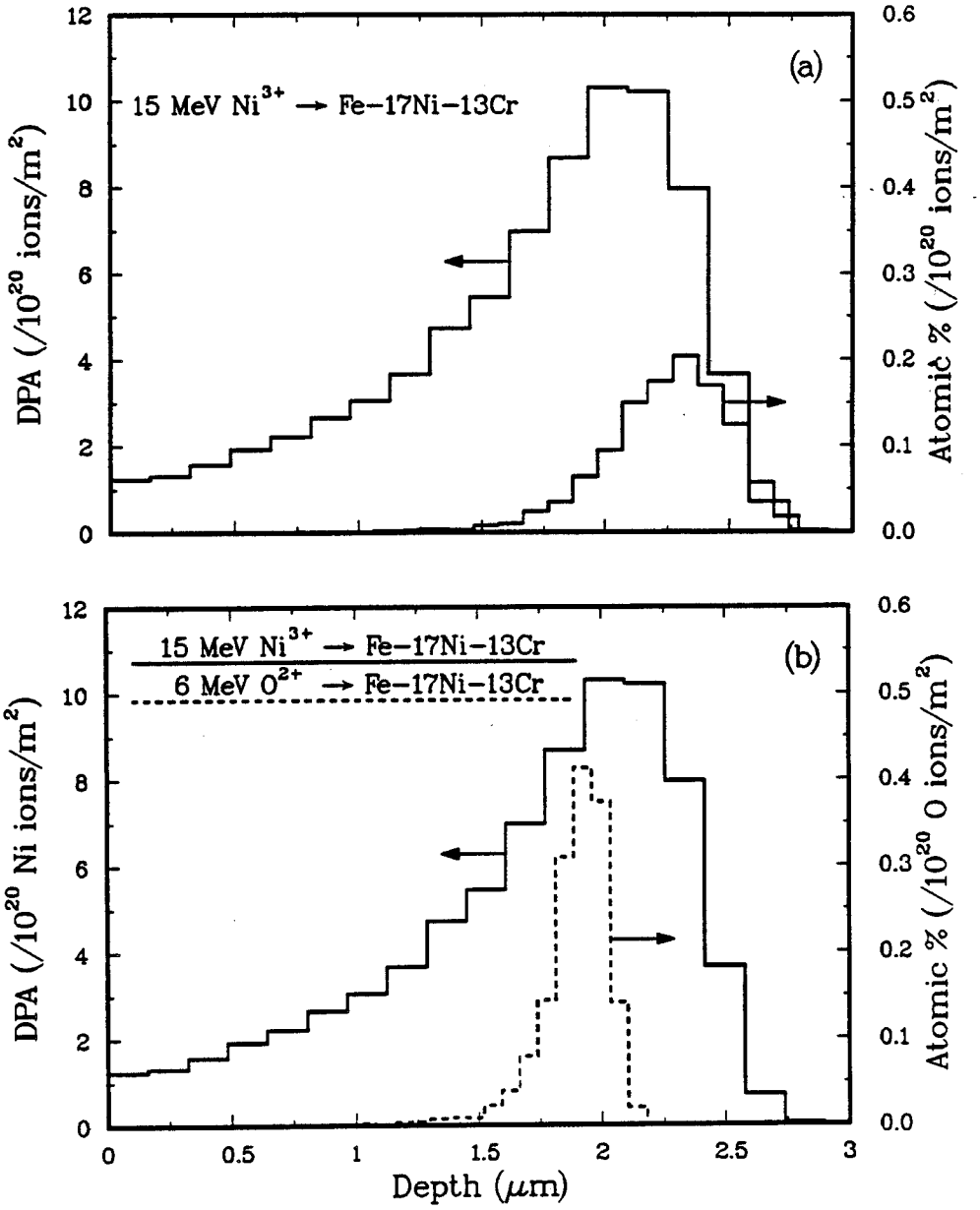

Figure 2.1. Calculated damage profile of 15 MeV Ni and ranges of (a) incident Ni and (b) implanted O in Fe–17Ni–13Cr with 1000 ion histories.

of the majority of Frenkel defects [9]. In order to calculate the concentration of point defects in an irradiated material, the following rate equations are typically used [10]:

$$\frac{\partial C_v}{\partial t} = \nabla \cdot \left(D_v \nabla C_v + \frac{D_v C_v}{kT} \nabla U_v\right) + G_v - RC_v C_i - K_v C_v \quad (2.2)$$

and

$$\frac{\partial C_i}{\partial t} = \nabla \cdot \left(D_i \nabla C_i + \frac{D_i C_i}{kT} \nabla U_i\right) + G_i - RC_v C_i - K_i C_i \quad (2.3)$$

where v denotes vacancies and i interstitials, C's are concentrations, K's are reaction rate constants detailing losses to sinks, D's are diffusion coefficients, U's are interaction energies of point defects with the discrete sink, kT is Boltzmann's constant times absolute temperature, G's are the surviving point defect generation rates per unit volume, and t is time. Once the point defect concentrations are known, defect cluster nucleation and growth can be determined.

B. Void Formation Theory

Void formation occurs because of the coalescence of single vacancies into a stable cluster. The stability of the cluster is defined by free energy. A stable void will increase the total free energy of the solid through the loss of a vacancy from the void to the matrix. Thus a stable void should not shrink. Several theories

exist which attempt to model the methods by which voids form. Classical nucleation theory, chemical reaction rate theory, and time-dependent stochastic evolution theory are the three primary classifications of these models. Each of these will be discussed below.

B.1. Classical Nucleation Theory

The first void nucleation theories, proposed by Katz and Wiedersich [11] and by Russell [12] (WKR) are based on the classical theory of homogeneous precipitate nucleation, where a precipitate cluster grows by the addition of an atom and shrinks by emission. Unlike precipitate nucleation, void nucleation theory must account for an anti-vacancy, the interstitial. Thus, a vacancy cluster grows by vacancy absorption or interstitial emission and shrinks by emitting vacancies or absorbing interstitials. Modifications made to this WKR theory of vacancy condensation consider non-equilibrium interstitials produced during irradiation [13] and the presence of gas atoms [13-15] and of non-gaseous impurities [14]. Later modifications include gas pressure [16-18] and solute segregation effects [19-21].

The WKR model calculates the steady state cavity nucleation rate and the incubation time until steady state is attained. Russell [12-14,22,23] assumes the metal to be a continuum and expresses nucleation rate in terms of a critical cavity radius, r_c, and a free energy nucleation barrier, ΔG_c. The critical cavity radius is

defined as the radius at which the void has an equal probability of growing or shrinking. The critical size and the nucleation barrier are affected primarily by the point defect supersaturations, the internal energy of the vacancy cluster, and the mobile species diffusion coefficients. A key assumption of classical nucleation theory is that the concentrations of clusters up to the critical size are determined solely by reactions between the clusters and single defects only. That is, the direct interaction between clusters is neglected.

The steady state nucleation rate in Russell's model can be approximated as

$$J_s^o \simeq \frac{K}{\Omega} \exp\left(\frac{-16\pi\Omega^2\Gamma^3}{3(kT)^3\{\ell n S_v\}^2}\right) , \qquad (2.4)$$

where J_s^o is the homogeneous nucleation rate, K is the atomic displacement rate, Ω is the atomic volume, Γ is the free surface energy of a flat surface, and S_v is the vacancy supersaturation.

Wiedersich and Katz [11,15,24], on the other hand, use an atomistic approach to model void nucleation. They calculate defect fluxes into and out of void embryos. The assumptions in this theory also lead to a steady-state nucleation rate preceded by a short transient period. The steady state nucleation rate in this model cannot be represented by as brief an equation as (2.4) because of the detailed balancing of fluxes. Defining

$$m^{o}(x,x+1) \equiv \frac{s(x+1)n^{o}(x+1)}{s(x)n^{o}(x)} , \tag{2.5}$$

where $m^{o}(x,x+1)$ is the ratio of total surface area of clusters with x+1 vacancies to the total surface area of clusters with x vacancies,

$$P_x \equiv \left(1 + \frac{\beta_i - \beta_i^{o}}{\beta_v/m^{o}(x,x+1) + \beta_i^{o}}\right) , \tag{2.6}$$

where P_x is a correction factor which is the ratio of the flow of embryos toward smaller sizes when the interstitials are in equilibrium with the vacancies to the flow of embryos toward smaller sizes for the actual interstitial concentration,

$$\xi \equiv 4\pi\left(\frac{3\Omega}{4\pi}\right)^{2/3} \frac{\Gamma}{kT} \tag{2.7}$$

where ξ in the ratio of surface energy to thermal energy,

$$n(x) \equiv n^{o}(x) \prod_{j=1}^{x-1} P_j , \tag{2.8}$$

where n(x) is the void size distribution, and

$$n^{o}(x) = N_o \exp(x\ell n\, S_v - \xi x^{2/3}) , \tag{2.9}$$

where $n^{o}(x)$ is the void size distribution in equilibrium with the vacancy concentration, yields a steady-state nucleation rate given by

$$J_s^o = \left[\int_1^\infty dx([\beta_v + \beta_i^o m^o(x,x+1)]s(x)n(x))^{-1}\right]^{-1} \qquad (2.10)$$

where, β_i^o is the arrival and incorporation rate per unit area per unit time of interstitials to a void in a material with an interstitial concentration in equilibrium with the vacancy concentration, $\beta_{i,v}$ are the arrival and incorporation rates per unit area per unit time of interstitials and vacancies to a void, s(x) is the surface area of a void of size x, and N_o is the number of lattice sites in the material. J_s^o, Γ, Ω, and s_v are the same as in equation (2.4). Equation (2.10) neglects the presence of gas molecules.

B.2. Chemical Reaction-rate Theory

Mayer and co-workers [25] developed a model of void nucleation based on chemical kinetics. The original form of the model was first used to calculate dislocation loop nucleation [26]. A major assumption of their model is that the void distribution can be represented by the same number of voids having an average size. Thus, the void size distribution is not determined, but rather the change in the average size. Other assumptions include the fact that voids need at least one or two gas atoms to prevent their collapse into vacancy loops, vacancy clusters occur by collapse of the displacement spike vacancies as well as by diffusional vacancy condensation, and that alloying elements act as traps for point defects or for gas atoms.

Reaction-rate theory is predicated on the interaction of one defect species, n_1, with a second defect species, n_2, occurring with a velocity, v, and a capture cross-section, C. Thus, the rate of change of defect species n_3 is given by

$$\frac{dn_3}{dt} = - Cn_1n_2v \ . \qquad (2.11)$$

A series of such equations are written to account for all probable interactions. These series of equations are solved numerically. Because the problem is formulated this way, no single equation can be cited as the nucleation equation. In fact, the details of nucleation and of growth are inseparable in this model. Void nucleation rates can be obtained, however, by calculating the slope of the plot of the logarithm of number density versus the logarithm of dose.

B.3. Stochastic-Evolution Theory

The attempts to model void nucleation rates by classical nucleation theory and by chemical reaction-rate theory do not fully achieve their objectives. Classical nucleation theory requires assumptions that do not reflect reality in order to obtain nucleation rates that are close to observable values. Both classical approaches assume that point defect populations are in steady state throughout nucleation. Yet they require that void nucleation terminate when the point defect supersaturation drops because of the increased number of

voids. Furthermore, the surface energy of the material is assumed to be 1 J/m^2 when nucleation rates are calculated [11,13,27-28].

The void nucleation and growth models based on chemical kinetics does not require these assumptions in order to get quantitative agreement with experiment on void growth or number density. However, predictions of nucleation rates are lacking for two reasons. First, the model does not explicitly calculate nucleation rates. Secondly, somewhat arbitrary assumptions have to be made to define when a void is nucleated. A cavity is considered nucleated when at least five vacancies and one gas atom are clustered or when two gas atoms with no vacancies bind together.

These issues are redressed in a recent void nucleation theory proposed by Wehner and Wolfer [29]. One of the major assumptions of classical nucleation theory and of reaction-rate theory is that the subcritical cluster population does not influence the critical radius. Wehner and Wolfer remove this assumption and calculate the time-dependent evolution of the entire vacancy cluster population. Formulating the problem in this manner yields an expression for void distribution with a Fokker-Planck form. That is

$$\frac{\partial P(x,t)}{\partial t} = - \frac{\partial}{\partial x} [K(x)P(x,t)] + \frac{1}{2} \frac{\partial^2}{\partial x^2} [Q(x,t)P(x,t)] \qquad (2.9)$$

where $P(x,t)$ is the number density of clusters of size x at time t, $K(x)$ is a drift force, and $Q(x,t)$ is a diffusion function. Equation

(2.9) is solved by a path sum construction after a coordinate transformation from x to r, the cluster radius.

The path sum technique consists of integration over small time steps so that the transformed equation is assumed linear. The solution for P is used to calculate the point-defect concentrations and these new values are used to calculate new K and Q. With the new K and Q, P is recalculated over another small time step. Thus a feedback mechanism is established and the effect of the void size distribution on its own development is incorporated. Figure 2.2 details a typical progression of the void size distribution.

Void nucleation terminates for two reasons. First, as the void sink strength increases with time, the point defect concentrations drop. The second and more dominant reason for termination is that the rates of interstitial and vacancy absorption at voids begin to approach one another. This decreases the drift force, K which is analogous to increasing the nucleation barrier, ΔG_c, in classical nucleation theory. As the dose increases the critical radius also increases. Thus void nucleation is terminated. Figure 2.3 presents the calculated terminal void densities versus temperature in nickel for several dose rates.

C. GAS EFFECTS ON VOID NUCLEATION

It will be shown later that the presence of gas in an irradiated metal can alter the swelling response of the metal. This effect is observed whether the gas is present before the irradiation begins or

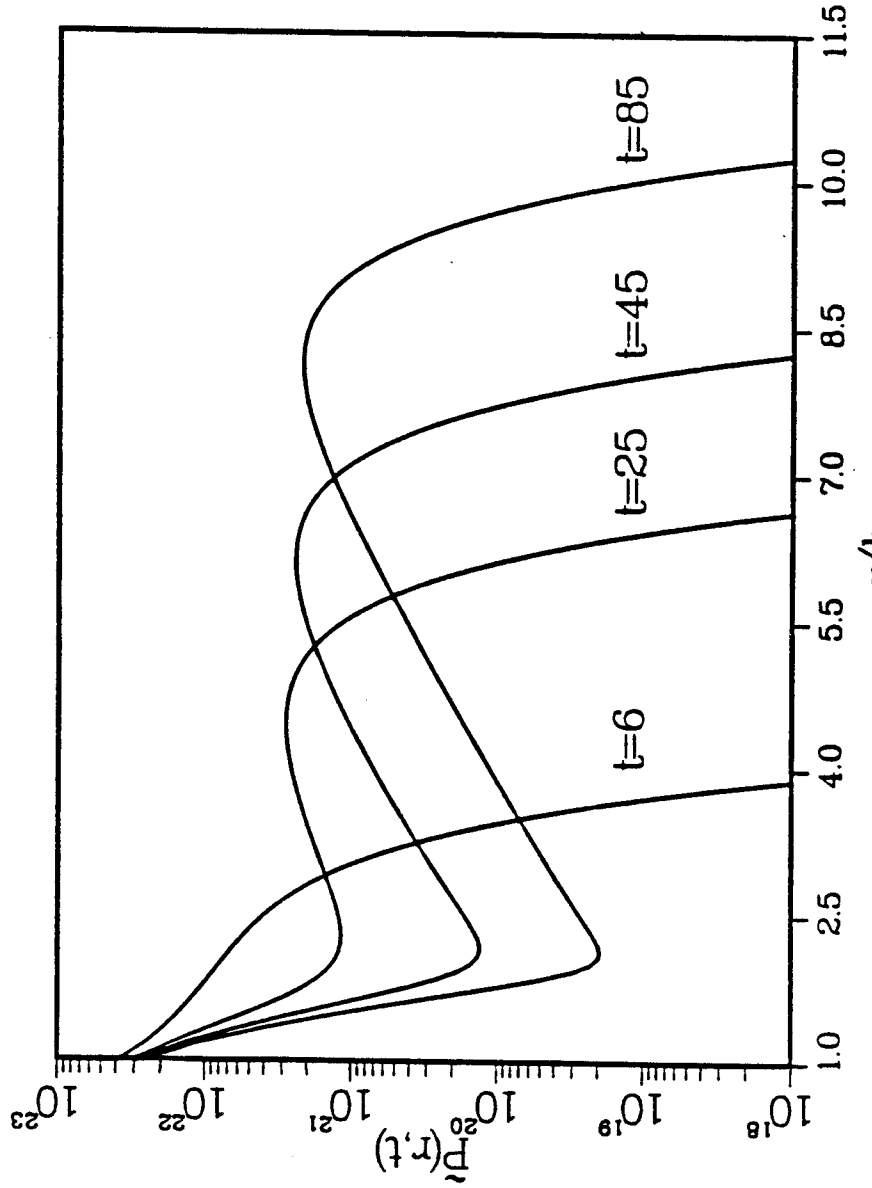

Figure 2.2. Calculated void size distribution versus void radii in nickel at various times for a dose rate of 0.001 dpa/s and a temperature of 600 °C in nickel. From ref. [29].

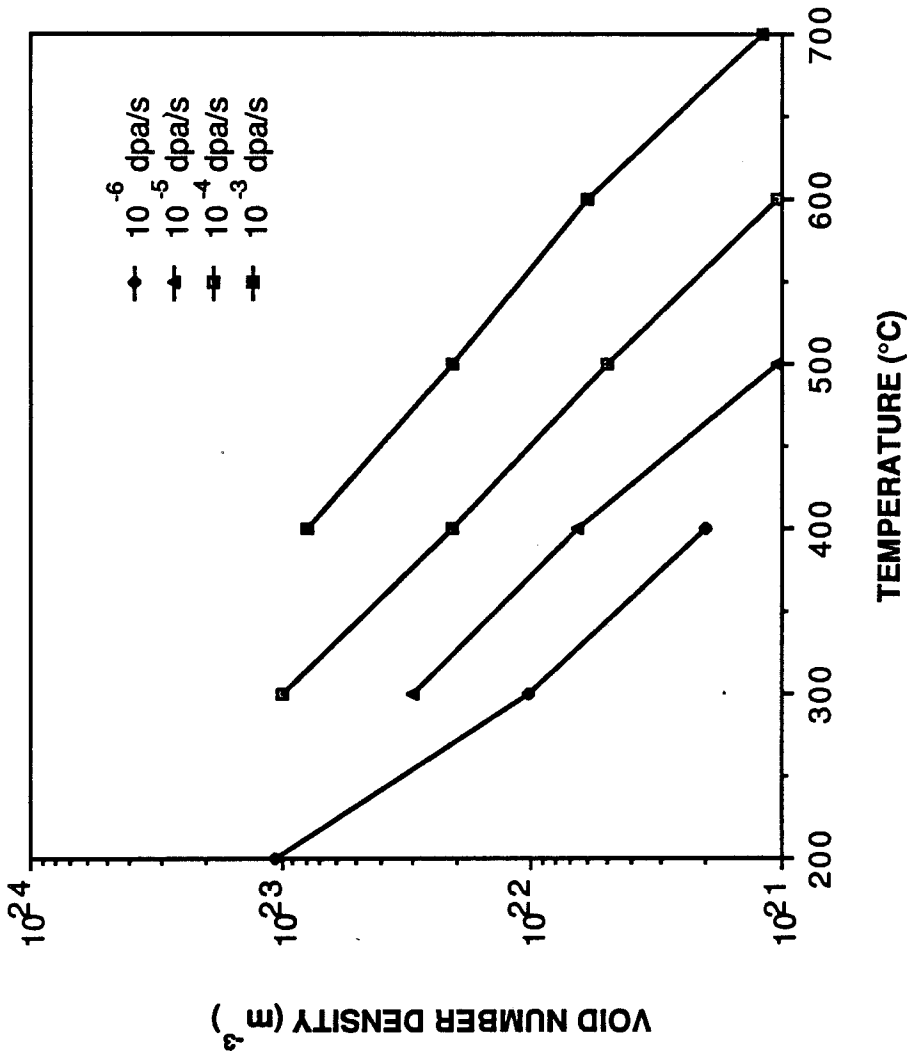

Figure 2.3. Terminal void number density as a function of temperature in nickel for various displacement rates from ref. [29].

is acquired during irradiation. A number of researchers believe that the presence of gas is essential for the formation of voids [15, 29-39]. The gas species can be either inert, like helium, or reactive, like oxygen or hydrogen. Because void formation is primarily a problem in materials used for nuclear applications, gas effects on the nucleation of voids are usually addressed in terms of helium. Helium is generated in metals exposed to fast neutron fluxes by the (n,α) reaction. However, in electron and ion irradiation simulations of neutron damage, helium is not present unless it is pre- or co-implanted. Therefore, in helium-free ion and electron irradiation residual gases must be responsible for void stability.

The incorporation of gas effects into the theory of void formation was first attempted by adaptations of the WKR theory [13-15, 23-24]. Katz and Wiedersich [15] calculated that dissolved gases do not affect void nucleation rates, except for possible changes in surface energy. The effect of insoluble gases is to increase the probability of a gas-containing cluster reaching critical size compared to that of a gas-free cluster. The probability increases with increasing number of gas atoms in the cluster. Russell [23] demonstrated the same effect for insoluble gas. For a reactive gas species, the change in nucleation rate depends on the mobility of the reactive gas. If it is mobile, the adsorption of the gas to the void surface reaches an equilibrium value, the surface energy drops, and the nucleation rate, equation (2.4), increases accordingly. If the gas is immobile, then nucleation must occur on the gas impurity and

the steady state nucleation rate becomes

$$J_s = J_s^o[1 - ZC_x^o \exp(\varepsilon_b/kT)] \qquad (2.13)$$

where J_s^o is given by equation (2.4), Z is a geometrical factor, C_x^o is the gas impurity concentration and ε_b is the binding energy of the impurity to a void surface.

The theory of Mayer and co-workers [25] treats all gas atoms equally. No distinction is made between soluble, insoluble, inert, or reactive gases. As noted earlier, a void is nucleated when at least one gas atom and five vacancies agglomerate. Any vacancy cluster with more than six vacancies and no gas atoms is assumed to collapse to a vacancy loop. Wehner and Wolfer [29] also assume that a void will collapse to a loop if not stabilized by a gas atom.

Recent theories on gas effects on void formation concentrate on helium [40-44]. These theories do not calculate void nucleation rates but rather consider the problem of the incubation time required for a gas bubble to grow to critical size. Unfortunately, the case of reactive, soluble gas in the absence of inert, insoluble gas is not described by these theories. This problem is usually dismissed, after noting that the surface energy will decrease by adsorption of the gas at the void surface. A theory is developed in the next chapter to address this problem.

D. Non-Gaseous Impurity Effect on Void Nucleation

Experimental evidence demonstrates that there can be a significant effect of major and minor alloying elements on vacancy cluster formation [45-53] and on void growth [51]. These alloying elements can affect void formation while in solution [54] as well as by forming second phases [55]. Void formation can increase or decrease depending on the type and amount of alloying element added. Several theories have been offered in an attempt to explain the effect of solute additions on swelling.

Lee and Mansur [53] attempt to explain the results of researchers who have noted that swelling decreases in the Fe-Ni-Cr ternary system as the nickel content increases [50,56-57]. They calculate that the critical cavity radius increases as nickel content increases, thereby suppressing void formation. Adda [45] claims that solute additions which decrease the stacking fault energy (SFE) lead to a decrease in void formation. A decrease in SFE means (as will be shown in chapter 3) that vacancy clusters of a faulted nature, the stacking fault tetrahedron and the faulted loop, become more energetically stable. Another explanation for the effect of impurity atoms on void nucleation is that impurities trap vacancies [49, 58-59]. This trapping of vacancies leads to increased recombination and a decrease in the vacancy supersaturation. However, Bullough and Hayns [58] calculate that this is true only at temperatures above the peak swelling temperature. Arguments have been put forth that elements which getter reactive gases are the major factor in the

suppression of swelling by impurities [51,60]. All of the above theories deal with impurity effects in solution, but the effect of precipitates on the swelling response is also important.

Mansur and co-workers [55] discuss the effects of precipitates on swelling in detail. This thesis is more concerned with the effect of solute impurities rather than second phases. However, it is worth noting that recent developments indicate that maximum swelling suppression is achieved by the formation of a high density of fine, thermally stable, and radiation stable precipitates that provide a large sink density for point defects and gas atoms [60-61]. Maintaining the high sink density allows the maximum incubation time before a critical number of gas atoms can accumulate to initiate swelling.

References for Chapter 2

1. M.T. Robinson, "The Theory of Radiation Induced Defect Production," in Fundamental Aspects of Radiation Damage in Metals, CONF-751006-P1, M.T. Robinson and F.W. Young, Jr., Eds. (1975) 1-20.
2. I.M. Torrens and M.T. Robinson, "Computer Simulation of Atomic Displacement Cascades in Metals," in Radiation Induced Voids in Metals, J.W. Corbett and L.C. Ianiello, Eds., CONF-710601 (1972) 739-756.
3. J.H. Kinney, M.W. Guinan, and Z.A. Munir, J. Nucl. Mat. 122 & 123 (1984) 1028-1032.

4. J. Lindhard, et al., Mat. Fys. Medd. Dan. Vid. Selsk. 33 (14) (1963).

5. I. Manning and G.P. Mueller, Computer Phys. Comm. 7 (1974) 85-94.

6. D.K. Brice, "Ion Implantation Range and Energy Deposition Codes COREL, RASE4, and DANG2," SAND77-0622 (1977).

7. S. Han and G.L. Kulcinski, "Computer Simulation of Ion Beam Mixing - Part I," in Fusion Reactor Materials, DOE/ER-0313/2 (1987) 105-109.

8. ASTM Standard E521, Annual Book of ASTM Standards, Part 45.

9. M.W. Thompson, Defects and Radiation Damage in Metals, Cambridge University Press (1969) 243-253.

10. L.K. Mansur, Nucl. Tech. 40 (1978) 5-34.

11. J.L. Katz and H. Wiedersich, J. Chem. Phys. 55 (1971) 1414-1425.

12. K.C. Russell, Acta. Met. 19 (1971) 753-758.

13. K.C. Russell, Acta. Met. 20 (1972) 899-907.

14. K.C. Russell, Scripta Met. 7 (1973) 755-760.

15. J.L. Katz and H. Wiedersich, J. Nucl. Mat. 46 (1973) 41-45.

16. W.G. Wolfer, "High-Density Equation of State for Helium and Its Application to Bubbles in Solids," in Effects of Radiation on Materials, ASTM STP 725, D. Kramer, H.R. Brager, and J.S. Perrin, Eds. (1980) 201-212.

17. C.A. Parker and K.C. Russell, Scripta Met. 15 (1981) 643-647.

18. W.G. Wolfer, B.B. Glasgow, M.F. Wehner, and H. Trinkhaus, J. Nucl. Mat. 122 & 123 (1984) 565-570.

19. A.D. Brailsford, J. Nucl. Mat. 56 (1975) 7-17.

20. R.C. Pillar and A.D. Marwick, J. Nucl. Mat. 83 (1979) 42-47.

21. A. Si-Ahmed and W.G. Wolfer, "Effect of Radiation-Induced Segregation on Void Nucleation," in Effects of Radiation on Materials: Eleventh Conference, ASTM STP 782, H.R. Brager and J.S. Perrin, Eds. (1982) 1008-1022.

22. K.C. Russell, Scripta Met. 6 (1972) 209-214.

23. K.C. Russell, Acta. Met. 26 (1978) 1615-1630.

24. H. Wiedersich, "A Generalized Theory of Nucleation," in Consultants Symposium on the Physics of Irradiation Produced Voids, R.S. Nelson, Ed., (1974) 147-157.

25. R.M. Mayer, L.M. Brown, and U. Gösele, J. Nucl. Mat. 95 (1980) 44-107.

26. L.M. Brown, A. Kelly and R.M. Mayer, Phil. Mag 19 (1969) 721-741.

27. R.W. Powell and K.C. Russell, Rad. Effects 12 (1972) 127-131.

28. C.A. Parker and K.C. Russell, J. Nucl. Mat. 119 (1983) 82-94.

29. M.F. Wehner and W.G. Wolfer, Phil. Mag. A 52 (1985) 189-205.

30. H. Wiedersich and J. L. Katz, "Effects of Insoluble Gases on Nucleation of Voids During Energetic Particle Irradiation," in Defects and Defect Clusters in B.C.C. Metals and Their Alloys, R.J. Arsenault, Ed., (1973) 530-544.

31. V. Levy, "Reactor Swelling of Pure Metals," in ref. 24 (1974) 50-70.

32. D.J. Mazey and S. Francis, "Observations of Dislocation Structure and Cavities Formed by Annealing in Type 316 Steel After Ion Irradiation at Ambient Temperature," in ref. 24 (1974) 257-262.

33. B.L. Eyre, "Irradiation Damage Structures Generated in Metals and Alloys During Irradiation at Elevated Temperatures," in ref. 1 (1975) 729-763.

34. L.M. Brown and R.M. Mayer, "The Nucleation of Point Defect Agglomerates," in ref. 24 (1975) 775-781.

35. J.M. Lanore, L. Glowinski, A. Risbet, P. Regnier, J.L. Flament, V. Levy, and Y. Adda, "Studies of Void Formation in Pure Metals," in ref. 1 (1975) 1169-1180.

36. K.H. Westmacott, Crystal Lattice Defects 6 (1976) 203-218.

37. M.I. Baskes, Trans. ANS 27 (1977) 320-321.

38. K. Farrell, Rad. Effects 53 (1980) 175-194.

39. B.N. Singh and A.J.E. Foreman, J. Nucl. Mat. (1981) 1469-1474.

40. M.R. Hayns, "The Transition from Gas Bubble to Void Growth," AERE-R-8806 (1977) 1-62.

41. L.K. Mansur, Nucl. Tech. 40 (1978) 5-34.

42. C.F. Clement and M.H. Wood, J. Nucl. Mat 89 (1980) 1-8.

43. L.K. Mansur and W.A. Coghlan, J. Nucl. Mat. 119 (1983) 1-25.

44. R.E. Stoller and G.R. Odette, J. Nucl. Mat. 141-143 (1986) 647-653.

45. Y. Adda, "Report on the CEA Program of Investigations of Radiation-Induced Cavities in Metals: Presentation of Some Results," in ref. 2 (1972) 31-83.

46. J.O. Stiegler, "Void Formation in Neutron-Irradiated Metals," in ref. 2 (1972) 292-337.

47. J.L. Brimhall, H.E. Kissinger, and G.L. Kulcinski, "The Effect of Temperature on Void Formation in Irradiated Pure and Impure Metals," in ref. 2 (1972) 338-362.

48. B.L. Eyre, J. Phys. F. 3 (1973) 422-470.

49. F.A. Smidt, J.A. Sprague, J.E. Westmoreland, and P.R. Malmberg, "The Effect of Alloy Additions on Void Nucleation and Growth," in ref. 30 (1973) 341-362.

50. W.G. Johnston, T. Lauritzen, J.H. Rosolowski, and A.M. Turkalo, "Void Swelling in the Iron-Chromium-Nickel System - A Survey by Nickel Ion Bombardment," in Properties of Reactor Structural Alloys After Neutron or Particle Irradiation, ASTM STP 570 (1975) 525-542.

51. V. Levy, N. Azam, L. LeNaour, G. Didout, and J. Delaplace, "Effect of Structure and Alloying Elements on Void Formation in Austenitic Steels and Nickel Alloys," in Radiation Effects in Breeder Reactor Strucutral Materials, M.L. Bleiberg and J.W. Bennett, Eds. (1977) 709-725.

52. M. Kiritani, K. Urban, and N. Yoshida, Rad. Effects 61 (1982) 117-126.

53. E.H. Lee and L.K. Mansur, Phil. Mag. A 52 (1985) 493-508.

54. J.A. Ellis, Jr., W.K. Appleby, and T. Lauritzen, "Swelling Simulation Studies of Type 316 Stainless Steel," in Irradiation Effects on the Microstructure and Properties of Metals, ASTM STP 611 (1976) 195-207.

55. L.K. Mansur, M.R. Hayns, and E.H. Lee, "Mechanisms Affecting Swelling in Alloys with Precipitates," in ref. 51 (1977) 359-382.

56. J.F. Bates and W.G. Johnston, "Effects of Alloy Composition on Void Swelling," in ref. 51 (1977) 626-644.

57. A Hishinuma, Y. Katano, and K. Shiraishi, J. Nucl. Sci. Tech. 15 (1978) 690-696.

58. R. Bullough and M.R. Hayns, Trans ANS 27 (1977) 335-336.

59. R.A. Johnson and N.Q. Lam, Phys. Rev. B 13 (1976) 4364-4375.

60. E.H. Lee and L.K. Mansur, J. Nucl. Mat. 141-143 (1986) 695-702.

61. M.P. Tanaka, P.J. Maziasz, A. Hishinuma, and S. Hamada, J. Nucl. Mat. 141-143 (1986) 943-947.

CHAPTER 3

A THEORY ON THE EFFECT OF OXYGEN ON VOID STABILITY

A. Void Stability in the Absence of Gas

Void nucleation theories generally ignore the problem of the thermodynamic stability of the void. However, the question of void nucleation is inseparable from the question of survivability of the void embryo. To determine the stability of the void with respect to other vacancy cluster types it is necessary to evaluate the energies of these cluster types. Calculations of these energies were first performed by Sigler and Kuhlmann-Wilsdorf [1] and by Cotterill [2] using an elastic continuum model. Kroupa [3] has derived similar expressions which are valid for small size clusters. It is assumed that vacancies can agglomerate into only four types of clusters. These are a perfect or prismatic loop, a faulted loop, a stacking fault tetrahedron, and a void. By calculating the energy per vacancy of each cluster type, it is possible to assess the relative stability of each. The cluster energies are calculated below for fcc metals.

The energy of a prismatic loop, according to Kroupa [3], is

$$E_p = \frac{GB^2}{2(1-\nu)} \{2R + (2R-\varepsilon)[(1-0.5\ K^2)F(K) - E(K)]\} \qquad (3.1)$$

where G is the shear modulus, b is the Burger's vector, ν is Poisson's ratio, R is the loop radius, ε is the core radius, and

$$K = \frac{4R(R-\varepsilon)}{(2R-\varepsilon)^2} , \tag{3.2}$$

and where F(K) and E(K) are elliptical integrals of the first and second kind, respectively. These integrals are given by

$$F(K) = \frac{2}{\pi} \int_0^{\pi/2} \frac{d\phi}{(1 - K^2 \sin^2\phi)^{1/2}} \tag{3.3}$$

and

$$E(K) = \frac{2}{\pi} \int_0^{\pi/2} d\phi (1 - K^2 \sin^2\phi)^{1/2} \tag{3.4}$$

Equations (3.3) and (3.4) may be approximated by the polynomial expansions given by Abramowitz and Stegun [4].

Kroupa [3] also gives the energy of a faulted loop as

$$E_F = \frac{b_F^2}{b^2} E_p + \pi R^2 \gamma \tag{3.5}$$

where b_F is the Burger's vector of the faulted loop and γ is the stacking fault energy. In order to convert equations (3.1) and (3.5) to an energy per vacancy, it is necessary to convert loop radius to number of vacancies. This conversion is given by

$$N = \frac{4\pi R^2}{\sqrt{3}\, a_o^2} \tag{3.6}$$

where N is the number of vacancies and a_o is the lattice parameter ($a_o = \sqrt{2}\ b$).

The energy of a stacking fault tetrahedron [5] is

$$E_T = \frac{Gb^2L}{6\pi(1-\nu)}\left[\ln\left(\frac{4L}{b}\right) + 1.017 + 0.97\ \nu\right] + \sqrt{3}\ L^2\gamma \qquad (3.7)$$

where L is the tetrahedron edge length. The conversion of edge length to number of vacancies is

$$N = L^2/a_o^2\ . \qquad (3.8)$$

Finally, the void energy is [6]

$$E_v = 4\pi R_v^2 \Gamma\left(1 - \frac{0.8}{N+2}\right) \qquad (3.9)$$

where R_v is the void radius and Γ is the planar free surface energy. The parenthetic expression in equation (3.9) is a surface energy correction factor for small voids. This correction is based on results of a model by Mruzik and Russell [7]. The number of vacancies in a void is calculated by

$$N = \frac{16\pi R_v^3}{3a_o^3} \qquad (3.10)$$

Utilizing these expressions, the energies of the different vacancy cluster types are compared in Fig. 3.1 using two different

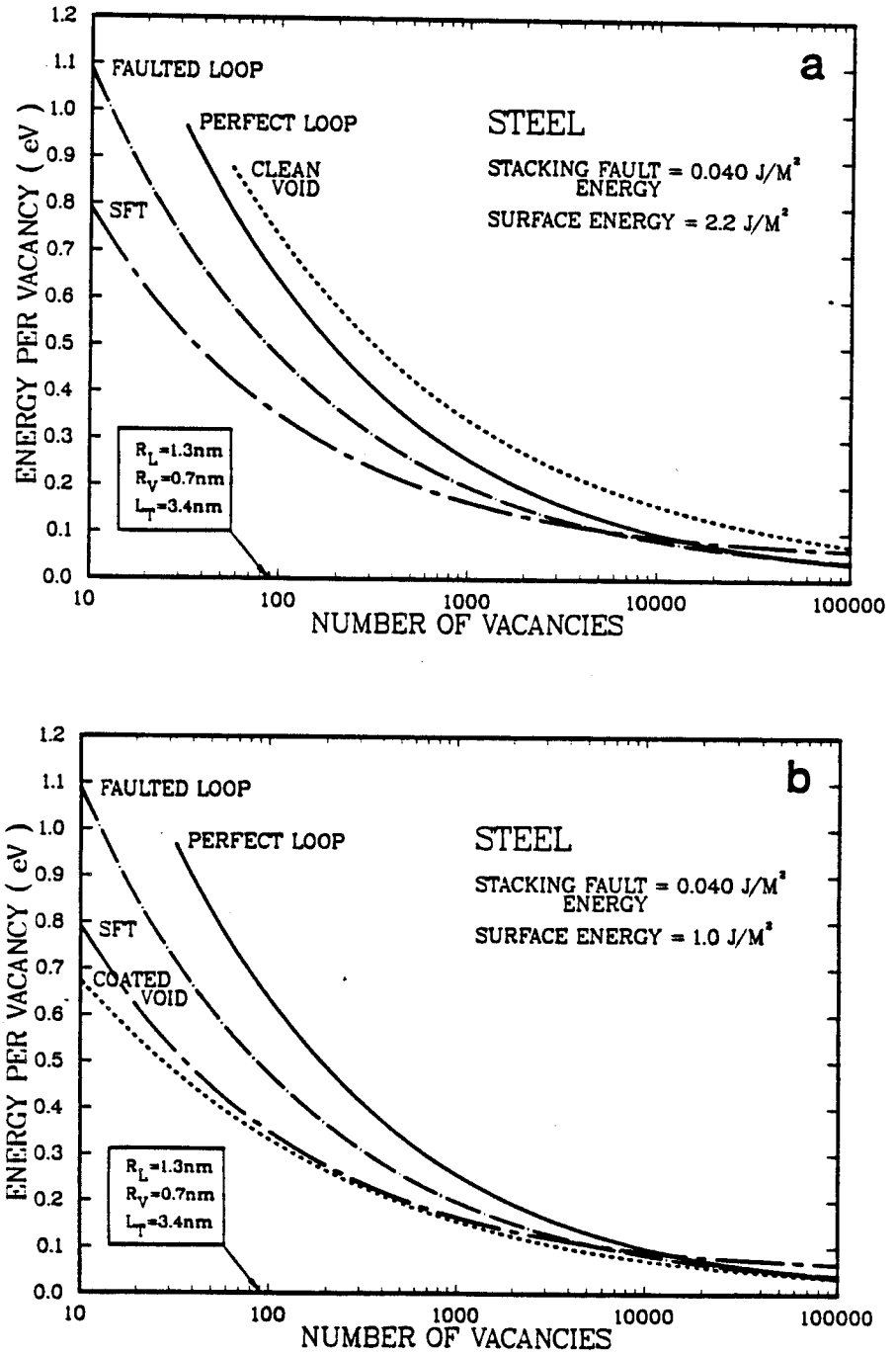

Figure 3.1. Comparison of the stability of different vacancy cluster species versus size in austenitic stainless steel with a surface energy of a) 2.2 J/m^2 and b) 1.0 J/m^2.

surface energies. A value for the surface energy typical of measured values is used in Fig. 3.1a and a value of 1.0 J/m^2 is used in Fig. 3.1b. The parameters used to evaluate the energy equations and all subsequent equations are given in Table 3.1. It is clear from Fig. 3.1 that the void is not a stable entity under normal conditions. In the absence of a reduction in surface energy, a subcritical void embryo should collapse to a stacking fault tetrahedron if the kinetics are not restrictive.

Table 3.1. Materials Parameters

Parameter	Value	Reference
Shear Modulus,[a] G (GPa)	57.6	8
Poisson's Ratio, ν	0.30	8
Lattice Parameter, a_o (nm)	0.363	9
Stacking Fault Energy, γ (J/m^2)	0.040	10
Surface Energy,[b] r (J/m^2)	2.2	11,12
Molar Surface Area, A (m^2/mol)	5.18×10^4	11
Heat of Chemisorption,[b] H_{cs} (kJ/mol)	540	13
Heat of Solution, H_u (kJ/mol)	335	14
Dissociation Energy, E_D (kJ/mol)	498.4	15

[a] $G = \frac{E}{2(1+\nu)}$

[b] value for γ-Fe

The transition from void to loop in fcc metals occurs by collapse of the surface layer of vacancies in a void to a single layer in the {111} plane. As the void collapse from a sphere to an oblate sphere to a planar arrangement of vacancies, the surface area and, therefore, surface energy increase. This increase in energy provides an activation barrier to collapse. This activation barrier is small ($\lesssim$ 50 kT) only for very small voids ($R_v \lesssim 1$ nm). Thus, once a void grows past this size it usually cannot collapse despite the fact that it is energetically unfavored with respect to other vacancy clusters. However, the void embryo can collapse before reaching a stable size. One can conclude that the morphology of visible vacancy clusters is dominated by the stability at small sizes.

The approximations of continuum theory begin to break down at small sizes and atomistic calculations should be used. However, qualitative agreement between this model and atomistic calculations is found for iron, molybdenum, and copper [16]. Doyama and co-workers [17], using position annihilation in a variety of FCC metals and alloys, demonstrate that clusters of vacancies are stabilized by gases. They estimate that collapse to a planar arrangement can occur in an unstabilized cluster containing as few as four vacancies. This data combined with the theory outlined in this chapter leads to the conclusion that, in the absence of a surface energy reduction, void formation in austenitic stainless steel free of inert gas is not possible. The manner by which surface energy reduction is achieved is discussed in the next sections.

B. Role of Oxygen

The adsorption of a reactive species on a metal surface causes a reduction in surface energy [18,19]. Oxygen is known to be a very potent surface active species [14] and a review of oxygen chemisorption has recently been performed [20]. Oxygen chemisorption on metals usually follows the pattern of molecular dissociation, adsorption, saturation, and oxidation. To calculate the magnitude of the surface energy change due to oxygen adsorption, the treatment of Bernard and Lupis [21] yields

$$\Gamma(\theta) = \Gamma - \frac{RT}{mA} \ln \left(\frac{1}{1 - m\theta}\right) , \qquad (3.11)$$

where $\Gamma(\theta)$ is the surface energy at fractional oxygen coverage, θ, A is the molar surface area, and m is an integer determined by the surface lattice at saturation, $M_{m-1}O$. For iron, a surface lattice of M_3O forms [14]. As chromium is added, the saturation coverage increases [22,23] to a monolayer, MO. Therefore, for 316 stainless steel a value of m = 2 is assumed. In Eq. (3.11) the interaction of oxygen atoms with each other has been neglected. Equation (3.11) can now be used to calculate the oxygen surface coverage, θ, required to reduce the surface energy to a value where the void is stable.

This surface coverage can be related to an atomic fraction of oxygen in solution, X, by the Langmuir-McLear isotherm [24]

$$X = \frac{\theta}{1-\theta} \exp - \left[\frac{G_B - G_S}{kT}\right] \qquad (3.12)$$

where G_B and G_S are the Gibbs free energies of oxygen in solution and oxygen chemisorption, respectively. Assuming that the entropies of these two energies are similar, one may approximate $G_B = -(H_u + E_D)/2$ and $G_S = -(H_{cs} + E_D)/2$, where H_u is the heat of solution of oxygen, E_D is the dissociation energy of the oxygen molecule and H_s is the heat of oxygen chemisorption. Evaluation of Eq. (3.12) assumes that H_s is independent of coverage. It is known that the degree of coverage reduces the heat of chemisorption [25]; however, some evidence indicates that for metals the reduction is small at moderate coverage [26]. Equation (3.12) allows the determination of the oxygen concentration that is required to achieve the partial coverage, θ, of a single surface.

In order to calculate the initial oxygen concentration, X_o, which will stabilize the voids and enhance swelling, it is necessary to evaluate the partitioning of the oxygen atoms during irradiation. An oxygen atom in solution at the beginning of the irradiation is permitted three possible fates during irradiation. The atom may remain in solution, it may chemisorb on a void embryo surface, or it may reassociate with another oxygen atom inside the embryo to form an oxygen molecule. The terminal void density and radius of Wehner and Wolfer [27] are used to calculate the total internal surface area per unit volume which exists, $A_v = n_v 4\pi R_v^2$. The density of chemisorbed oxygen atoms is then determined by that area that is chemisorbed divided by the surface area of an adsorbate atom, $\frac{A_v \theta}{(A/N_o)}$, where N_o is Avogadro's number. The density of oxygen atoms in solution is

simply the oxygen fraction, X, times the atomic number density. The density of oxygen atoms in molecular form is twice the product of the number of oxygen molecules per void and the void density, $(2N_o Xo_2)n_v$, where Xo_2 is the molar fraction of oxygen molecules. Sievert's law relates Xo_2 to the fraction of oxygen in solution, X. The total number of oxygen atoms remains unchanged, so

$$nX_o\Omega = nX\Omega + N_o \left(\frac{4\pi R_v^2}{A}\right)n_v\theta\Omega + 2\, N_o n_v Xo_2\Omega \qquad (3.13)$$

where Ω is the atomic volume. Calculations at all relevant temperatures indicate that the last term in Eq. (3.13) is many orders of magnitude smaller than the other terms. Therefore, a simpler expression may be used to calculate the initial oxygen concentration that determines void stability

$$X_o = X + \frac{N_o 4\pi R_v^2 n_v \theta}{nA} \quad . \qquad (3.14)$$

The variation in initial oxygen concentration needed for void stability as a function of temperature is plotted in Fig. 3.2. The temperatures investigated span the swelling range of 0.4-0.6 T_m. If the steel contains a concentration of oxygen in solution that is greater than that calculated, the entire void density should be stabilized. As the initial oxygen concentration decreases, fewer voids should obtain a sufficient coverage to prevent collapse. If no free oxygen is present, swelling should be completely suppressed if

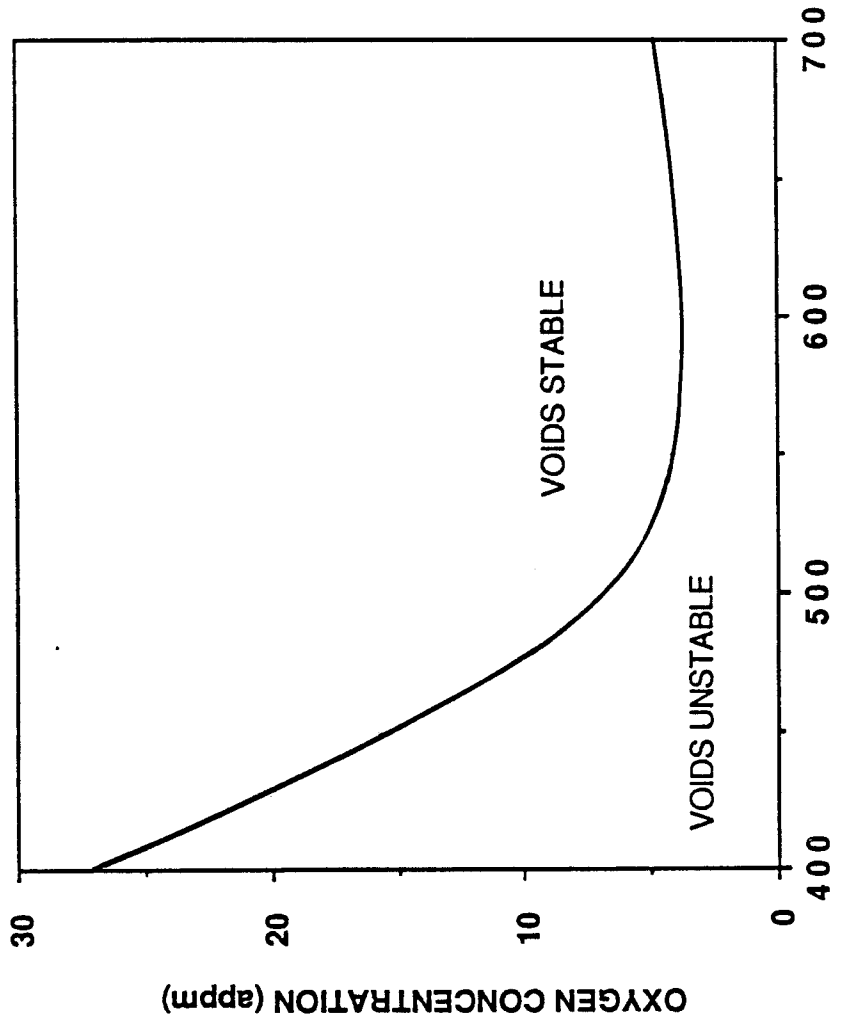

Fig. 3.2. Minimum oxygen concentration calculated to stabilize the entire void embryo population as a function of temperature in austenitic stainless steel.

no other gas or surface active species is present. The greatest value of the minimum oxygen concentration needed for void stability is approximately 29 appm and occurs at 400°C. This critical value of oxygen concentration is greater at lower temperatures because of the increased terminal void density [27]. The void densities and radii used in the calculation were for a dose rate of 10^{-3} dpa/sec. As the temperature increases, n_v decreases and the calculated value for X_o decreases to a minimum of about 4 appm at 550°C. At higher temperatures the increasing oxygen solubility causes X_o to increase.

The dose of 10^{-3} dpa/sec is typical for ion irradiation studies. Because there is no (n,α) transmutation reaction in ion bombardment, it is possible to study the effects of oxygen on swelling in the absence of helium. The predictions of Fig. 3.2 should be able to be tested by varying the oxygen content of an Fe-Ni-Cr ternary similar to 316 SS. However, there has been no known alloy developed which combines the elimination of significant concentrations of impurity elements (elements other than Fe, Ni, and Cr) and the reduction of oxygen to concentrations below 10 appm. Removal of additional elements is essential to properly test the proposed model.

One of the underlying assumptions of this model is that the oxygen in solution increases the quantity of oxygen which must be present in order to promote void stability. This fact, combined with void coalescence indicates that measured void densities should be lower than the predicted terminal densities. Such was the case reported for nickel [28]. Rectification of this problem can be

partly achieved by the inclusion of a sink term in Eq. (3.13) wherein oxygen is able to partition to internal defects such as grain boundaries and oxides bound by gettering elements. However, the complexity of the interaction of oxygen with the constituents of an austenitic stainless steel indicates that precise quantitative correlations of oxygen levels to void densities is not likely. Even if the physical processes could be exactly modeled, several parameters remain unknown for steel. Nevertheless, the prediction that a very low concentration of free oxygen is capable of enhancing swelling in 316 stainless steel should remain valid.

As noted earlier, the calculations of Eq. (3.13) indicate that there is very little driving force for oxygen to reassociate molecularly inside the void embryo. Rather, it is much more likely that an oxygen atom will chemisorb on the embryo surface. Thus, oxygen behaves differently from helium in the manner in which it stabilizes the void. Oxygen is not predicted to cause bubbles to form. Rather, it reduces surface energy by adsorption.

References to Chapter 3

1. J.A. Sigler and D. Kuhlmann-Wilsdorf, in The Nature of Small Defect Clusters, Vol. 1, M.J. Makin, Ed., (1966) 125.
2. R.M.J. Cotterill, in The Nature of Small Defect Clusters, Vol. 1, M.J. Makin, Ed., (1966) 144.
3. F. Kroupa, Czech. J. Phys. 10B (1960) 284.

4. M. Abramowitz and I.A. Stegun, Handbook of Mathematical Functions, Dover Press (1972) 591.

5. T. Jossang and J.P. Hirth, Phil. Mag. 13 (1966) 657-670.

6. A. Si-Ahmed and W.G. Wolfer, "Effect of Radiation-Induced Segregation on Void Nucleation," in Effects of Radiation on Materials: Eleventh Conference, ASTM STP 782, H.R. Brager and J.S. Perrin, Eds. (1982) 1008-1022.

7. M.R. Mruzik and K.C. Russell, Surf. Sci. 67 (1977) 205-225.

8. Smithell's Metal Reference Book, E.A. Brandes, Ed., Butterworth, p. 15-2.

9. B.D. Cullity, Elements of X-Ray Diffraction, Addision-Wesley, 1978, p. 508.

10. C.G. Rhodes and A.W. Thompson, Metallurgical Transactions A 8 (1977) 1901-1905.

11. W.R. Tyson, Canadian Metallurgical Quarterly 14 (1975) 307-314.

12. V.K. Khumikov and Kh.B. Khokonov, J. Applied Physics 54 (1983) 1346-1350.

13. K-I. Tanaka and K. Tamaru, J. Catalysis 2 (1963) 366-370.

14. V.W.A. Fischer, D. Janke, and W. Ackermann, Archiv für das Eisenhüttenwesen 41 (1970) 361-367.

15. R.C. Weast, CRC Handbook of Chemistry and Physics, 1979, p. F-230.

16. S.J. Zinkle, L.E. Seitzman, and W.G. Wolfer, Phil. Mag. A 55 (1987) 111-125.

17. M. Doyama, K. Hinode, and S. Tanigawa, J. Nucl. Mat. 85 & 86 (1979) 781-785.

18. E.D. Hondros, Acta Met. 16 (1968) 1377-1380.

19. M.D. Chadwick, Scripta Met. 3 (1969) 871-878.

20. K. Wandelt, Surface Science Reports 2 (1982) 1-121.

21. G. Bernard and C.H.P. Lupis, Surface Science 42 (1974) 61-85.

22. B. Ozturk, Ph.D. Thesis, Pennsylvania State University, 1981.

23. T. Smith and L.W. Crane, Oxidation of Metals 10 (1976) 135-148.

24. J.M. Blakely, in Chemistry and Physics of Solid Surfaces, Vol. II, R. Vanselow, Ed., CRC Press, Inc., Boca Raton, 1979, pp. 253-276.

25. S.R. Morrison, The Chemical Physics of Surfaces, Plenum Press, New York, 1977, pp. 229-234.

26. D. Brennan and M.J. Graham, Discussions of the Faraday Society, 41 (1966) 95-100.

27. M.F. Wehner and W.G. Wolfer, Phil. Mag. A 52 (1985) 189-205.

28. L.E. Seitzman, L.M. Wang, G.L. Kulcinski, and R.A. Dodd, J. Nucl. Mat. 141-143 (1986) 738-742.

CHAPTER 4

A REVIEW OF EXPERIMENTAL EVIDENCE OF THE EFFECT OF OXYGEN ON VOID STABILITY

Soon after Cawthorne and Fulton [1] discovered the existence of voids in irradiated stainless steel, simulation techniques for studying radiation damage were developed. Nelson and Mazey [2] simulated neutron damage in 316 SS with 100 kV proton, carbon, oxygen, and iron ion irradiations. Norris [13] was the first to utilize the high voltage electron microscope (HVEM) as an irradiation facility. Since then, many simulation experiments using particle (ion or electron) irradiation have included preimplanted or coimplanted helium for comparison with the results of neutron irradiated materials. Unfortunately, the inclusion of noble gases, especially helium, may have masked the effect of oxygen on void nucleation. This effect could be noticed despite the fact that the importance of oxygen was recognized early [4-8]. In order to evaluate the role oxygen plays in void formation, it is necessary to eliminate the effects of noble gases. Therefore, unless otherwise noted, all the data reviewed in this chapter is for material free of helium and other inert gases.

A. Oxygen Effect in Quenching Studies

Impurities in quenched metals can affect the nucleation of vacancy clusters in a variety of ways. Yoshida and Kiritani [9] point out that the stability of vacancy clusters can be directly and

indirectly affected by impurities. After an impurity is absorbed into the cluster it directly affects stability. Indirect influences occur when impurities in solution alter the effective mobility of vacancies, thereby changing the arrival rate of point defects to the clusters. Eyre [10] points out that impurities can lower stacking fault energies as well.

Previous to 1966, quenching studies in nickel and copper yielded relatively low densities of prismatic loops. Researchers [11-12] then quenched zone-refined material and found high densities of heterogeneously distributed faulted vacancy loops and stacking fault tetrahedra. These are the energetically favored secondary defects as calculated from elastic continuum theory [13]. Austenitic stainless steels also exhibit this dearth of observable secondary defects after quenching, except for high phosphorous (0.31 wt.%) bearing materials [14]. Westmacott [15] traced many of the inconsistencies in copper and silver to the presence of residual gases, particularly oxygen. Similar results on gold and platinum led Westmacott [16] to claim that very small residual interstitial impurity concentrations are crucial in determining the resultant secondary defects found in all quenched FCC metals. In this last study, it is found that voids never form in material that is remelted in an ultrahigh vacuum (UHV) and quenched under ultraclean UHV conditions. Westmacott also speculates that the anomalies in steel could be explained by the fact that phosphorous decreases oxygen solubility in steel as well as getters oxygen. Eyre and co-workers [17] suggest that the presence

of interstitial impurities causes nucleation on such a fine scale that defect clusters are too small to be seen in the microscope. Therefore, oxygen could play a dual role in quenching studies. It can act as a vacancy cluster nucleating agent as well as a void stabilizer [17].

The stability calculations for austenitic stainless steel presented in the previous chapter predict that the stacking fault tetrahedra (sft) and the faulted loop are the most stable vacancy-type defects. The first evidence of sft in quenched steel was presented in 1975 [18] and in deformed steel in 1977 [19]. These steels are prepared in a plasma induction furnace with high purity metals. Although Azarian et al. [18] found tetrahedra only in phosphorous bearing steel, Artigue and co-workers [19] report no difference between steels with and without phosphorous.

B. Oxygen Effect in Irradiation Studies

The first ion irradiation experiment performed to simulate fast neutron damage was an irradiation to ~ 0.5 dpa of solution treated (ST) type 316 stainless steel at 450 to 600°C with various bombarding particles [2]. Some samples were preinjected with helium. When irradiated with 100 keV C or Fe ions, the steel exhibited void formation in the absence of He. However, when the He concentration exceeded 10 appm, the void number density increases by an order of magnitude. However, when 100 keV oxygen were the bombarding species, little variation in void density or size was observed between the

helium-free and helium-injected material up to 1000 appm He. The importance of oxygen in void swelling was further highlighted when Urban [4] found that voids do not form in freshly prepared nickel bombarded with 650 keV electrons. Yet nickel samples that were stored in air and contained a 100 nm thick oxide layer show void formation after 40 minutes of irradiation. This result was attributed to oxygen atoms being knocked from the oxide into the matrix by the electron beam. A similar result is noted for electron-irradiated copper by Makin [5].

Adda [6] reported that preinjecting oxygen into ion-irradiated nickel increased swelling. Seitzman and co-workers [20] have also injected oxygen into nickel before ion bombardment. Their result reveals that the presence of freshly injected oxygen can increase void densities by one to two orders of magnitude. Wang et al. [21] found that heterogeneous void formation occurs in the immediate vicinity of nickel oxide inclusions in ion-irradiated nickel. They attribute this to the increase in free oxygen near the inclusion due to radiation-induced resolution of the oxide. Oxygen has also been preimplanted in copper before ion irradiation [22-23]. Again void number density increases significantly. It was also demonstrated [23] that the effect of oxygen is to reduce the void surface energy. Stainless steel has also been preinjected with oxygen by Nelson and co-workers [7]. They note that 316 SS swells under nickel ion irradiation with and without helium but that 18/8/Ti requires helium in order to form voids. After oxygen preinjection, however,

the void number density and size in the 18/8/Ti steel are similar to that of the helium preinjected material. They also found that nitrogen preinjected 18/8/Ti fails to produce voids when irradiated. They conclude that the Ti getters the residual oxygen, preventing it from stabilizing voids from collapse.

Other researchers have noted that variation in oxygen content in austenitic steel can affect void stability [24-25]. Sindelar et al. [24] found a large difference in the swelling response of nickel-irradiated 316 SS and P7 (a "high purity" 316 SS). No voids were found in the 316 but the P7 exhibited extensive swelling resulting from a bimodal void distribution. Previously, bimodal distributions had been found only in metals containing helium. The P7 alloy contains significant residual oxygen (1060 appm). Lee and Mansur [25] nickel bombarded an Fe-13 Cr-15 Ni alloy with P, Si, and Ti additions. The addition of either Si or Ti also eliminates void formation. The oxygen concentration in this alloy was reduced from 1050 appm to 700 appm when Si is added, to 455 appm when Ti is added, and to 140 appm when both are added. These two elements not only reduce the oxygen levels in the steel but also bind strongly to the remaining oxygen, thereby preventing it from diffusing to and stabilizing void embryos.

Further evidence for the efficacy of oxygen in promoting voids comes from outgassing and electropolishing studies [22, 26-28]. Void nucleation in ion-bombarded copper [22], nickel [26], and P7 [27] has been significantly reduced or eliminated when outgassed in high

vacuum. Buswell and co-workers [28] demonstrate that electropolishing before irradiation can significantly alter the void densities found in irradiated metals. Their work reveals that void response varies only with temperature, not polishing solution. In order to avoid introducing gas during electropolishing they find it necessary to polish at temperatures below -40°C. Hydrogen charging during polishing was thought to be the cause of their results. Sindelar et al. [29] have demonstrated that oxygen, not hydrogen, evolves at the anode during polishing and that oxygen, therefore, is the responsible agent for increased void densities. This last result indicates that care should be taken when comparing swelling results in materials that have been electropolished prior to irradiation. Unfortunately, all electron-irradiated and many ion-bombarded materials are electropolished before irradiation.

C. Review of Particle Irradiations on Austenitic Stainless Steels

Results of ion- and electron-irradiated austenitic stainless steels are often inconsistent. Even when the irradiating particle, the target material, the temperature, and the dose are identical, the resultant swelling can vary from one study to another. A survey of electron and ion irradiation studies of austenitic stainless alloys are presented in Table 4.1 and Table 4.2, respectively. Reiterating a point made earlier, all these irradiated alloys are free of noble gases either pre- or co-injected. In some cases the study did include some helium injections but that portion of the data is

Table 4.1. Void Nucleation in Austenitic Stainless Steels Bombarded by 1 MeV Electrons

MATERIAL	DOSE (dpa)	TEMP.(°C)	$N_v(10^{20}/m^3)$	$\bar{d}$ (nm)	COMMENTS	Ref.
EN 58B Fe-18 Cr-10 Ni-1 Mn-0.3 Ti	1.5	450	6.9	14		30
ST 316 SS	30					31
.02 wt%C		500	17.7			
		600	1.74	150		
		650	0.45			
.04%		500	37			
		600	4.5	100		
		650	1.0			
.16%		500	69			
		600	7.2	80		
		650	2.5			
.45%		500	72			
		600	9.8	70		
		650	3.5			
1.0%		500	24			
		600	10.0	70		
		650	6.1			
ST and 20% CW 316 SS	5-50	480-730	1-10 Around 600°C		ST swells more than 20% CW	32

Table 4.1. Void Nucleation in Austenitic Stainless Steels Bombarded by 1 MeV Electrons (Cont.)

MATERIAL	DOSE (dpa)	TEMP.(°C)	$N_v(10^{20}/m^3)$	$\bar{d}$ (nm)	COMMENTS	Ref.
ST 316 SS		550				28
	20		2.5			
	45		4			
	65		3.5			
	85		3			
	100		2			
20% CW 316 SS	8-50	400-600			Void nucleation ceases after a few dpa. Increased swelling as temperature increases.	33
ST 316 SS	2-40	470-670			Void density lower and diameter greater than He injected material.	34
ST 316 SS	to 0.4	100-500				
		below 500	0	-		
		500			Defect clusters visible which grow to voids after 0.1 to 0.2 dpa. Nucleation ceases after 0.2 dpa.	35

Table 4.1. Void Nucleation in Austenitic Stainless Steels Bombarded by 1 MeV Electrons (Cont.)

MATERIAL	DOSE (dpa)	TEMP.(°C)	$N_v(10^{20}/m^3)$	$\bar{d}$ (nm)	COMMENTS	Ref.
ST 316 SS		550	10	21		36
		620	1	45		
+ Ti	10-40	520			Decreased swelling.	
Fe-32 Ni-22 Cr	10-40	600				
+ Ti		600				
Fe-40 Ni-16 Cr	10-40	600	10	21	Ti reduces density and diameter. Nb reduces diameter only.	
+ Ti						
+ Nb						
Fe-22 Cr + XNi	10-40	600			Decreasing swelling with increasing nickel.	
X=35						
X=40			4	32		
X=50						
Fe-17 Cr-12 Ni	30	300-600				37
		370	10	< 50		
		600	1.0	~ 100		
Fe-17 Cr-50 Ni					No voids T>450°C. Incubation dose 10 dpa.	

Table 4.1. Void Nucleation in Austenitic Stainless Steels Bombarded by 1 MeV Electrons (Cont.)

MATERIAL	DOSE (dpa)	TEMP.(°C)	$N_v(10^{20}/m^3)$	$\bar{d}$ (nm)	COMMENTS	Ref.
Fe-15 Cr-25 Ni		600	11	29		38
ST 316	40	575				39
.01 wt%C						
.04			1-10			
.06			low C			
.45						
.73			10-40			
1.0			high C			
Fe-15 Cr-13 Ni-1Mn					130 appm O residual 20 appm N residual	40
0 wt% Si	~ 5	400	400			
		500	20			
		600	2			
		700	1			
2% Si	~ 25	450	100			
		550	2			
		650	0.2			

Table 4.1. Void Nucleation in Austenitic Stainless Steels Bombarded by 1 MeV Electrons (Cont.)

MATERIAL	DOSE (dpa)	TEMP.(°C)	$N_v(10^{20}/m^3)$	$\bar{d}$ (nm)	COMMENTS	Ref.
20% CW 316 SS	5	500	$100x10^{16}/m^2$	~ 30		41
		700	$100x10^{16}/m^2$	~ 50		
+ 2 wt% Si		300	$10x10^{16}/m^2$	~ 50		
0.1% Ti		500	$5x10^{16}/m^2$	~ 100		
		700	$2x10^{16}/m^2$	~ 150		
+1 wt.% Si		300	$8x10^{16}/m^2$	~ 35		
0.5% Ti		500	$9x10^{16}/m^2$	~ 50		
		700	$3x10^{16}/m^2$	~ 70		
316 SS	30	500-600			Peak swelling at 570°C	42
Fe-17 Cr-XNi						
X=12		370	15	20		
		450	11	20		
		500	8	20		
		530	5	40		
		550	2	60		
X=35		370	11	30		
		450	4	40		
		500	2	65		
		530	0.3	75		
		550	0.12	90		

Table 4.1. Void Nucleation in Austenitic Stainless Steels Bombarded by 1 MeV Electrons (Cont.)

MATERIAL	DOSE (dpa)	TEMP.(°C)	$N_v(10^{20}/m^3)$	$\bar{d}$ (nm)	COMMENTS	Ref.
X=50		370	9	20		42
		450	0.6	70		(cont.)
		500	0	-		
		530	0	-		
		550	0	-		
ST 310 SS	3	550	40		Dose is that of peak	43
	1	600	25		density in all alloys.	
	3	650	7			
ST RA 330 SS	4	450	67			
	15	500	56			
CW RA 330 SS	11	500	75			
ST Incoloy 800	7	500	24			
	9	600	18			
	9	650	4			
STA A286	30	500	0		STA = solution treated	
		600	0.006		and aged	
ST Nimonic PE16	1	550	150			
	8	650	11			

Table 4.1. Void Nucleation in Austenitic Stainless Steels Bombarded by 1 MeV Electrons (Cont.)

MATERIAL	DOSE (dpa)	TEMP.(°C)	$N_v(10^{20}/m^3)$	$\bar{d}$ (nm)	COMMENTS	Ref.
STA Nimonic PE16	0	550	8.5			43
	5	650	5.5			(cont.)
OA Nimonic PE16	8	500	4.7		OA=over aged (beyond recrystallization)	
	9	600	1.4			
	9	700	0.67			
STA M813	6	450	16			
	7.5	500	42			
	1	550	36			
	7	600	6.8			
	0	650	3.0			
ST Inconel 706	30	550	0			
	30	600	0			
STA Inconel 706	3	550	3			
	0	600	0.71			
STA Incoloy 901	5	500	1.2			
	1	550	1.4			
	5	600	0.1			
ST Inconel 625	3	500	5			
	9	600	2			

Table 4.1. Void Nucleation in Austenitic Stainless Steels Bombarded by 1 MeV Electrons (Cont.)

MATERIAL	DOSE (dpa)	TEMP.(°C)	$N_v(10^{20}/m^3)$	$\bar{d}$ (nm)	COMMENTS	Ref.
STA Inconel 718	30	500	low		Too hard to measure	43
	30	600	0			(cont.)
304 SS	20					44
+ 0.02 wt% N		400	10	30		
		500	10	50		
		600	1.0	120		
+.08%		400	20	20		
		500	17	30		
		600	0.8/40	120/80	Secondary nucleation after 16 dpa.	
+0.13%		400	50	12		
		500	19	25		
		600	0.4/40	120/80	Secondary nucleation after 10 dpa.	
Fe-15 Cr-15 Ni-2.5 Mo-0.8 Nb		650			60 appm O residual. Dose is that of peak density.	45
ST	2		7			
10% CW	6		18			
30% CW	15		20			

Table 4.1. Void Nucleation in Austenitic Stainless Steels Bombarded by 1 MeV Electrons (Cont.)

MATERIAL	DOSE (dpa)	TEMP.(°C)	$N_v(10^{20}/m^3)$	$\bar{d}$ (nm)	COMMENTS	Ref.
Fe-13 Ni-30 Cr + Si	to 30	500			Si reduces swelling. +3.75% Si no voids to 40 dpa.	
Fe-25 Ni-30 Cr + Mn					Mn reduces swelling by increasing incubation period only.	46
ST 316 SS	5-7	600				47
0.05 atom % N+C			20			
0.3%			5			
0.5%			4			
0.6%			9			
20% CW 316 SS						
0.05 atom % N+C			20			
0.3%			30			
0.5%			50			
0.6%			55			

Table 4.1. Void Nucleation in Austenitic Stainless Steels Bombarded by 1 MeV Electrons (Cont.)

MATERIAL	DOSE (dpa)	TEMP.(°C)	$N_v(10^{20}/m^3)$	$\bar{d}$ (nm)	COMMENTS	Ref.
316 SS + .25 Ti	10	350-600				48
0 wt.% Nb		350	70	14		
		400	50	16		
		450	6	35		
		500	1.4	44		
		550	1.8	79		
		600	0.15	103		
0.12%		350	11	10		
		400	1.2	20		
		450	11	21		
		500	0.4	10		
		550	0.3	17		
		600	0.1	48		
0.21%		350		1		
		400	60	3		
		450	20	6		
		500	4	10		
		550	0.4	10		
		600	0.3	42		

Table 4.1. Void Nucleation in Austenitic Stainless Steels Bombarded by 1 MeV Electrons (Cont.)

MATERIAL	DOSE (dpa)	TEMP.(°C)	$N_v(10^{20}/m^3)$	$\bar{d}$ (nm)	COMMENTS	Ref.
316 SS	20-50	550				49
+ 0 Ti, 0 Zr	20		.4	100		
	35		.4	150		
	50		.4	190		
+0.3 wt.% Zr	20		.02	50		
	35		.08	80		
	50		.07	130		
+0.25 wt.% Ti	20		.02	60		
	35		.02	90		
	50		.05	125		
+0.12% Ti .08% Zr	to 50		0	-		
JPCA	5	450	3			50
	10		4			
	18		9			
316 SS + 0.08 Wt.% Ti		500				51
Base Metal	15		0.5	68		
Heat Affected Zone	15		5	54		
Weld Metal	6		10	25		
JPCA	15		0	-		

Table 4.1. Void Nucleation in Austenitic Stainless Steels Bombarded by 1 MeV Electrons (Cont.)

MATERIAL	DOSE (dpa)	TEMP.(°C)	$N_v(10^{20}/m^3)$	$\bar{d}$ (nm)	COMMENTS	Ref.
FE-15 Ni-XCr X=10,16,20	30	450,550, 650			Voids at all temperatures.	52
X=10		650	10		Incubation dose 15 dpa.	
X=20		650	20		Incubation dose 5 dpa. Maximum void density reported.	
Fe-13 Cr-14 Ni	$1x10^{26}$ e^-/m^3 (180 sec dose)	200	250		Stacking fault tetrahedra convert to voids	53
		250	300			
		300	500			
		350	250			
ST 304 SS		400	50			54
		450	30			
		500	10			
		550	1.1			
		600	3.5			

Table 4.1. Void Nucleation in Austenitic Stainless Steels Bombarded by 1 MeV Electrons (Cont.)

MATERIAL	DOSE (dpa)	TEMP.(°C)	$N_v(10^{20}/m^3)$	$\bar{d}$ (nm)	COMMENTS	Ref.
Fe-16 Cr-17 Ni	2					55
0%P		300		~ 2	Also vacancy loops	
		350	110	8	and SFT 100-400°C.	
		400	5	23		
		450	3	34		
+0.1 wt.% P		450	190	5	Also vacancy loops	
		500	30	11	and SFT 250-500°C.	
		550	10	23		
		600		40		
CW 316 SS	50	500	1	9	80 appm residual O	77
		600	0.4	19		
+ Ti		500	2.5	12		
		600	0	-		
+ Zr		500	0.6	7.4		
		600	0.08	13		
+ V		600	30	4.5	160 appm residual O	
+ TiZr		500	0	-	80 appm residual O	
		600	0	-		
+ TiV		500	50	0.9		
		600	0	-		
+ ZrV		500	15	1.6		
		600	10	5.5		

Table 4.2. Ion Irradiation Studies of Void Nucleation in Austenitic Steels

MATERIAL	ION	DOSE (dpa)	TEMP. (°C)	$N_V(10^{20}/m^3)$	$\bar{d}$(nm)	COMMENTS	REF.
ST 316 SS	100 kV C,Fe,O,P	10^{17}-10^{19} ion/cm^2	450 to 600			Oxygen irradiation-cavitation density and size independent of presence of He.	2
ST 316 SS	20 MeV C	40	550			Voids form after interstitial faulted loops form.	56
4% CW 316 SS	5 MeV Cu	$2x10^{16}$ ion/cm^2	500	60	18		57
CW 348 SS	5 MeV Ni	$3x10^{16}$ ion/cm^2	625	0.5	8-25	Nb stabilized steel	58
316 SS	20 MeV C		525			Voids with and without He, lower density without.	7

Table 4.2. Ion Irradiation Studies of Void Nucleation in Austenitic Steels (Cont.)

MATERIAL	ION	DOSE (dpa)	TEMP. (°C)	$N_V(10^{20}/m^3)$	$\bar{d}$(nm)	COMMENTS	REF.
18/8/Ti						Hard to find voids without He. Preinject O, void number density and diameter similar to He injected. Preinject N, no effect.	7
304 SS	4 MeV Ni	5	500	~ 3	~25		59
304 SS	5 MeV Ni	20	625	0.8	32		60
		70		1.2	47		
		140		3	60		
316 SS		50		0.19	36		
		100		0.30	45		
		200		0.45	68		
ST 316 SS	46.5 MeV Ni	1	RT	0	-	RT=room temperature irradiation. OHA=one hour anneal.	61
			OHA	3	7		
			650				
		10	RT	0	-	loops only	
			OHA	0	-		
			650				

Table 4.2. Ion Irradiation Studies of Void Nucleation in Austenitic Steels (Cont.)

MATERIAL	ION	DOSE (dpa)	TEMP. (°C)	$N_V(10^{20}/m^3)$	$\bar{d}$(nm)	COMMENTS	REF.
316 SS	5 MeV Ni	120	525 580 650	30 0.6 0.1	16 100 170	No voids visible below 20 dpa.	62
ST 316 SS	500 keV Ni	30	600			Voids present	36
+ Mo			600				
+ Cu						$\Delta V/V(\%)$	
+ .021%C			600			.271	
			650			1.21	
+ .027%C			600			.264	
			650			.31	
+ .034%C			600			.254	
			650			-	
+ .054%C			600			.05	
			650			.025	
						Carbon effective only in solution.	
						C reduces density only.	

Table 4.2. Ion Irradiation Studies of Void Nucleation in Austenitic Steels (Cont.)

MATERIAL	ION	DOSE (dpa)	TEMP. (°C)	$N_V(10^{20}/m^3)$	$\bar{d}$(nm)	COMMENTS	REF.
Fe-16 Cr-14 Ni-20 Mo-2 Mn (0.5 Si)	4 MeV Ni	to 30	625			Voids below 30 dpa.	63
(1 Si, 0.1 Ti, .04 Nb, .06 Zr)		to 600		0	-	No voids to 600 dpa.	
304 SS	28 MeV Si	20	25-750	<0.0001			64
P7	4 MeV Ni	1	625	20	11	1060 appm O residual	65
		10		9	38		
		70		4	89		
P7	4 MeV Ni	1	575	8	10	1060 appm O	66
		70		10	50		
		1	675	0.05	25		
		70		0.5	180		
		1	750	0	-		
		70		0.03	250		
		1	825	0	-		
		70		0.0001	100		

Table 4.2. Ion Irradiation Studies of Void Nucleation in Austenitic Steels (Cont.)

MATERIAL	ION	DOSE (dpa)	TEMP. (°C)	$N_V(10^{20}/m^3)$	$\bar{d}$(nm)	COMMENTS	REF.
316 SS	1.1 MeV N	14	450 500 530 600 650	7.5 8 4 3 2	10 15 20 27 23	Cross-section technique applied; data taken from 0.7 μm depth at swelling peak.	67
P7	4 MeV Ni	10	675	2.5	55		68
Fe-17 Cr-17 Ni-2.5 Mo	4 MeV Ni	10	570 625 675 750 825	6.6 9 0.18 0.016 0	31 38 99 118 -		69
P7	4 MeV Ni	10	750	0.18	84	1060 appm O residual.	70
Fe-15 Cr-15 Ni-2 Mo-2 Mn-1 Si-0.2 Ti	4 MeV Ni	125	675	0	-	No voids without He	71

Table 4.2. Ion Irradiation Studies of Void Nucleation in Austenitic Steels (Cont.)

MATERIAL	ION	DOSE (dpa)	TEMP. (°C)	$N_V(10^{20}/m^3)$	$\bar{d}$(nm)	COMMENTS	REF.
316 SS ST,STA, 20% CW	3 MeV Ni	5	630 to 650	0	-	No voids without He	72
316 SS	140 keV p		625			Step-height measurement only. Swelling saturates at 260% at 600 dpa.	73
Fe-15 Cr-15 Ni-2.5 Mo-0.8 Nb	1 MeV Cr		650			60 appm O residual Dose is that of peak density.	45
ST		30		20			
10% CW		85		7			
30% CW		140		5			
ST 316 SS						Cross-Section Technique	74
	1 MeV C	10	530	1.5	12	Void denuded zone 0.5-0.8 μm	
			650	10	4		
		42	530	6	80	Void denuded zone 0.9-1.3 μm	
	1.1 MeV N	42	530	6	55	Void denuded zone 0.7-1.1 μm Peak void density at 0.5 μm.	

Table 4.2. Ion Irradiation Studies of Void Nucleation in Austenitic Steels (Cont.)

MATERIAL	ION	DOSE (dpa)	TEMP. (°C)	$N_V(10^{20}/m^3)$	$\bar{d}$(nm)	COMMENTS	REF.
316 SS	3 MeV Ni	to 25	625				75
ST,STA		5			0.5 to 1.0		
20% CW		5		0	-		
ST 316 SS	14 MeV Ni	12	575	0	-	Cross-Section Technique	24
P7		10	650	4.8	40	1060 appm O residual	
		50		1.6	40	Bimodal distribution	
		50		1.6	200	at 50 dpa.	
316 SS	14 MeV Ni	10	450	4	7.5	150 appm O residual.	76
		40		5	12	Cross-section technique applied.	
		10	500	1.3	21	10 and 30 dpa levels	
		40		2.3	24	at 1 μm depth.	
		30		0.91	25	40 and 120 dpa levels	
		120		1.4	30	at peak damage depth.	
		10	550	1.5	20		
		40		2.1	25		

Table 4.2. Ion Irradiation Studies of Void Nucleation in Austenitic Steels (Cont.)

MATERIAL	ION	DOSE (dpa)	TEMP. (°C)	$N_V(10^{20}/m^3)$	$\bar{d}$(nm)	COMMENTS	REF.
Fe-13 Cr-15 Ni	4 MeV Ni	95	675	2.2	63	1050 appm O residual	25
+.05 wt% P		86		2.0	65	1050 appm O	
+.84 Si, .05 P		85		0	-	700 appm O	
+.18 Ti, .04C, .05 P		97		0	-	455 appm O	
+.83 Si, .17 Ti, .04 C, .05 P		59		0	-	140 appm O	
Fe-15 Ni-XCr X=10,16,20	46.5 MeV Ni	to 30	450, 650			No voids at 450°C to 30 dpa. Copious voids at 650°C 30 dpa Maximum void density in 20 Cr alloy. ~ 3 time that in 10 Cr alloy.	52

excluded. Inspection of Tables 4.1 and 4.2 reveals that several variables affect the swelling data. These are major and minor alloying elements, thermomechanical pretreatment, and temperature. All these are discussed below.

The effects of the major alloying elements Ni and Cr on void formation in ion-bombarded Fe-Ni-Cr alloys were first studied by Johnston et al. [78] although they preimplanted He to 15 appm. Other researchers [36-37, 42-43, 52] have performed similar experiments without helium. In all cases increasing the nickel content and reducing the chromium content decrease the void density. Garner et al. [79-80] have attributed this to a delay in spinodal-like decomposition of Fe-Ni-Cr alloys at moderate nickel contents.

Minor solute element effects have also been extensively studied [25,31,36,39-41,44,46-49,55,63]. Carbon has been shown to both increase and decrease void density in electron and ion irradiations [31,36,39] of 316 SS. This is true even when the irradiations are carried out at the same temperature. Nitrogen can increase the void density by itself [44] but in conjunction with carbon it can increase or decrease the void density depending on the thermomechanical treatment [47]. Silicon additions to austenitic steel invariably reduces void formation and prolongs the incubation period [25,40-41,46]. Manganese additions have been found to also extend the incubation dose [46]. The role of phosphorus is not as clear. In one ion irradiation study [25] phosphorus failed to affect the swelling behavior, while in an electron-bombarded alloy [55] the void

number density increased with the addition of phosphorus. Niobium reduces swelling in irradiated steels, although one study claims only the void size is affected [36] whereas another finds a reduction of density [48] for moderate amounts of niobium. This latter study finds that increasing the niobium content from 0.12 wt% to 0.21 wt% increases the void number density. Vanadium appears to enhance void formation [77], while zirconium [49,77] and titanium [25,36,41,49,77] are effective at suppressing voids. Vanadium additions appear to lessen the efficiency of zirconium and titanium in limiting void formation [77], while the combination of titanium and zirconium together seems to be most effective in swelling suppression [49,77].

Another variable in irradiation studies is the pre-irradiation thermomechanical treatment. The treatments considered below are solution treated (ST), solution treated and aged (STA), overaged (OA), and cold-worked (CW). When comparing solution treated versus cold-worked pretreatment inconsistencies appear. In some cases cold-work increased the void density [43,45,47], while in others the density was reduced [45] and in others there was no effect [47,72]. In one study cold-working 316 SS eliminated swelling but it is not clear whether the number density was reduced to zero or whether the density has increased but the size is reduced beyond visibility in the microscope [75]. The effect of aging is also equally ambiguous. In one study [43] one alloy shows a drop in number density of voids when aged and a further drop when overaged while another alloy which contained no voids in the solution treated condition contained voids

in the aged condition. In other studies aging had no effect on void density [72,75].

The effect of temperature on void response of irradiated austenitic stainless alloys is not conclusive either. As the temperature increases the void density can initially increase then decease [31,43,66-67], initially decrease then increase [54,76], increase only [74], decrease only [40-44,48,55,62,69], or remain steady [53]. These result cannot, with one exception, be attributed to irradiating particle, temperature range surveyed, or material bombarded. In the case where the void density remained constant, the temperature range was 200 to 350°C where mobilities are low and kinetics are sluggish. Although it is not listed in Tables 4.1 and 4.2, dose rate differences do not explain these variations in swelling either.

The lack of consistency in void density trends for temperature, thermomechanical history, and alloying element from one study to another is clear. Often these inconsistencies have been eliminated when helium is injected before bombardment. This indicates that gas content is a critical variable in ion irradiation studies. Few researchers list the oxygen content of their alloy, yet it appears that variations in oxygen levels can have a dramatic effect in the swelling response of a single ion- or electron-irradiated metal. The remainder of this study is concerned with determining how oxygen impacts void nucleation in austenitic stainless steel.

References for Chapter 4

1. C. Cawthorne and E.J. Fulton, Nature 216 (1967) 575-576.
2. R.S. Nelson and D.J. Mazey, "Void Formation in Stainless Steel During Charged-Particle Irradiation at Elevated Temperatures," in Radiation Damage in Reactor Materials, Vol. II, IAEA (1969) 157-163.
3. D.I.R. Norris, Nature 227 (1970) 830-831.
4. K. Urban, Phys. Stat. Solidi (a) 3 (1970) K167-K168.
5. M.J. Makin, "The Production of Voids in Copper by Electron Irradiation in a 1 MV Electron Microscope," in Voids Formed by Irradiation of Reactor Materials, S.F. Pugh, M.H. Loretto, and D.I.R. Norris, Eds. (1971) 269-274.
6. Y. Adda, "Report on the CEA Program of Investigations of Radiation-Induced Cavities in Metals: Presentation of Some Results," in Radiation-Induced Voids in Metals, J.W. Corbett and L.C. Ianniello, Eds. (1972) 31-83.
7. R.S. Nelson, J.A. Hudson, D.J. Mazey, G.P. Walters, and T.M. Williams, "Void Formation in Metals During Ion Bombardment," in ref. 6 (1972) 430-448.
8. J.T. Buswell, S.B. Fisher, J.E. Harbottle, D.I.R. Norris, and K.R. Williams, "The Application of High-Voltage Electron Microscopy to Void Studies," in ref. 6 (1972) 533-549.

9. S. Yoshida and M. Kiritani, "The Role of Small Vacancy Clusters in Quenched Face-Centered Cubic Metals," in Lattice Defects and Their Interactions, R.R. Hasiguti, Ed. Gordon and Breach, NY (1967) 456-476.

10. B.L. Eyre, J. Phys. F. 3 (1973) 422-470.

11. L.M. Clarebrough, R.L. Segall, and M.H. Loretto, Phil. Mag. 13 (1966) 1285-1291.

12. P. Humble, M.H. Loretto, and L.M. Clarebrough, Phil. Mag. 15 (1967) 297-303.

13. S.J. Zinkle, L.E. Seitzman, and W.G. Wolfer, Phil. Mag. 55 (1987) 111-125.

14. A.F. Rowcliffe and R.B. Nicholson, Acta Met. 20 (1972) 143-155.

15. K.H. Westmacott, Phil. Mag. 24 (1971) 475-480.

16. K.H. Westmacott, Crystal Lattice Defects 6 (1976) 203-218.

17. B.L. Eyre, M.H. Loretto, and R.E. Smallman, "Electron Microscopy Studies of Point Defect Clusters in Metals," in Vacancies '76, R.E. Smallman and J.E. Harris, Eds. (1976) 63-78.

18. A. Azarian, M. Da Cunha Belo, and J. Leteurtre, Scripta Met. 9 (1975) 185-192.

19. F. Artigue, M. Condat, and M. Fayard, Scripta Met. 11 (1977) 623-626.

20. L.E. Seitzman, L.M. Wang, G.L. Kulcinski, and R.A. Dodd, J. Nucl. Mat. 141-143 (1986) 738-742.

21. L.M. Wang, R.A. Dodd, and G.L. Kulcinski, J. Nucl. Mat. 141-143 (1986) 713-717.

22. J.M. Lanore, L. Glowinski, A. Risbet, P. Regnier, J.L. Flament, V. Levy, and Y. Adda, "Studies of Void Formation in Pure Metals," in Fundamental Aspects of Radiation Damage in Metals, Vol. II, CONF-751006-P2 (1975) 1169-1180.

23. M.F. Felsen and P. Regnier, Scripta Met 11 (1977) 133-136.

24. R.L. Sindelar, G.L. Kulcinski, and R.A. Dodd, J. Nucl. Mat. 122 & 123 (1984) 246-251.

25. E.H. Lee and L.K. Mansur, J. Nucl. Mat. 141-143 (1986) 695-702.

26. J.B. Whitley, G.L. Kulcinski, P. Wilkes, and J. Billen, J. Nucl. Mat. 85 & 86 (1979) 701-706.

27. R.L. Sindelar, R.A. Dodd, and G.L. Kulcinski, "Comparison of Depth-Dependent Microstructures of Ion-Irradiated Type 316 Stainless Steels," in Effects of Radiation on Materials: Twelfth International Symposium, ASTM STP 870 (1985) 330-343.

28. J.T. Buswell, S.B. Fisher, J.E. Harbottle, and D.I.R. Norris, "High-Voltage Electron Microscope Studies of Void Swelling," in Physical Metallurgy of Reactor Fuel Elements, J.E. Harris and E.C. Sykes, Eds. (1975) 170-174.

29. R.L. Sindelar, R.A. Dodd, and G.L. Kulcinski, "A Note on Reactive Gas Charging During Pre-Irradiation Specimen Preparation," in Damage Analysis and Fundamental Studies, DOE/ER-0046/21 (1985) 148-150.

30. J.T. Buswell, "The Growth of Voids in Stainless Steel," in ref. 5 (1971) 283-291.

31. M.J. Makin and G.P. Walters, "The Effect of Void Density and Carbon Concentration on the Swelling of Type 316 Austenitic Steel Irradiated in the HVM," in The Physics of Irradiation Produced Voids, R.S. Nelson, Ed. (1974) 299-312.

32. J.J. Laidler, B. Mastel, and F.A. Garner, "Swelling in Electron-Irradiated Type 316 Stainless Steel," in Properties of Reactor Structural Alloys After Neutron or Particle Irradiation, ASTM STP 570 (1975) 415-468.

33. J.J. Laidler, "Simulation of Neutron-Induced Swelling in Fast Test Reactor Fuel Cladding," in ref. 28 (1975) 175-179.

34. M.J. Makin and G.P. Walters, "Simulation of Fast Reactor Void Swelling in the Harwell High-Voltage Microscope," in ref. 28 (1975) 180-185.

35. A. Hishinuma, Y. Katano, K. Fukaya, and K. Shiraishi, J. Nucl. Sci. and Tech. 13 (1976) 656-662.

36. V. Levy, N. Azam, L. LeNaour, G. Didout, and J. Delaplace, "Effect of Structure and Alloying Elements on Void Formation in Austenitic Steels and Nickel Alloys," in Radiation Effects in Breeder Reactor Structural Materials, M.L. Bleiberg and J.W. Bennett, Eds. (1977) 709-725.

37. A. Hishinuma, Y. Katano, and K. Shiraishi, J. Nucl. Sci. and Tech. 15 (1978) 690-696.

38. R.W. Powell and G.R. Odette, J. Nucl. Mat. 85 & 86 (1979) 695-699.

39. M.J. Makin, G.P. Walters, and A.J.E. Foreman, J. Nucl. Mat. 95 (1980) 155-170.

40. B.N. Singh, T. Leffers, M.J. Makin, G.P. Walters, and A.J.E. Foreman, J. Nucl. Mat. 103 & 104 (1981) 1041-1045.

41. N. Igata, Y. Kohno, M. Saito, and H. Tsunakawa, J. Nucl. Mat. 103 & 104 (1981) 1047-1051.

42. A. Hishinuma, Y. Katano, and K. Shiraishi, J. Nucl. Mat. 103 & 104 (1981) 1063-1067.

43. L.E. Thomas and D.S. Gelles, J. Nucl. Mat. 108 & 109 (1982) 490-503.

44. N. Igata, Y. Kohno, N. Tanabe, T. Fujihira, and H. Tsunakawa, "The Effect of Nitrogen on Void Swelling of Stainless Steel," in Effect of Radiation on Materials: Eleventh Conference, ASTM STP 782, H.R. Brager and J.S. Perrin, Eds. (1982) 906-916.

45. V.N. Voevodin, B.V. Matvienko, B.N. Singh, and T. Leffers, "Effects of Cold Work on Void Nucleation and Growth in an Austenitic Stainless Steel During Heavy-Ion and Electron Irradiation," in Dimensional Stability and Mechanical Behaviour of Irradiated Metals and Alloys, Vol. 1, British Nuclear Energy Society (1983) 33-36.

46. J. Cawley and F.B. Pickering, "Some Effects of Alloying Elements on Void Swelling in High Purity Fe-Ni-Cr Alloys," in ref. 45 (1983) 77-81.

47. N. Igata, Y. Kohno, N. Tanabe, F. Rotman, and H. Tsunakawa, J. Nucl. Mat. 122 & 123 (1984) 219-223.

48. H. Takahashi, S. Ohnuki, H. Osanai, T. Takeyama, and K. Shiraishi, J. Nucl. Mat. 122 & 123 (1984) 327-331.

49. Y. Katano, K. Nakata, S. Jitsukawa, T. Aruga, and K. Shiraishi, J. Nucl. Mat. 133 & 134 (1985) 530-534.

50. T. Takeyama, S. Ohnuki, and H. Takahashi, J. Nucl. Mat. 133 & 134 (1985) 571-574.

51. T. Sawai, K. Fukai, S. Hamada, K. Suzuki, and A. Hishinuma, J. Nucl. Mat. 141-143 (1986) 444-447.

52. J.F. Stubbins, J. Nucl. Mat. 141-143 (1986) 748-753.

53. S. Kojima, Y. Sano, T. Yoshiie, N. Yoshida, and M. Kiritani, J. Nucl. Mat. 141-143 (1986) 763-766.

54. N. Igata, Y. Kohno, and J. Nishimura, J. Nucl. Mat. 141-143 (1986) 790-793.

55. H. Watanabe, A. Aoki, H. Murakami, T. Muroga, and N. Yoshida, "Effects of Phosphorous on Defect Behavior, Solute Segregation and Void Swelling in Electron Irradiated Fe-Cr-Ni Alloys, to be published in J. Nucl. Mat.

56. D.J. Mazey, J. Nucl. Mat. 35 (1970) 60-66.

57. G.L. Kulcinski, J.J. Laidler, and D.G. Doran, Rad. Eff. 7 (1971) 195-202.

58. J.J. Laidler, "Suppression of Void Formation in Stainless Steel," in ref. 6 (1972) 174-186.

59. A. Taylor and S.G. McDonald, "Void Formation in Proton- and Nickel-Irradiated Stainless Steel," in ref. 6 (1972) 499-510.

70. K. Miyahara, N.H. Packan, and N. Igata, "The Effect of Pulsed Irradiation on Void Swelling in a 'Pure' 316 Stainless Steel," in ref. 44 (1982) 941-952.

71. E.H. Lee, N.H. Packan, and L.K. Mansur, J. Nucl. Mat. 117 (1983) 123-133.

72. A. Kohyama, G. Ayrault, and A.P.L. Turner, J. Nucl. Mat. 117 (1983) 151-158.

73. A. Kumar and F.A. Garner, J. Nucl. Mat. 117 (1983) 234-238.

74. T. Aruga, Y. Katano, and K. Shiraishi, J. Nucl. Mat. 122 & 123 (1984) 191-195.

75. A. Kohyama, G. Ayrault, and N. Igata, J. Nucl. Mat. 122 & 123 (1984) 224-229.

76. R.L. Sindelar, G.L. Kulcinski, and R.A. Dodd, J. Nucl. Mat. 133 & 134 (1985) 544-548.

77. K. Nakata, T. Kato, and I. Masaska, J. Nucl. Mat. 148 (1987) 185-193.

78. W.G. Johnston, J.H. Rosolowski, A.M. Turkalo, and T. Lauritzen, J. Nucl. Mat. 54 (1974) 24-40.

79. F.A. Garner, J. Nucl. Mat. 133-134 (1985) 113-118.

80. F.A. Garner, H.R. Brager, M.L. Hamilton, R.A. Dodd, and D.L. Porter, Rad. Effects 101 (1986) 37-53.

CHAPTER 5

EXPERIMENTAL PROCEDURE

A. Heavy Ion Irradiation Facility

The ion irradiations in this study are performed at the University of Wisconsin Heavy Ion Irradiation Facility. This facility, schematically represented in Figure 5.1 consists of the SNICS negative ion source, the EN Tandem accelerator, the irradiation target stand, and associated beam handling components. The irradiating ion is 15 MeV Ni^{3+} and the injected-gas ion is 6 MeV O^{2+}. The details of the facility have been described elsewhere [1]. The SNICS ion source, developed by Billen and Richards [2,3], produces negative ions by cesium sputtering of a cylindrical cathode target. In this case a nickel cathode is utilized for both the oxygen injections and the nickel bombardment. The oxygen source current is large, around 20 μA, for the first several hours of source usage. After a few hours, the oxygen beam diminishes and the nickel current rises to as much as 40 μA. The negative ion is extracted at around 25 kV from the source and passes through a selecting magnet so that the desired negative ion species may be steered through the accelerator. A 90° electrostic mirror reflects the source ion into the axis of the accelerator. The negative ion passes through a quadrupole triplet into the accelerator. The ion accelerates from 25 kV to several million volts at the dome of the accelerator. Passing through a N_2 gas stripper, the now positively charged ion is repelled towards the

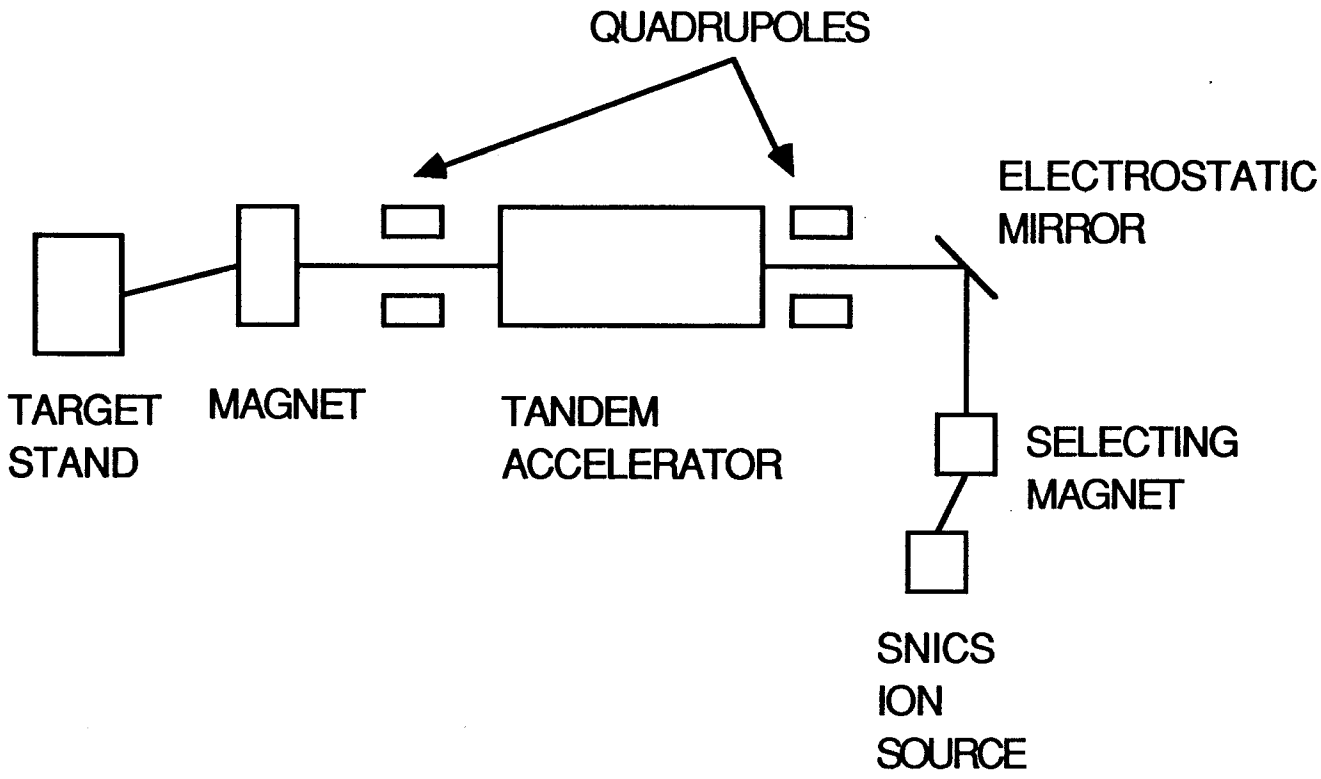

Figure 5.1. Schematic of University of Wisconsin Heavy Ion Irradiation Facility.

target chamber. The ion emerges from the accelerator with an energy $E = qV(1+n)$, where q is the unit of charge, V is the accelerator dome voltage, and n is the charge state of the ion. The gas stripper yields a distribution of charge states that depends on the dome voltage. The desired charge state is selected by a quadrupole lens. Charge state analysis at the target location is performed by Rutherford scattering analysis of the beam scattered by a gold foil into a solid state detector. Charge state analysis shows that ~ 95%+ of the beam is of the desired charge state for both nickel and oxygen. The remainder of the beam consists of lesser charge states

The target chamber is aligned ~ 1° off the accelerator axis in order to prevent neutrals from reaching the sample. A bending magnet steers the beam onto the target. The target chamber was originally designed by Smith and Lott [1,4]. Modifications to the sample holder were made by Knoll [5]. Further modifications are also made in an effort to eliminate hydrocarbon contamination of the vacuum by the pumping systems. Two differential pumping stages and two pumps are eliminated so that only a large orbitron pump evacuates the entire sample stand. A normal operating pressure is 1.0×10^{-6} torr at 650°C. The ion beam is collimated by a 3 mm mask aperture before reaching the target. The samples are 1 cm x 1/2 cm foils covered by a Ta face plate with a 3 mm hole on the same axis as the 3 mm aperture. The sample holder can hold up to 8 foils (or discs). Knoll [5] has modified the sample holder so that each foil is isolated from

the others when heated. When the irradiated foil is heated to 650°C, the neighboring foils never exceed 300°C.

For the case of oxygen implantation, the dome voltage used is V=2.0 MeV and the charge state selected is 2+ (n=2). This yields an oxygen implantation energy of 6.0 MeV. The nickel irradiation is performed with 15 MeV Ni^{3+} ions (V=3.8, n=3). Oxygen implantation rates are typically on the order of 0.1 appm/sec and dose rates are on the order of $1x10^{-3}$ dpa/sec at 1 μm from the front surface.

B. Specimen Preparation and Analysis

An Fe-Ni-Cr ternary steel in the composition range of the Magnetic Fusion Program's Prime Candidate Alloy (PCA) is used in this study. The Inland Steel Company provided 0.5 mm thick sheet form ternary steel with the composition shown in Table 5.1. Both the oxygen and carbon contents are greater than desired. A series of treatments, discussed below are applied in order to reduce the impurity levels. The major alloying elements are determined by energy dispersive spectroscopy using a known standard for quantitative comparison. The Analytical Chemistry Group at Los Alamos National Laboratory performed vacuum fusion analysis on the treated steel. Results are also given in Table 5.1.

Table 5.1. Ternary Composition

Material	Weight %							
	Fe	Ni	Cr	C	P	S	Al	O_2
As-Received	Bulk	16	13.5	.215	.008	.008	-	.0062
Treated	Bulk	17	13	.016	.008	.008	.003	.0060

B.1. Pre-Irradiation Specimen Preparation

Minimization of the minor alloying and impurity elements, especially oxygen, are of high priority in preparing the steel. Unfortunately, in steel, low oxygen levels can only be achieved by adding other impurities. It is impossible to get an oxygen free pure ternary steel. The treatment detailed here is considered the best compromise for achieving low oxygen content while maintaining maximum purity.

Strips of the steel plate are cut to 15 cm x 2 cm and cleaned in 50% HNO_3 50% H_2O. A quartz tube with a 3 cm inner diameter open at both ends is cleaned in 10% HF 90% H_2O. The strip is placed inside the tube and inserted in a horizontal annealing furnace. Wet H_2 gas at 1000°C flows across the strip for $2x10^5$ sec in order to decarburize the steel. Next, the steel strip is annealed in flowing argon at 1000°C for 1 hour to remove hydrogen. The annealed strip is bead blasted to clear the surface. The strip is then arc melted along with Johnson Mathey 99.999% pure aluminum. The arc melted ingot is bead blasted to clean the surface. The ingot is cold rolled 50%,

annealed in argon at 1000°C, and bead blasted. This last procedure is repeated three times until a sheet 0.38 mm thick is obtained. Foils, 1/2 cm x 1 cm, are cut with a diamond saw.

The steel foils are sequentially ground on 240, 320, 540, and 600 grit abrasive paper. Mechanical polishes with 0.3 μm and 0.05 μm alumina slurry on a rotary mechanical polisher are performed. Note that no electropolishing step is added in order to avoid introduction of additional residual gas to the speciments prior to irradiation [6-8]. The polished foils are kept in an inert atmosphere until loaded in the carousel holder for irradiation.

B.2. Post-Irradiation Specimen Preparation

The cross-section specimen preparation technique for transmission electron microscopy analysis, introduced by Spurling and Rhodes [9], is used in this study. This technique permits the damage range to be viewed in toto, as depicted in Figure 5.2. This is opposed to the traditional backthinning method, where only a single depth is sampled. A recent paper outlines the transverse or cross-section technique for copper, nickel, copper alloys, 300 series austenitic stainless steel, and low chromium ferritic steels [10]. This study introduces several modifications to the method for preparing cross-section samples of 300 series stainless steels.

First, the irradiated foil is lightly swabbed with a weak slurry of 0.3 μm alumina on both faces. The foil is then degreased for 20 minutes in an ultrasonically agitated acetone bath. The clean foil

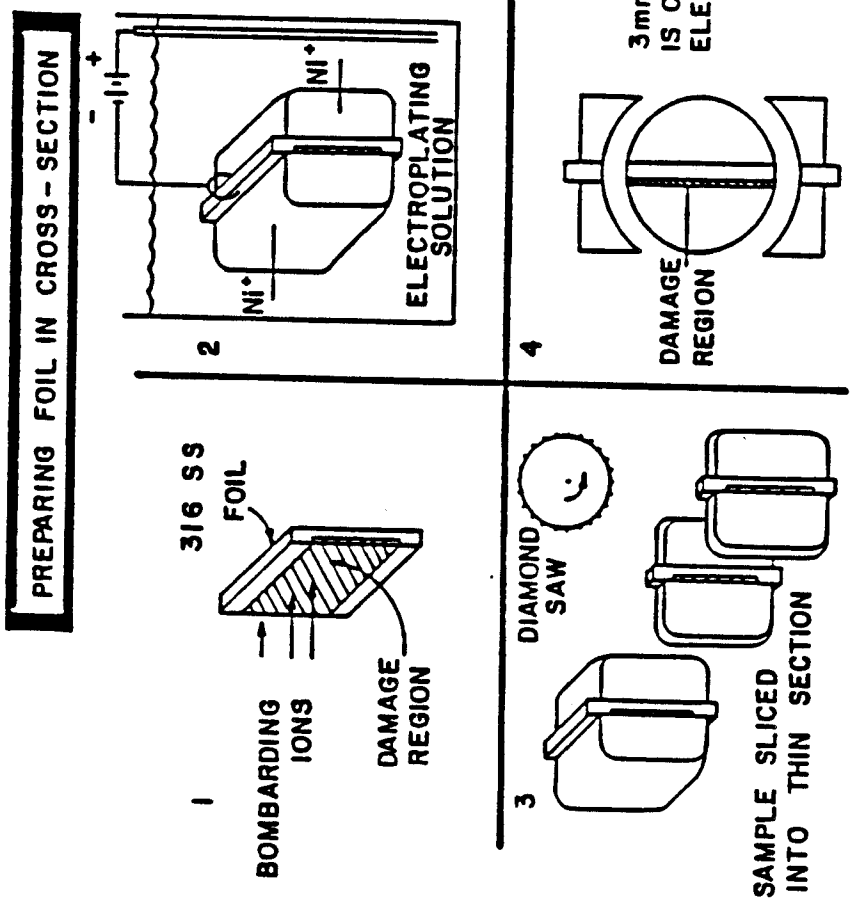

Figure 5.2. Sample preparation technique for obtaining TEM samples with entire irradiated region in view. From ref. [10].

is placed in a plexiglass holder with a 0.5 cm x 0.5 cm window. Below the window is a 0.5 cm diameter hole extending to the bottom of the holder. This cylindrical hole permits agitation of the plating surface from below. Above the window the holder is beveled in order to facilitate the removal of gas bubbles that occur at the cathode surface. A small hole in the top of the holder allows a metal rod coated with stop-off lacquer, except at the tip, to act as an electrical conduit to the sample. The plating holder is illustrated in Figure 5.3. Good electrical contact between the electrode rod and the sample is essential for a strong plating bond.

The holder is immersed in a room temperature striking bath. The strike solution consists of 30g $NiCl_2$, 125 ml H_2O, and 20 ml HCl. A nickel screen is also submerged to provide the opposite electrode to the sample. Vigorous agitation is applied to the solution by a teflon-coated stirring bar magnet. Agitation is necessary in order to deter sticking of the hydrogen bubbles that evolve during electroplating to the surface. The sample is made anodic for 2.5 sec at a current density of 200 mA/cm^2. The polarity is then reversed and the sample is plated with nickel for 10 minutes in the striking bath at a current density of 70 mA/cm^2.

Next, the sample holder is removed and placed in the plating bath. The plating solution is comprised of 16.75g $NiCl_2$, 16.75g $NiSO_4$, 6.75g H_3BO_3, and 112 ml H_2O. Added to this solution is 0.1g sodium lauryl sulfate, $CH_3(CH_2)_{11}OSO_3Na$. This organic compound is added as an anti-wetting agent in order to eliminate porosity of the

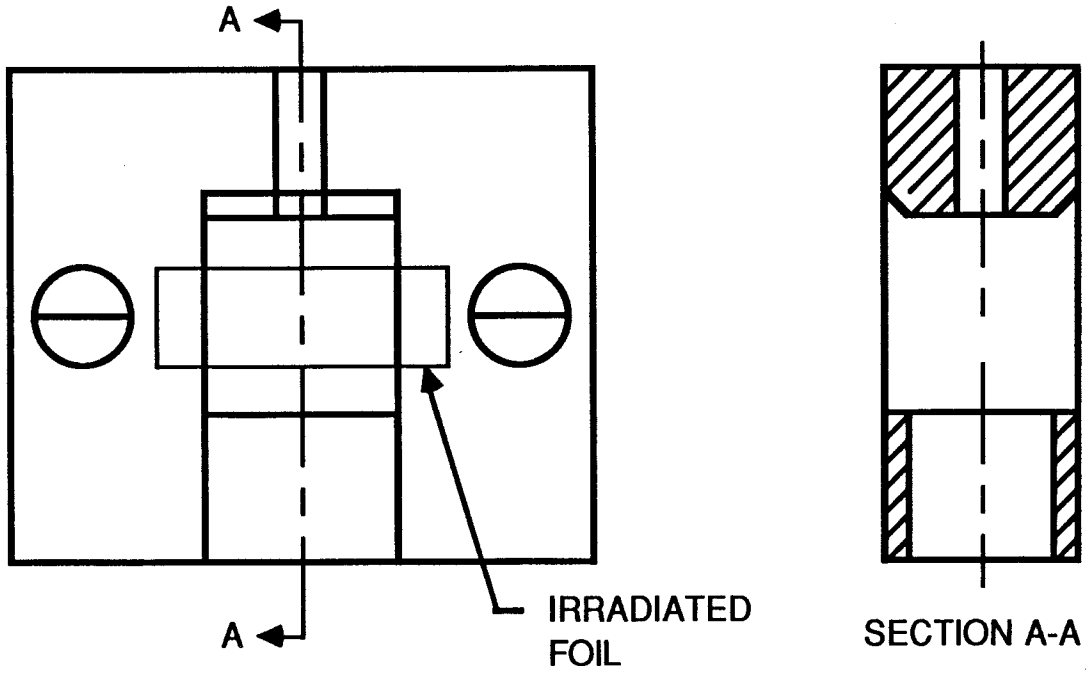

Figure 5.3. Plating holder for cross-section specimen preparation.

plating. The plating bath is maintained between 65 and 70°C. Vigorous agitation is applied by a teflon-coated stirring bar magnet. Two nickel blocks, one on each side of the holder, are immersed to act as sacrificial anodes during plating. The blocks are placed parallel to and about 0.5 cm from the sample holder faces. The sample is made anodic for 10 sec at a current density of 200 mA/cm^2. The polarity is then reversed and the sample is plated with nickel at a current density of 60 mA/cm^2. A plating layer sufficiently thick to obtain 3 mm discs is achieved after 24 to 30 hours.

After electroplating, the sample is removed from the holder and mounted in epoxy with the irradiated spot marked. The hardened epoxy block is placed in a diamond saw holder and transverse slices of the plated foil are cut. Each slice is about 0.25 mm thick. The slices from the irradiated zone are mechanically polished and etched in Villelas reagent. This etching is used to highlight the interface between the nickel plating and the steel foil. Sindelar [10] noticed that this etching also can highlight the irradiated zone in the steel so that an irradiated band is visible. The slices are either punched or slurry drilled to obtain 3 mm TEM discs. The slurry drill is utilized when a poor plating bond exists.

Electropolishing of the TEM discs is a two step process due to the different thinning rates of steel and nickel. The disc is first lacquered on one face. The entire face is lacquered except for a thin strip along the irradiated interface. The lacquer should stop in the nickel approximately 0.01 mm from the interface and in the

60. W.G. Johnston, J.H. Rosolowski, A.M. Turkalo, and T. Lauritzen, "Nickel Ion Bombardment of Types 304 and 316 Stainless Steels: Comparison with Fast Reactor Swelling Data," in Effects of Radiation on Substructure and Mechanical Properties of Metals and Alloys, ASTM STP 529 (1973) 213-227.

61. D.J. Mazey and S. Francis, "Observations of Dislocation Structure and Cavities Formed by Annealing in Type 316 Steel After Ion Irradiation at Ambient Temperature," in ref. 31 (1974) 257-262.

62. J.L. Brimhall, K. Uematsu, and T. Nishikawa, "Void Formation in an Ion Bombarded Cold-Worked Stainless Steel," in ref. 32 (1975) 488-504.

63. E.A. Kenik, J. Nucl. Mat. 85 & 86 (1979) 659-663.

64. W.J. Choyke, J.N. McGruer, and J.R. Townsend, J. Nucl. Mat. 85 & 86 (1979) 647-651.

65. N.H. Packan and K. Farrell, J. Nucl. Mat. 85 & 86 (1979) 677-681.

66. K. Farrell and N.H. Packan, J. Nucl. Mat. 85 & 86 (1979) 683-687.

67. K. Shiraishi, T. Aruga, and Y. Katano, J. Nucl. Mat. 103 & 104 (1981) 1053-1057.

68. N.H. Packan, J. Nucl. Mat. 103 & 104 (1981) 1029-1033.

69. K. Farrell and N.H. Packan, "Comparison of Neutron and Heavy-Ion Damage in a Single-Phase Austenite," in ref. 44 (1982) 953-962.

steel approximately 0.04 mm from the interface. After drying completely, the disc is single jet electropolished for 20 to 50 sec at -10°C and a current of 90 mA (2-5 V) in a solution of 30% HNO_3 and 70% methanol. The lacquer is then stripped in acetone. The next step is to twin-jet electropolish to perforation (several minutes) at room temperature and a current of 67 mA (25-30 V) in a solution of 10% perchloric acid, 90% acetic acid, 20 g/l Cr_2O_3, and 10 g/l $NiCl_2$. Electropolishing is performed on a Fischione Twin-Jet Electropolisher.

Often the hole appears off the interface and/or has insufficient thin area for electron microscopy. Extension of the thin area is achieved by ion beam milling on a Gatan Model 600 Duo Mill. The disc is cooled to liquid nitrogen temperature and sputtered with a dual argon beam operating at 6 kV, 0.3 mA per beam, and sputtering angle of 12 to 15°. Before analysis the sample is sputtered for 30 minutes at 11°, 2 kV, 0.5 mA per gun to remove any surface damage introduced by the higher voltage milling.

B.3. Specimen Analysis

The electron microscopy performed in this study is done on a JEOL TEMSCAN 200CX electron microscope operating at 200 kV. The 200CX is equipped with a double tilt side entry goniometer. Specimen thickness is measured by stereo microscopy and checked, when possible, with thickness fringes. Stereo pair thickness measurements are conducted on a Hilgar Watts stereoviewer. The foil thickness, t, is

given by

$$t(nm) = \frac{px10^6}{2M \sin(\frac{\theta}{2})} \tag{5.1}$$

where p is the image parallax in mm measured from features on opposite surfaces of the foil, M is the magnification of the negatives analyzed, and θ is the tilt angle between the negatives. For consistency in this study, M is always 100,000 and θ was around 10°.

Void sizes are measured on a Zeiss particle size analyzer. All void data are determined in 0.25 μm wide intervals along the incident direction. The average void size, $\bar{d}$, is given by

$$\bar{d} = \frac{1}{N} \sum n_i d_i \tag{5.2}$$

where N is the total number of voids, n_i is the number of voids with size d_i. Assuming the void size distribution is normal yields a standard deviation

$$\sigma_d = \left(\frac{\sum n_i (d_i - \bar{d})^2}{N - 1}\right)^{1/2} \tag{5.3}$$

The void density, N_V, is calculated as

$$N_V = \frac{N}{V} \tag{5.4}$$

where V is the measured volume. The error analysis of the number density assumes that the thickness uncertainty and the standard deviation in void number are independent errors. Then the uncertainty in number density, δN_v, is given by

$$\frac{\delta N_v}{N_v} = \left[\left(\frac{\delta t}{t}\right)^2 + \left(\frac{\sqrt{N}}{N}\right)^2\right]^{1/2} \qquad (5.5)$$

where $\frac{\delta t}{t}$ is the fractional error in thickness measured (30%) and the standard deviation in void number assumes a normal distribution.

References for Chapter 5

1. H.V. Smith and R.G. Lott, Nucl. Instr. Methods 143 (1977) 125-132.
2. J.H. Billen and H.T. Richards, "SNICS-A Source of Negative Ions by Cesium Sputtering," in Proceedings of the Symposium of Northeastern Accelerator Personnel, CONF-781051 (1978) 137-146.
3. J.H. Billen, IEEE Trans. Nucl. Sci. NS-28 (1981) 1535-1539.
4. R.G. Lott, "The Effect of Nickel and Nitrogen on Void Formation in Vanadium," Ph.D. Thesis, University of Wisconsin, Madison, 1981.
5. R.W. Knoll, "Effects of Heavy-Ion Irradiation on the Phase Stability of Several Copper-Base Alloys," Ph.D. Thesis, University of Wisconsin, Madison, 1981.

6. J.T. Buswell, S.B. Fisher, J.E. Harbottle, and D.I.R. Norris, "High Voltage Electron Microscope Studies of Void Swelling," in Physical Metallurgy of Reactor Fuel Elements, J.E. Harris and E.C. Sykes, Eds. (1975) 170-174.

7. J.B. Whitley, "Depth Dependent Damage in Heavy-Ion Irradiated Nickel," Ph.D. Thesis, University of Wisconsin, Madison, 1978.

8. R.L. Sindelar, R.A. Dodd, and G.L. Kulcinski, "A Note on Reactive Gas Charging During Pre-Irradiation Specimen Preparation," in Damage Analysis and Fundamental Studies, DOE/ER-0046121 (1985) 148-150.

9. R.A. Spurling and C.G. Rhodes, J. Nucl. Mat. 44 (1972) 341-344.

10. S.J. Zinkle and R.L. Sindelar, Nucl. Instr. Methods in Phys. Res. B16 (1986) 154-162.

CHAPTER 6

EXPERIMENTAL RESULTS

A. Unirradiated Microstructure

The microstructure of the unirradiated Fe-17 Ni-13 Cr alloy used for this study is that of a well annealed material. The average grain diameter is measured to be ~ 20 μm according to standard techniques [1]. An electron micrograph of this alloy, Figure 6.1, reveals a low dislocation density and a heterogeneous distribution of widely spaced inclusion clusters. The dislocation density, measured by the random line intersection method at various operating reflections [2], is $\rho_d \sim 2 \times 10^{13}/m^2$. Figure 6.2 is an enlargement of the cluster A in Figure 6.1. This cluster contains three distinct inclusions. Energy dispersive spectroscopy (EDS) reveals that these are aluminum-bearing particles. The diffraction pattern in Figure 6.2 reveals a spot pattern as well as a ring pattern. A high density of fine particles can be seen in the vicinity of this inclusion cluster as well as others. These particles are readily visible in Figure 6.1 at position B, where it appears that the larger inclusions fell out of the sample. The ring pattern corresponds to that of FeO. Also, inclusions appear only in about half the grains. No carbide precipitates, such as $M_{23}C_6$ or M_6C, are found in the alloy. Finally, it should be noted that no inclusions were found in the irradiated regions of the ion-bombarded alloys.

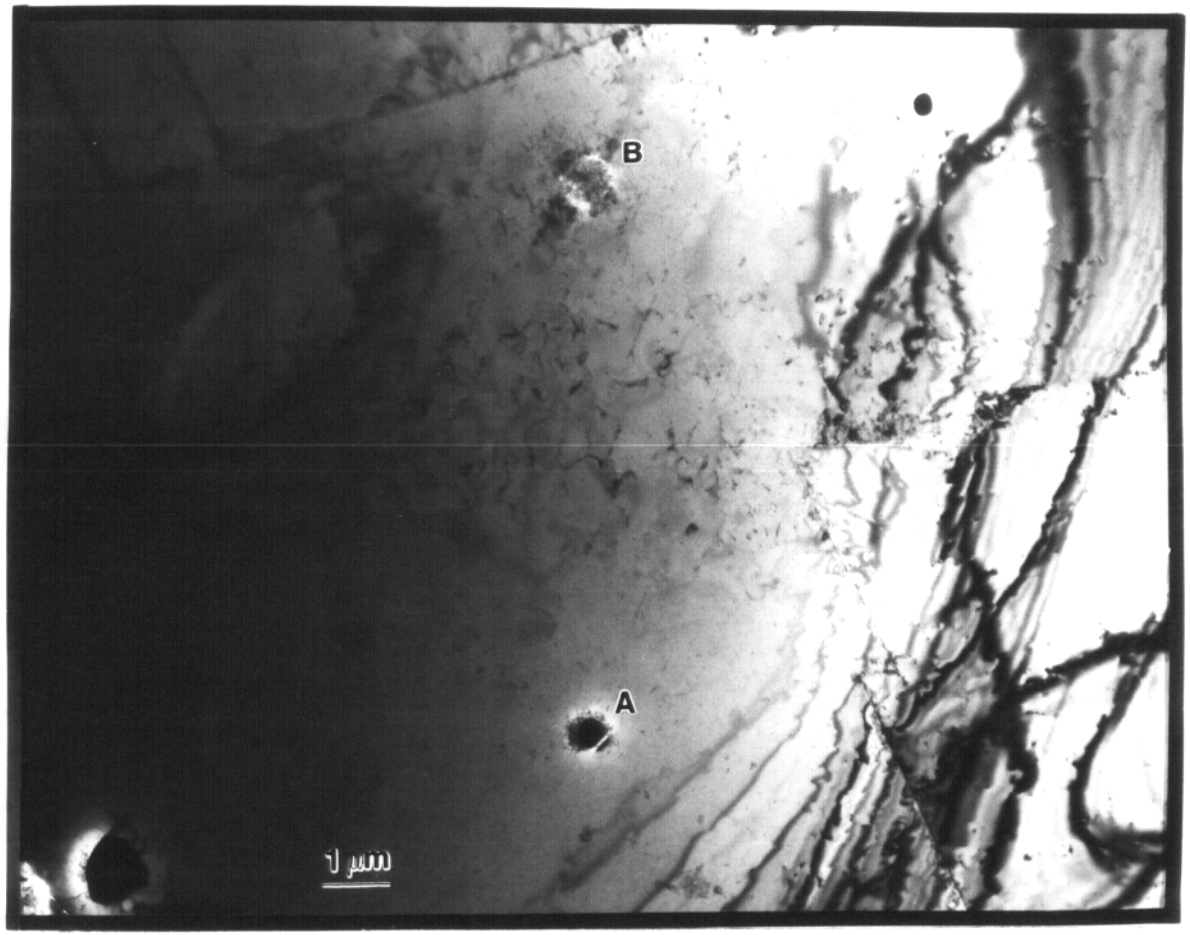

Figure 6.1. As-treated microstructure of Fe-17Ni-13Cr. Inclusion cluster marked at A and hole of former cluster marked at B.

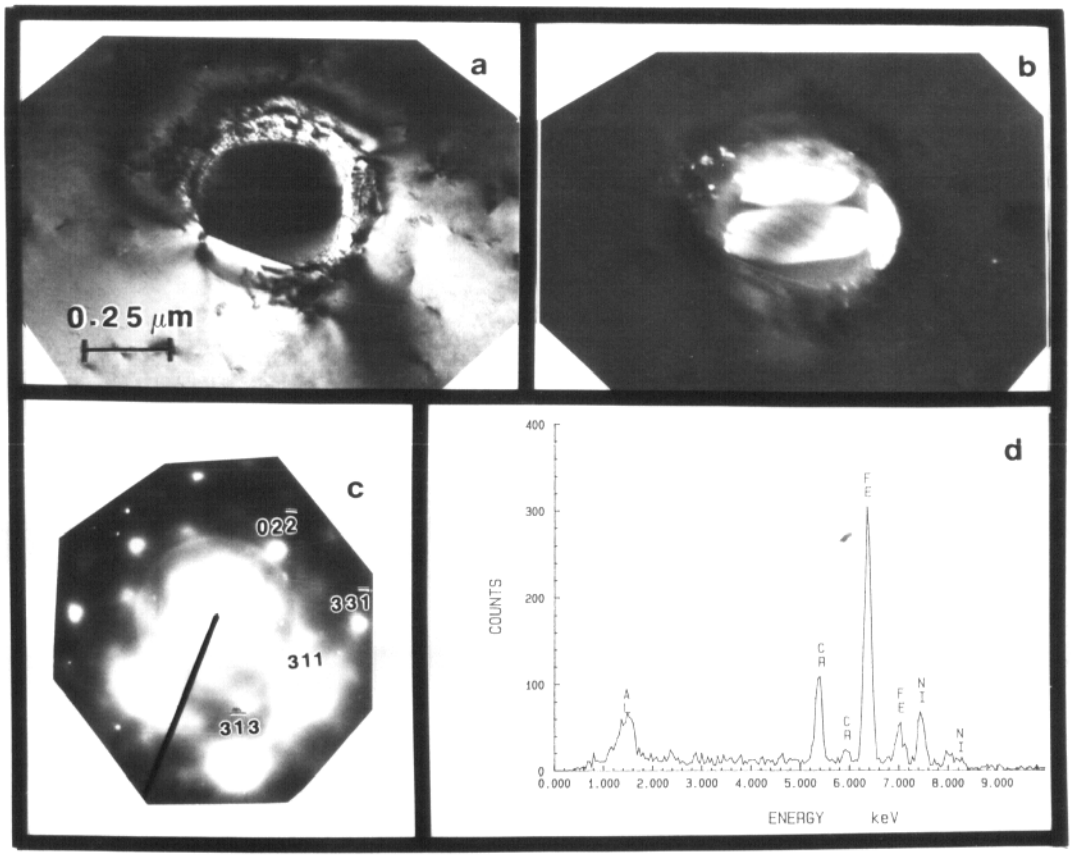

Figure 6.2. Inclusion cluster A in a) bright field and b) dark field revealing three individual inclusions and a high density of small particles. c) Selected area diffraction shows spot and ring patterns from cluster. d) EDS spectrum of large inclusions.

B. Irradiated Microstructure

The conditions under which the alloy is irradiated are presented in Table 6.1. The irradiation temperature ranges from 550 to 650°C in steps of 50°C. Room temperature oxygen preinjections vary from 10 to 1000 appm. Control samples at each temperature do not receive an oxygen preimplantation. The residual oxygen content in all samples is 160 appm O as analyzed by vacuum fusion techniques. The ion fluence (and dose) in all cases is identical, although the dose rate varies up to a factor of two. A typical micrograph of the cross-sectional view of the irradiated region is displayed in Figure 6.3. Table 6.2 lists the void density, N_v, the average void diameter, $\bar{d}$, and the percent volume swelling, $\frac{\Delta V}{V}$, measured at a depth of 1 and 2 μm in all cases.

B.1. Swelling Response at 550°C

The results of the 550°C irradiation yields the greatest information on the effect of oxygen on the swelling response. Figure 6.4 presents a comparison of the resultant void size and density at the various oxygen implantation levels. These micrographs are all taken from 1 to 2 μm from the interface. The void diameter in the unimplanted sample is much greater than the diameters of the implanted specimens. It also appears from Figure 6.4 that the void diameter increases slightly with increasing injected oxygen content. This trend is confirmed throughout the entire damage range as shown in Figure 6.5.

Table 6.1. 15 MeV Ni-Ion Irradiation Conditions of Fe-17Ni-13Cr Alloy

Irradiation Temperature (°C)	Injected Oxygen (appm)	Injection Rate (appm/sec)	Ion Fluence (10^{16} ions/cm^2)	Dose Rate at 1 μm[(a)] (10^{-4} dpa/sec)	Dose Rate at Damage Peak[(b)] (10^{-3} dpa/sec)
550	0	-	1.3	7.0	2.8
550	10	0.13	1.3	8.2	3.2
550	100	0.13	1.3	8.8	3.5
550	300	0.10	1.3	7.0	2.8
550	1000	0.12	1.3	13.4	5.3
600	0	-	1.3	12.2	4.8
600	100	0.12	1.3	12.2	4.8
650	0	-	1.3	7.0	2.8
650	100	0.12	1.3	6.4	2.5

(a) Total dose at 1 μm is 5 dpa.

(b) Total dose at damage peak is 15 dpa.

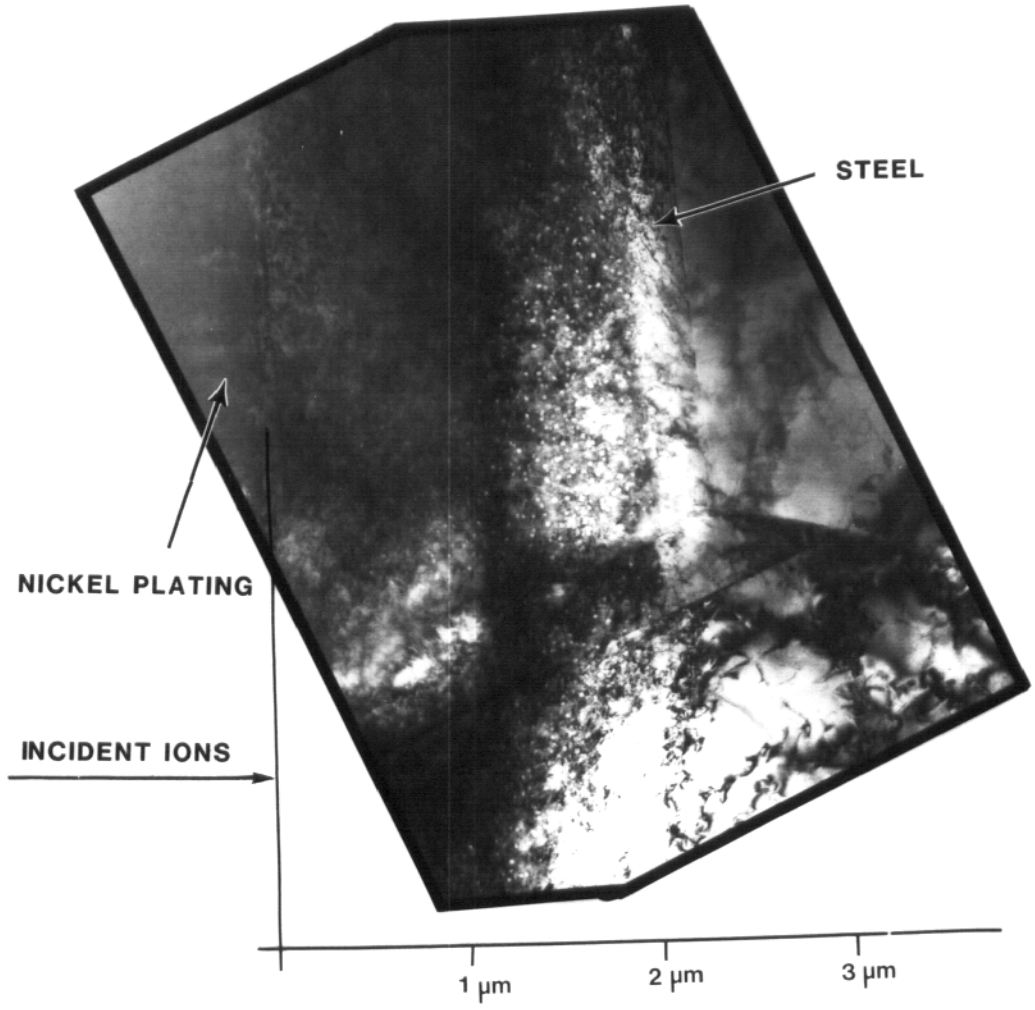

Figure 6.3. Cross-section of unimplanted Fe-17Ni-13Cr irradiated with 15 MeV Ni ions to a fluence of 1.3 E16 ions/sq. cm. at 600 °C showing entire irradiated region.

Table 6.2. Swelling Response of Fe-17Ni-13Cr to 15 MeV Nickel-Ion Irradiation[a)]

Temperature (°C)	Injected Oxygen Concentration (appm)	Response at 1 μm[b)]			Response at 2 μm[c)]		
		N_v (10^{20}/m)	$\bar{d}$ (nm)	$\frac{\Delta V}{V}$ (%)	N_v (10^{20}/m^3)	$\bar{d}$ (nm)	$\frac{\Delta V}{V}$ (%)
550	0	2.4	21	0.13	3	29	0.4
600	0	29	25	2.4	13	30	2.0
650	0	1.0	17	0.04	3	24	0.23
550	10	16	10	0.09	10	9	0.04
	100	11	11	0.08	23	12	0.25
	300	2.6	9	0.011	5.3	10	0.03
	1000	15	15	0.25	4	14	0.06
600	100	18	23	1.2	13	15	0.26
650	100	2.4	21	0.13	19	30	2.8

a) Nickel fluence = 1.3×10^{16} ions/cm^2
b) Dose @ 1 μm = 5 dpa
c) Dose @ 2 μm = 15 dpa (peak damage depth)

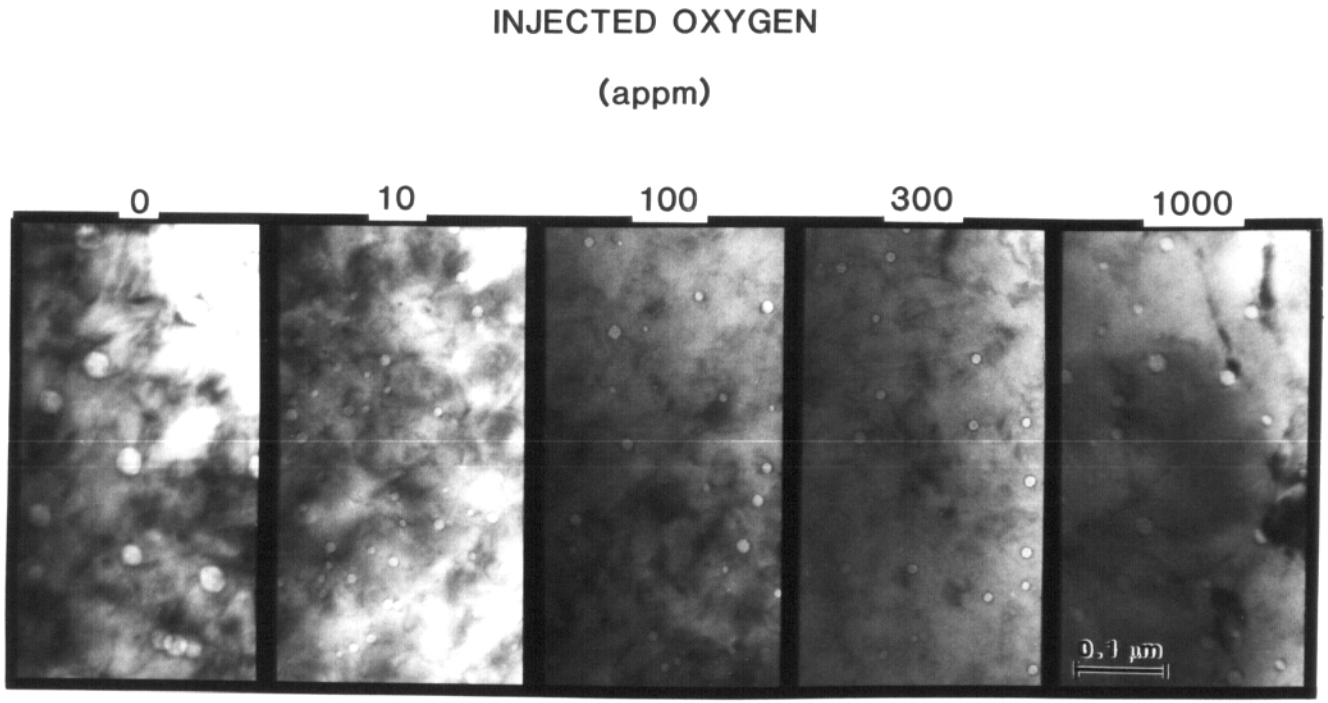

Figure 6.4. Comparison of the swelling of Fe-17Ni-13Cr to 15 MeV Ni-ion irradiation to a fluence of 1.3 E16 ions/sq. cm. at 550 °C with varying injected oxygen concentration. Residual oxygen is 160 appm O. Data taken in oxygen implanted region (1.2 - 1.5 μm and 8 dpa).

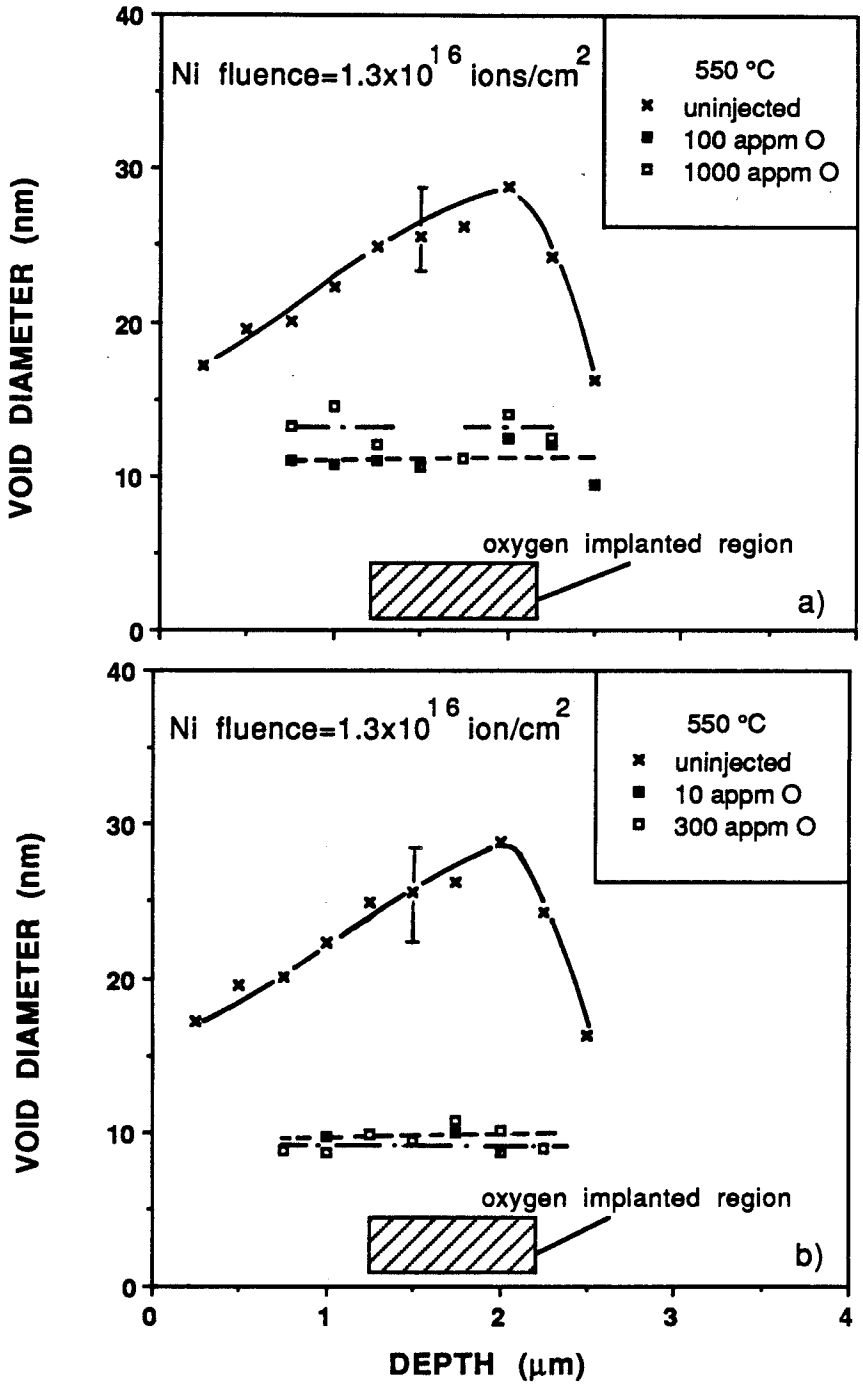

Figure 6.5. Void diameter as a function of depth and oxygen concentration at 550 °C in Ni-irradiated Fe-17Ni-13Cr.

In Figure 6.5, the data is recorded as measured with the exception of the 100 appm case. The raw data for this specimen exhibits void formation out to a 3.25 μm depth. All other specimens exhibited end-of-range swelling at depths no greater than 2.5 μm. This sample also exhibited a greater near-surface void free zone (> 1 μm) compared to the other sample (~ .5 μm). It was noticed that in the sectioning step of the sample preparation for the 550°C, 100 appm O specimen that the sample had slipped and was being sliced at ~ 45° from the normal. Rather than obtaining data perpendicular to the incident direction, the angle was only 45°. Thus the apparent range was increased by a factor of $\sqrt{2}$. Therefore, the recorded depths of the data were divided by $\sqrt{2}$ in order to obtain the void distribution along the incident direction.

The average void diameter for the oxygen injected specimens falls in a band between 9 and 15 nm. Also, the average diameter in these specimens is relatively constant with increasing depth (and dose). Only the uninjected sample shows an increase in diameter with increasing depth up to 2 μm. As the dose decreases further into the sample, the average diameter drops to lower values. A typical error bar is also given in Figure 6.5.

A comparison of the void diameter distribution, taken over the full damage range, for all the 550°C irradiated specimens is given in Figure 6.6, see figure comment. This representation of the data shows that the size distribution for the oxygen injected alloy is relatively narrow, with 60 to 80% of the voids within 2 nm of the

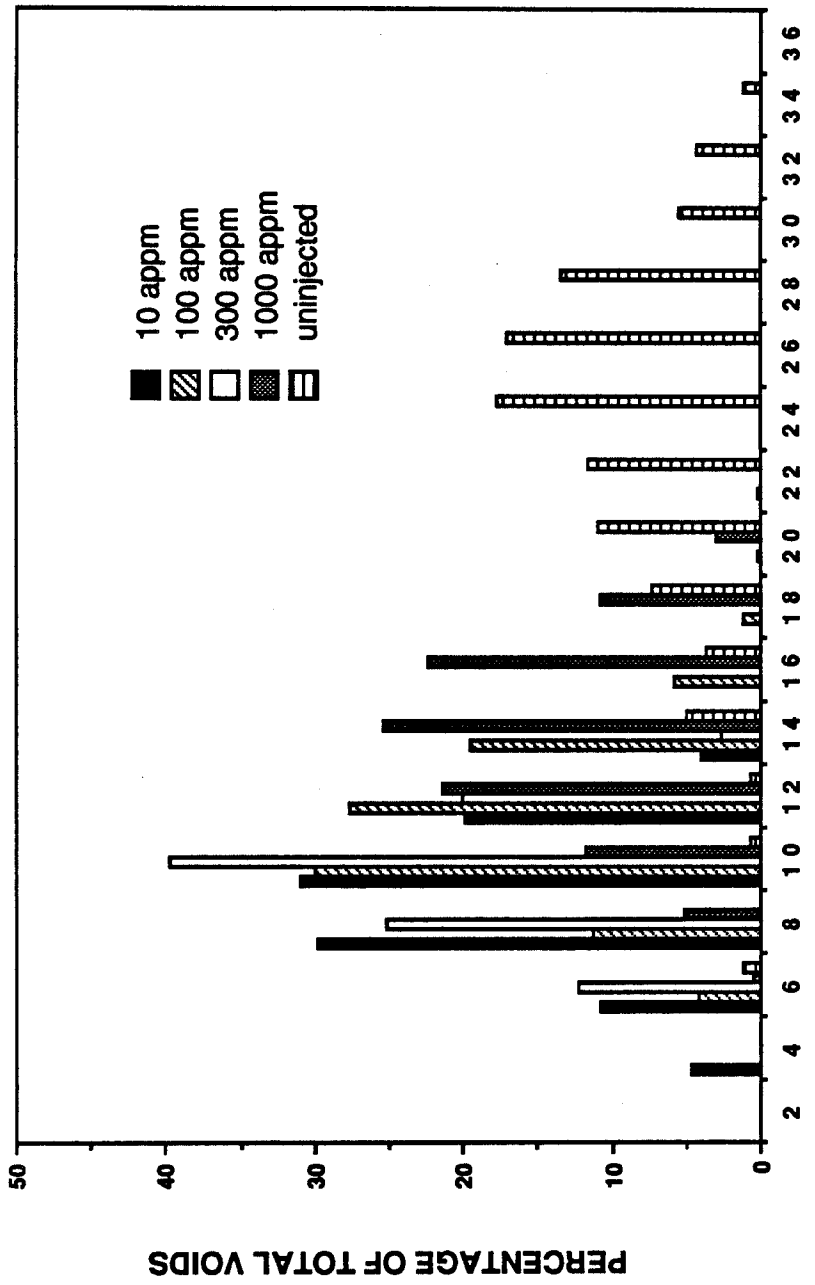

Figure 6.6. Void size distribution in Ni-irradiated Fe-17Ni-13Cr at 550 °C with varying levels of preimplanted oxygen. Total Ni fluence is 1.3 E16 ions/sq. cm.

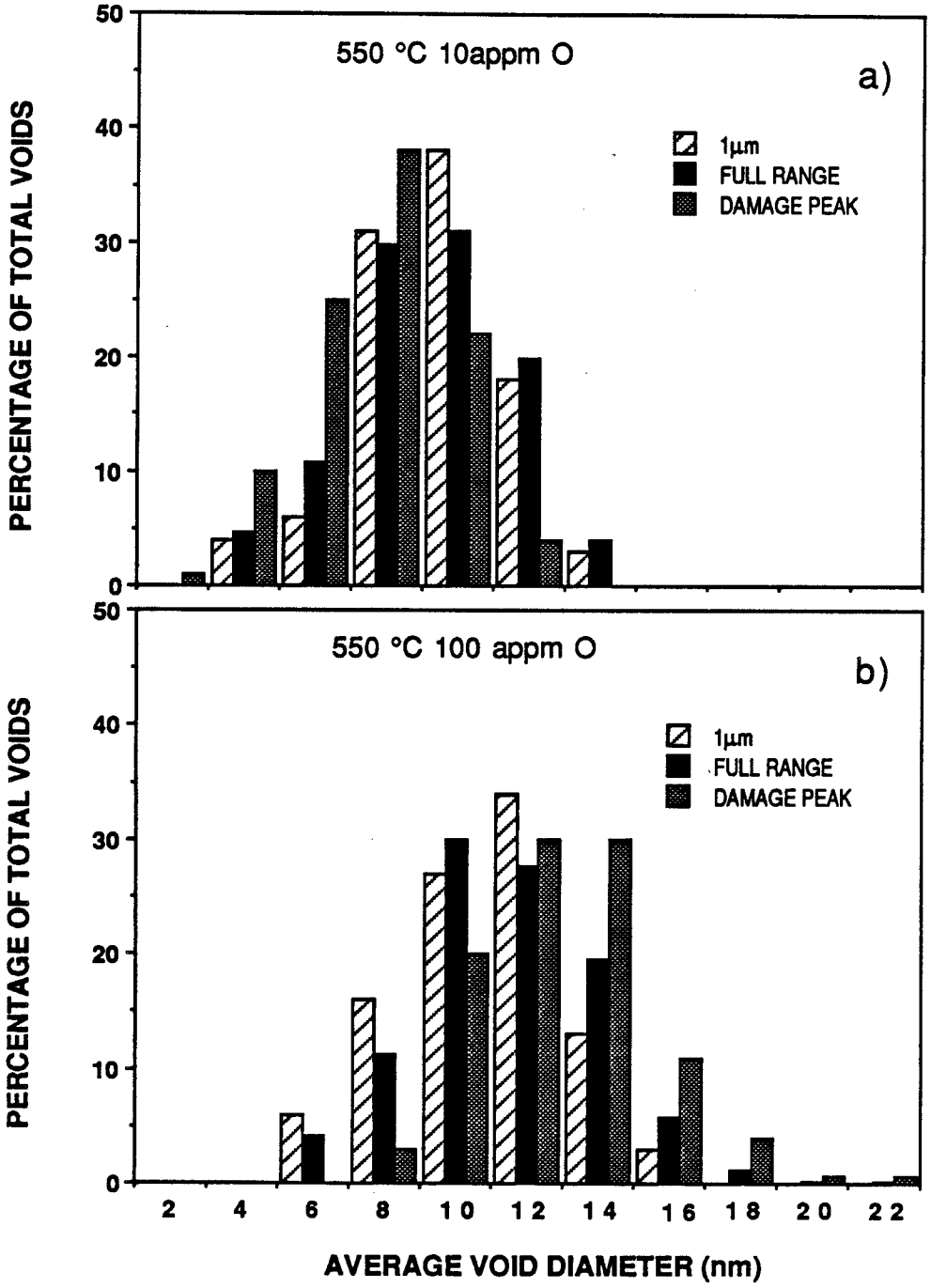

Figure 6.7. Void size distribution in Ni-irradiated Fe-17Ni-13Cr with a) 10 appm and b) 100 appm oxygen preimplanted. Total Ni fluence is 1.3 E16 ions/sq. cm.

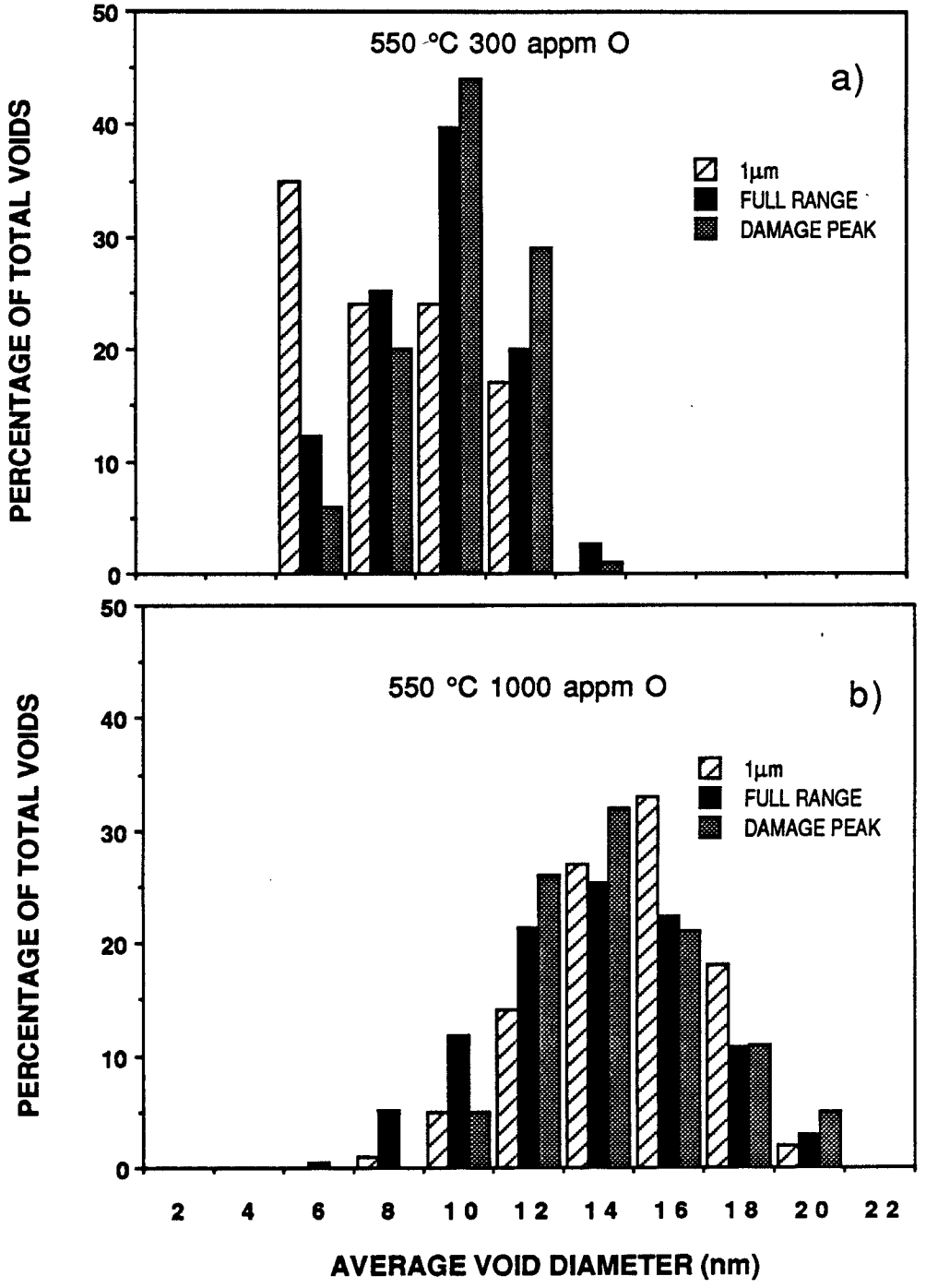

Figure 6.8. Void size distribution in Ni-irradiated Fe-17Ni-13Cr with a) 300 appm and b) 1000 appm oxygen preimplanted. Total Ni fluence is 1.3 E16 ions/sq. cm.

average diameter. Furthermore, Figures 6.7 and 6.8 reveal that the data taken over the full range is generally mirrored by the data taken at 1 μm and at 2 μm for the oxygen injected samples. The data at the 1 and 2 μm depths are taken from regions 0.25 μm wide in Figure 6.7 and 6.8. Only the 300 appm O injected sample shows a difference between the data taken at the 1 μm region and that taken over the full range. The data taken at 1 μm shows an average void diameter slightly smaller than that of the overall data. However, this sample has poor thin area and, subsequently, low counting statistics. The error bars on this data are about twice that of the other samples. Figures 6.6 to 6.8 also show the general trend of increased void diameter with increasing oxygen level for the preimplanted specimens.

The void densities of the 550°C irradiated samples are presented in Figure 6.9. The uninjected sample has a moderately peaked distribution of voids with maximum number density of $7\pm2\times10^{20}/m^3$ occurring at a depth of 1.5 μm. Preinjecting 10 appm of oxygen results in a very sharply peaked void distribution with a maximum number density of $27\pm4\times10^{20}/m^3$ at 1.5 μm. The steepness of the distribution decreases slightly when the oxygen preinjection concentration is increased to 100 appm. The peak void density drops a little to $23\pm4\times10^{20}/m^3$. At the 300 appm O injection level, the void density shows a minimum at a depth of 1.5 μm. In fact, there is a slight depleted zone between 1.50 μm and 1.63 μm. No voids are visible in this narrow range. This void depleted zone widens at the

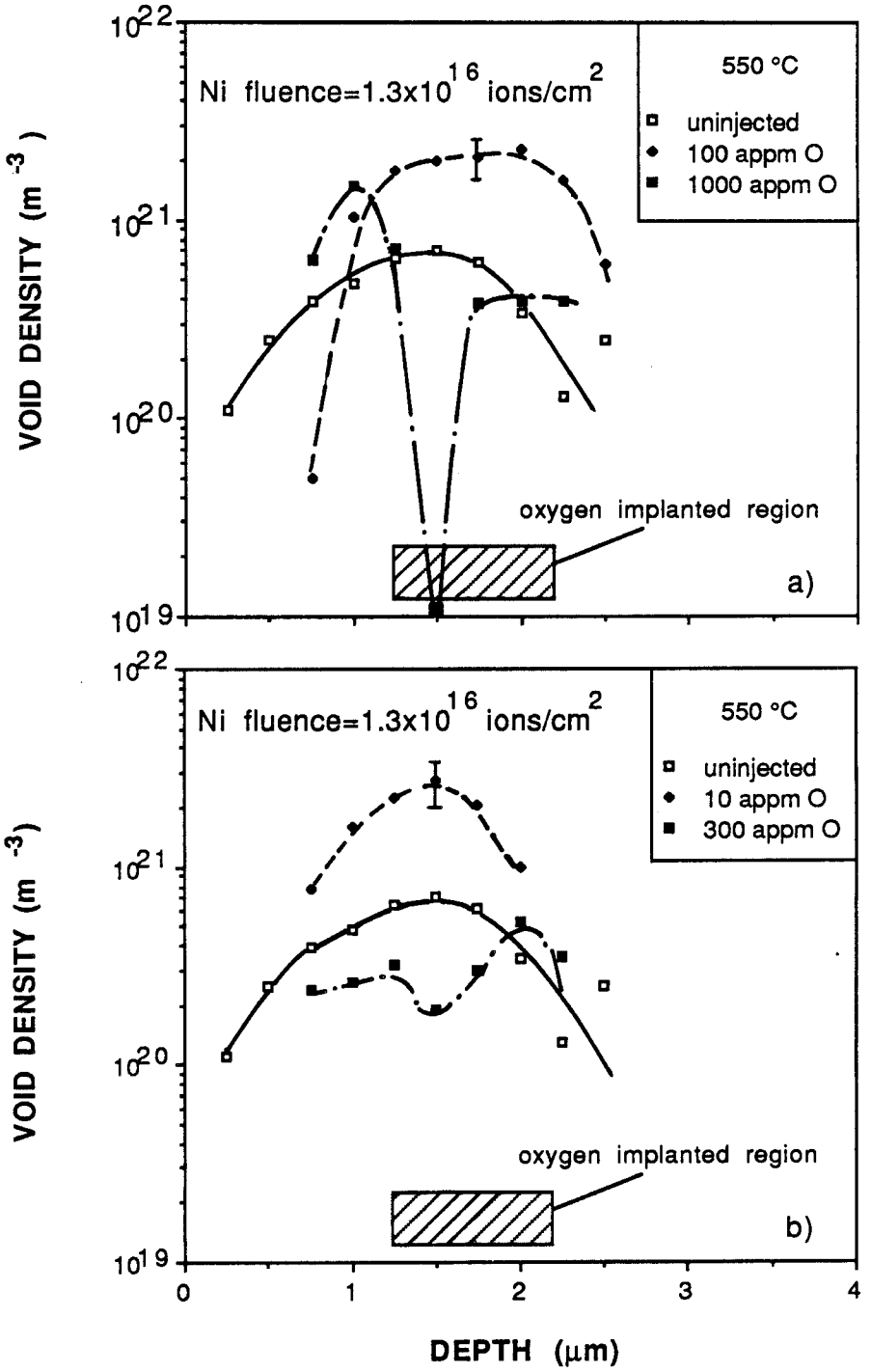

Figure 6.9. Void number density as a function of depth and oxygen concentration at 550 °C in Ni-irradiated Fe-17Ni-13Cr.

1000 appm O implanted level from 1.25 μm to 1.60 μm. This last sample also has a relatively high void density at 1 μm compared to the 300 appm injected sample.

B.2. Swelling Response Versus Temperature

Figure 6.10 shows a comparison of void diameter and density at different temperatures using high magnification micrographs. Figure 6.10a is a comparison of void response at 550, 600, and 650°C for the uninjected specimens. All these micrographs are taken from the 2 μm region. There does not seem to be a great difference in void diameter for these samples. The void density appears slightly greater in the 600°C case compared to 550 or 650°C. Figure 6.10b compares the results of the 100 appm O preimplanted specimens. A distinct difference in void size is visible between the 550°C and the 600 and 650°C cases. Void densities appear roughly the same in all cases. Note that the micrographs in Figure 6.10b are enlargements of the 1.5 μm region.

The effect of temperature on void diameter is presented in Figure 6.11. For the uninjected case (Figure 6.11a), there is not much change, within experimental error, of the void diameter on increasing the temperature from 550 to 600°C. When the temperature reaches 650°C the void diameter may decrease slightly. In general, however, at any particular depth all the diameters are the same, within experimental error. The tendency of the diameter to increase with increasing depth (and dose) for the uninjected 550°C sample is

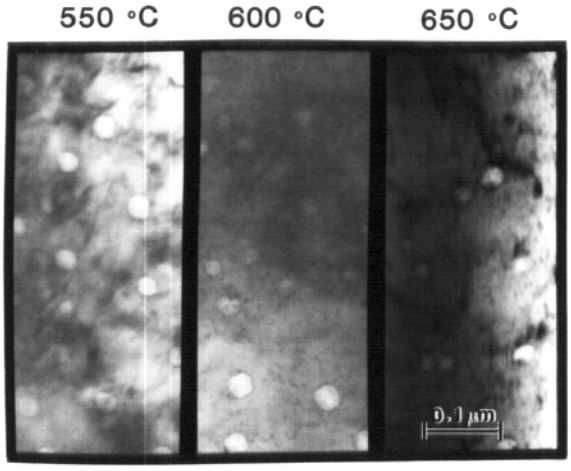

a) no injected oxygen

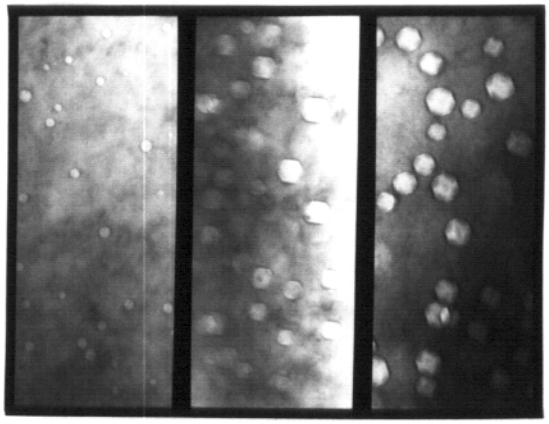

b) 100 appm injected oxygen

Figure 6.10. Comparison of the swelling response versus temperature for 15MeV Ni-irradiated Fe-17Ni-13Cr to a fluence of 1.3 E16 ions/sq. cm. a) with and b) without injected oxygen. Data taken at peak damage depth (2 μm and 15 dpa).

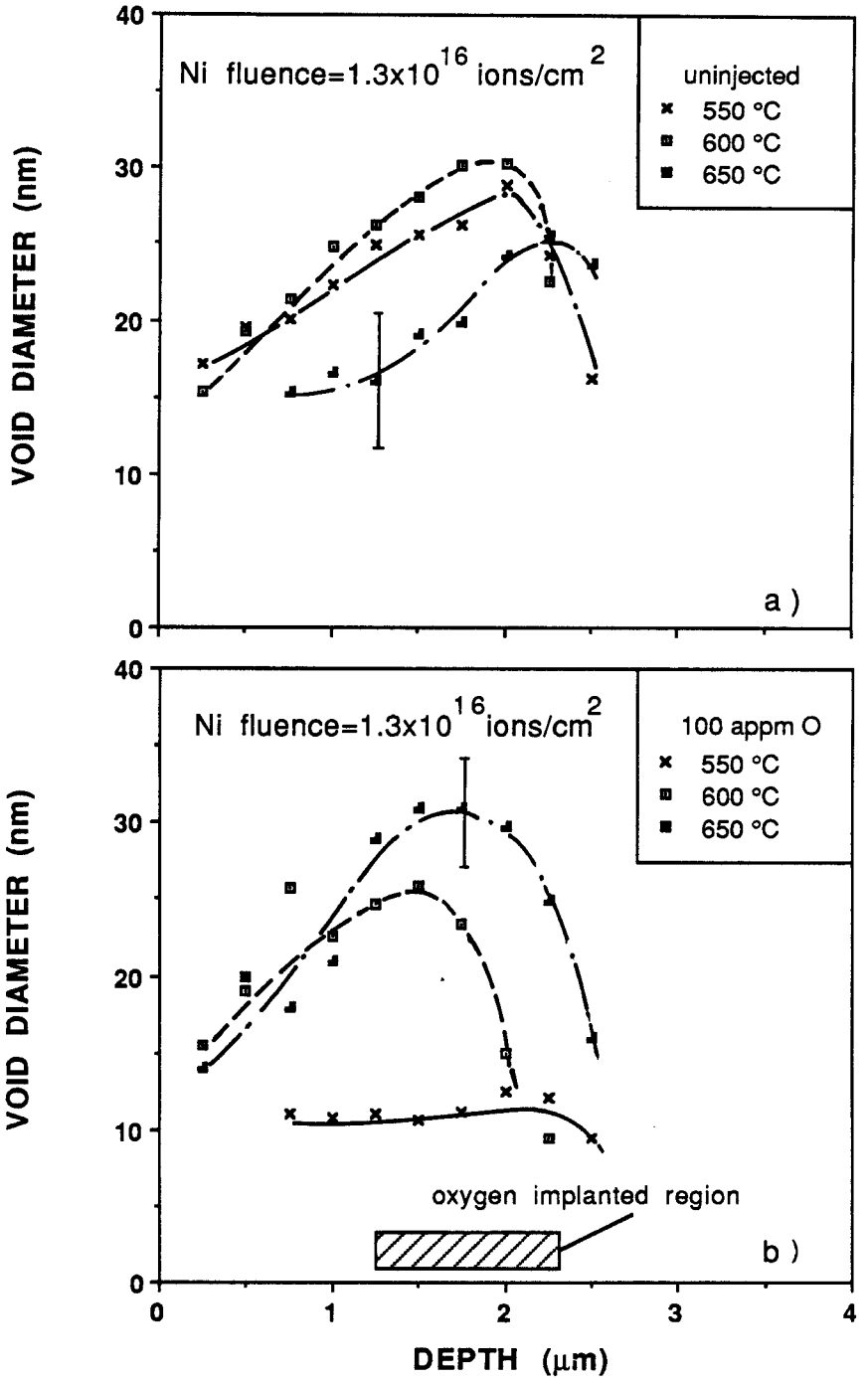

Figure 6.11. Void diameter as a function of depth and temperature in Ni-irradiated Fe-17Ni-13Cr. a) as treated. b) 100 appm oxygen preimplanted.

observed in the uninjected samples irradiated at 600 and 650°C. In all cases the maximum void diameter occurs around 2 to 2.25 μm.

When 100 appm O is injected into the alloy, the trends in diameter versus depth and diameter versus temperature are different from those of the uninjected samples. As Figure 6.11b demonstrates, there is a large increase in average void diameter for all depths, except the end of range, as the ion-irradiation temperature increases from 500 to 600°C. Another small increase in average void diameter occurs when the irradiation temperature is raised to 650°C. Also, although the diameter distribution versus depth remains relatively constant at 550°C, the 600 and 650°C irradiations have strongly peaked depth profiles of void diameter. In both cases the maximum void diameter occurs at a depth of 1.5 μm.

Another interesting trend in void diameter as a function of depth is revealed in Figure 6.12, where the void diameter is compared for the injected and uninjected cases at every temperature. At 550°C the diameter of the voids in the unimplanted sample is 2 to 3 times that of the voids in the specimen preimplanted with 100 appm O. At 600°C the void diameters in the implanted and unimplanted conditions are nearly the same up to 1.5 μm. After that the implanted specimen contains smaller voids. Finally, at 650°C the situation is opposite that at 550°C, so that the 100 appm O injected sample now has larger voids throughout most of the damage range than the unimplanted specimen. In this latter case, the void diameter of the oxygen injected specimen is about 1.5 times that of the uninjected case.

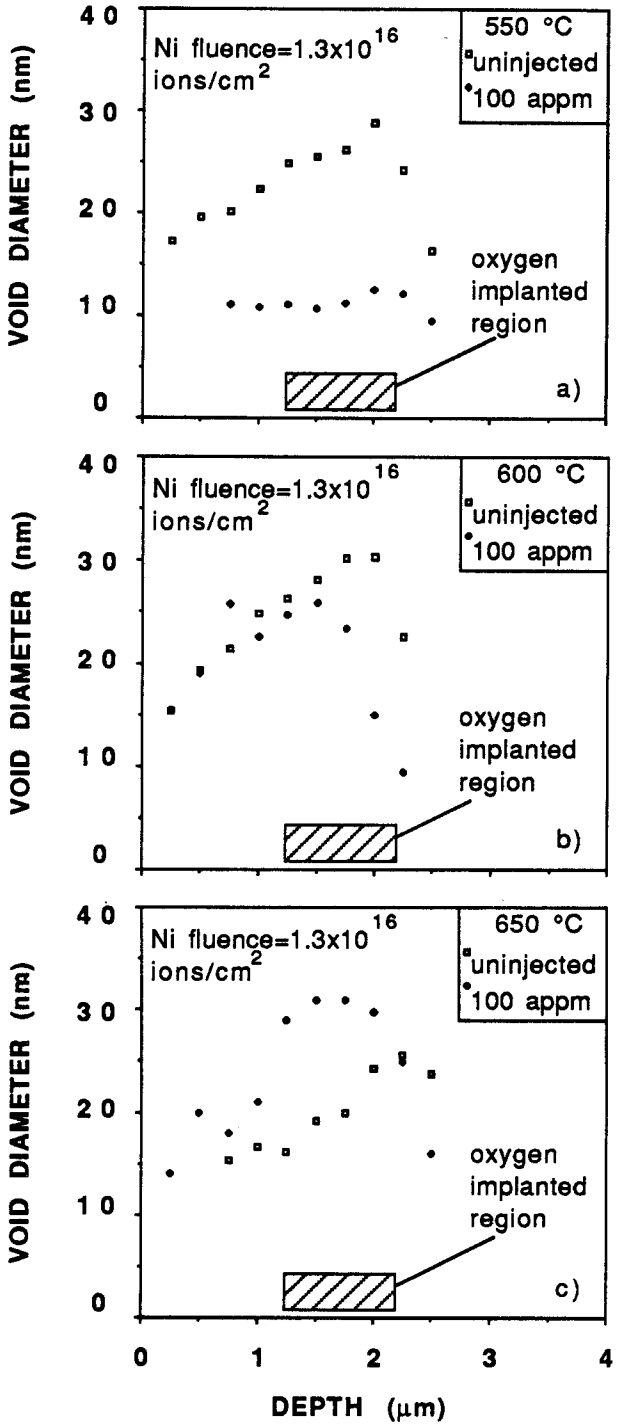

Figure 6.12. Comparison of void diameter with and without oxygen preimplantation at a) 550 °C, b) 600 °C, and c) 650 °C in Ni-irradiated Fe-17Ni-13Cr.

The trend towards increasing void diameter with increasing temperature in the 100 appm injected oxygen samples is also seen in Figure 6.13. Also evident in these histograms is the broader range of the void size distribution. Unlike the data for the 550°C oxygen injected samples, the void size distribution is not as tightly bunched in the 600 and 650°C injected samples. Whereas 60 to 80% of the data fell within 2 nm of the average diameter for the 550°C case, 60 to 80% of the void diameter data occurs within a range of about 6 nm from the average value for the higher temperature irradiations. This is due primarily to the fact that the void diameter is not uniform with depth. When averaging data over the full range, one expects greater variation in data from a peaked distribution than a flat distribution.

The void number density as a function of temperature is considered next. Figure 6.14 is a plot of the void density versus depth for the uninjected sample, Figure 6.14a, and for the injected case, Figure 6.14b, at the various irradiation temperatures. In the as-treated condition, the void density increases from 550 to 600°C, then drops at 650°C. However, in all cases the density increases with damage level (or depth). Also the location of the maximum void number density varies from 1 μm at 600°C to 1.5 μm at 550°C to 2.25 μm at 650°C.

With 100 appm O injected, the temperature effect on void density is more consistent. At 550°C the maximum void density of $23\pm4\times10^{20}/m^3$ occurs at 2 μm. At 600°C the maximum void density is

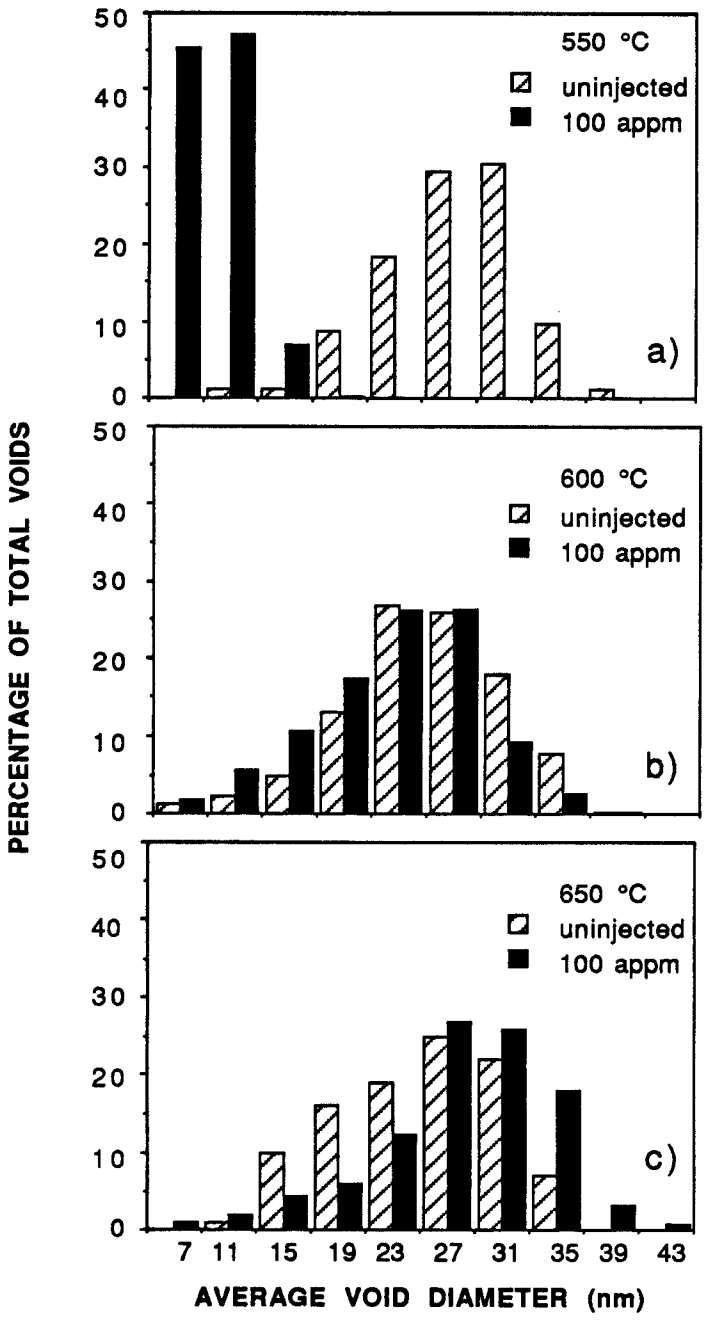

Figure 6.13. Comparison of the void size distribution in Ni-irradiated Fe-17Ni-13Cr at a) 550 °C, b) 600 °C, and c) 650 °C with and without oxygen preimplantation. Ni fluence is 1.3 E16 ions/sq. cm.

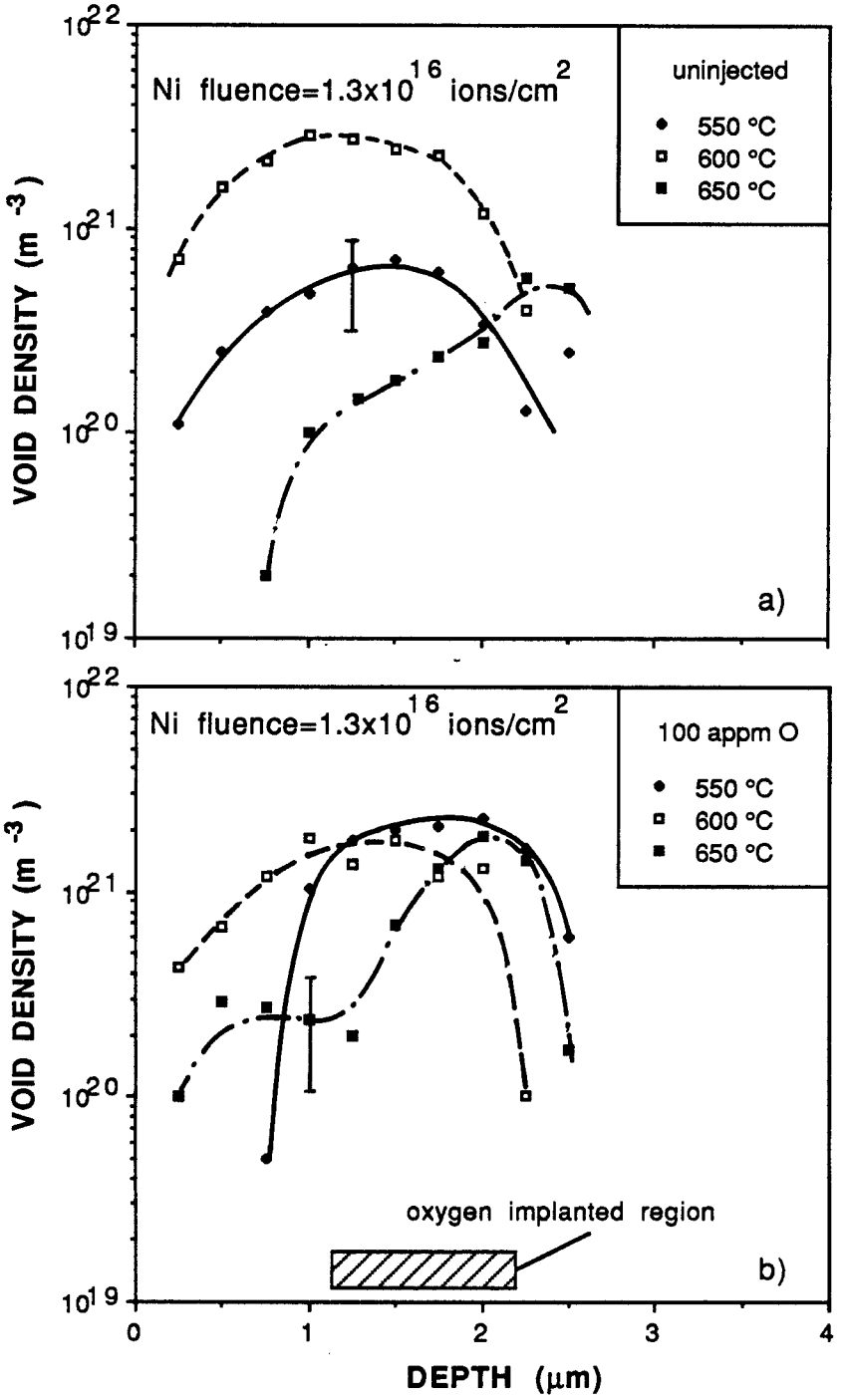

Figure 6.14. Void number density as a function of depth and temperature in Ni-irradiated Fe-17Ni-13Cr. a) as treated. b) 100 appm oxygen preimplanted.

found at 1.25 μm and has a value of $24\pm3\times10^{20}/m^3$. In the 100 appm O injected specimen irradiated at 650°C, the peak density of $19\pm2\times10^{20}/m^3$ occurs at 2 μm. Note that the void density distribution varies more as a function of depth with increasing temperature.

A comparison of void density in samples with and without oxygen injection at the different irradiation temperatures is given in Figure 6.15. At 550°C the void density in the 100 appm O injected sample is greater than that in the unimplanted sample. There is also a slight shift in density distribution to greater depths with oxygen implantation. Within experimental error, there does not seem to be any difference between the two cases at 600°C. At 650°C, the oxygen injected specimen again has a greater void density than the unimplanted case. Also, the 650°C irradiated sample shows a low void density from 0 to 1 μm followed by an increase in void density up to 2 to 2.25 μm.

B.3. Surface and End-of-Range Effects

Finally, the data is reviewed with regard to the swelling response at the front surface of the sample and at the end of range. Table 6.3 gives the depth at which voids are first seen and at which they are last observed in all the irradiated specimens. Notice that at 550°C, all the oxygen preimplanted specimens show a void-free region within 0.5 to 0.7 μm of the surface. All other specimens, with the exception of the uninjected 650°C sample, show little or no void-free zone at the irradiated surface. It should be

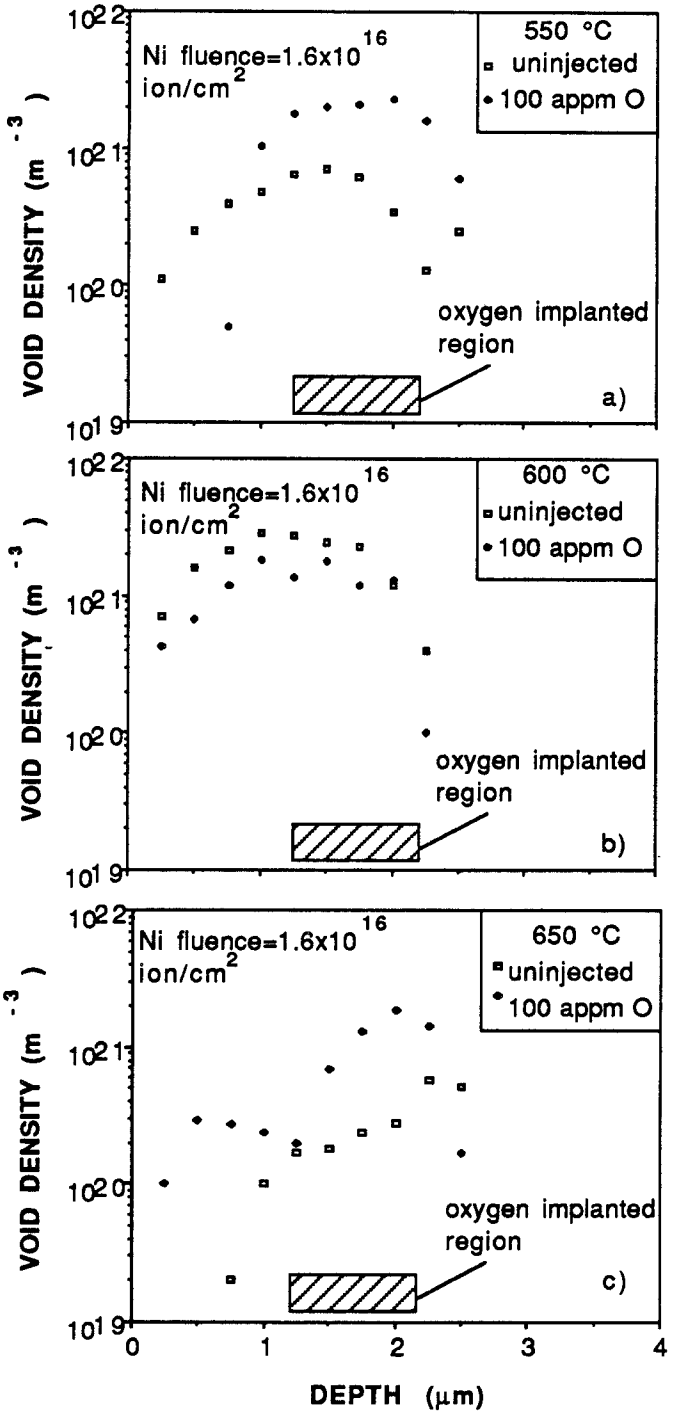

Figure 6.15. Comparison of void number density with and without oxygen preimplantation at a) 550 °C, b) 600 °C, and c) 650 °C in Ni-irradiated Fe-17Ni-13Cr.

Table 6.3. Damage Range Data in 15 MeV Nickel-Irradiated Fe-17Ni-13Cr to a Fluence of 1.3×10^{16} ions/cm^2(a)

Temperature (°C)	Injected Oxygen (appm)	Depth of Initial Voidage (μm)	Depth of Final Voidage (μm)	Width of Void Region (μm)
550	0	0.2	2.5	2.3
	10	0.5	2.0	1.5
	100	0.7(b)	2.5	1.8
	300	0.6	2.25	1.7
	1000	0.5	2.25	1.8
600	0	Interface	2.25	2.3
	100	Interface	2.25	2.3
650	0(c)	0.5	2.5	2.0
	100	~ 0.1	2.5	2.4

(a) 1.3×10^{16} ions/cm^2 is 5 dpa at a depth of 1 μm.

(b) Adjusted depth for 45° cross-section.

(c) Irradiated with 14 MeV Nickel.

noted that the 650°C unimplanted specimen was irradiated with 14 MeV Ni^{3+} ions unlike all the other samples, which received 15 MeV Ni-ion irradiation. However, a decrease in ion energy results in a slight decrease rather than increase in the total range of the damage. Calculations on the dose versus depth for 14 MeV Ni ions, however, show no noticeable difference in damage in the first 1 μm compared with the damage for 15 MeV Ni ions (Figure 2.1).

The data in Table 6.3 also shows that the total range of voids can be broken into the same categories. At 550°C the oxygen injected samples have a width of the region where voids are first and last seen varying from 1.5 to 1.8 μm. All other data, again with the exception of the 650°C uninjected case, have a width of 2.3 to 2.4 μm where voids are seen. The aforementioned 650° sample has a width of only 2.0 μm.

The depth at which the swelling ceases appears to vary from sample to sample without a pattern. This lack of consistency may be due to a variation from sample to sample in the amount of material removed from the surface during the post-irradiation specimen handling. The striking step in the electroplating procedure is estimated to uniformly remove ~ 0.2 μm from the irradiated surface. One sample, the 10 appm O injected specimen irradiated at 550°C, was subjected to a striking time twice normal during post-irradiation electroplating. Prior to electroplating an 0.3 μm alumina slurry is used during a light mechanical cleaning of the surface. The amount of material removed from the surface by this latter step varies from

sample to sample, typically from 0 to 0.5 μm. Therefore, some of the inconsistencies may be eliminated by assuming that the end of range of the damage corresponds to the depth at which the swelling ends. Although this is not necessarily true, it is likely that the depth at which swelling stops should be nearly the same in all cases, because significant damage occurs beyond the end of the oxygen implanted zone.

Figure 2.1a indicates that the end of range of the damage is calculated to be 2.7 μm for the 15 MeV (and 14 MeV) nickel-irradiated alloy. Table 6.4 is a compilation of key data assuming that the true depth at which the voidage ends is 2.7 μm. Nearly all of the inconsistencies in the data are eliminated by matching the end of the swelling regimes in all the samples. For example, the depth at which the maximum void density or, in some cases, the void-depleted zone occurs is 1.95 to 2.2 μm in all the oxygen injected samples. This corresponds very well to the calculated depth, given in Figure 2.1b, of the oxygen implanted region. Figure 2.1b shows the full width at half maximum (fwhm) of the oxygen implanted zone occurs from 1.8 to 2.0 μm, with the full oxygen distribution taking place from 1.2 to 2.2 μm. Only the samples not preinjected with oxygen show any variation in the location of the peak void density.

Another discrepancy that is resolved by adjusting the data to a unified end of range is the location of the maximum void diameter. Before adjustment, the depth at which the void diameter peaked varied from sample to sample with little consistency. Table 6.4 shows that,

Table 6.4. Adjusted Swelling Response in Nickel-Irradiated Fe-17Ni-13Cr Alloy

Irradiation Condition		Adjusted[a]	Surface[b]	Depth of[b]	Depth of[b]	
Oxygen Implantation (appm)	Irradiation Temperature (°C)	Depth (μm)	Denuded Zone Width (μm)	Maximum or Suppressed Void Density (μm)	Maximum Average Void Diameter (μm)	Width of Void Bearing Zone (μm)
0	550	0.2	0.4	1.7	2.2	2.3
	600	0.45	≤0.45	1.45	2.45	≥2.3
	650	0.2	0.7	2.45	2.45	2.0
100	550	0.2	0.9	2.2	2.2	1.8
	600	0.45	≤0.45	1.95	1.95	≥2.3
	650	0.2	0.3	2.2	2.2	2.4
10	550	0.7	1.2	2.2	2.45	1.5
100		0.2	0.9	2.2	2.2	1.8
300		0.45	1.05	1.95[c]	2.3	1.7
1000		0.45	0.95	1.95[c]	2.45	1.8

a) Depth added to cause end of void bearing zone to correspond to 2.7 μm.
b) Value resulting from adding adjusted depth to raw data.
c) Depth at which void denuded zone appears within the void bearing region.

after the depth correction is made, the maximum void diameter occurs consistently around 2.2 μm. Reference to Figure 2.1a reveals that the peak damage is calculated to occur around 2.1 μm.

Adjustment of the data also reveals some trends in the void-denuded zone at the front surface. When no oxygen is injected, the width of this denuded zone increases slightly with increasing temperature. At an irradiation temperature of 650°C, the maximum denuded zone width of 0.7 μm occurs. Sindelar [3] also found a void-denuded zone, 0.6 μm wide, in P7 irradiated to a fluence of 3.3×10^{16} ions/cm^2 at 650°C with 14 MeV Ni. His data also shows a denuded zone in the first 0.4 μm at 550°C and a fluence of 1×10^{16} ions/cm^2. Garner and Thomas [4] observed a 0.6 μm denuded zone at the front surface of 1 MeV electron-bombarded 316 SS irradiated at 650°C.

When 100 appm of oxygen is preimplanted, the irradiated specimens show a strong temperature dependence on the extent of the surface void-denuded zone. The width of the zone decreases from a maximum of 0.9 μm at 550°C to a minimum of 0.2 μm at 650°C. At 550°C, in fact, the width of the denuded zone appears to be relatively independent of the level of oxygen implanted. All the preimplanted specimens irradiated at 550°C have a surface void-denuded zone 0.9 to 1.2 μm wide. Only the unimplanted 550°C specimen has a smaller denuded region, 0.4 μm.

The assumption that the depth where void formation stops corresponds to the end of the calculated range may not be correct. This assumption is composed of two parts. First it is assumed that

the void swelling region should cease at the same depth in all the samples irradiated. It then assumes that end of the swelling region corresponds to the end of range. When both assumptions are made, the data not only becomes self-consistent but also tends to support other aspects of the model used in Chapter 2 to calculate oxygen range and ion damage versus depth. This certainly strengthens arguments for the validity of both assumptions. However, the key assumption needed to eliminate most discrepancies in the data is the first assumption, that the depth at which the voids end in all the irradiated samples should be the same. As stated earlier, the reason that they do not appear to be is due to variations in the amount of surface removed during post-irradiation sample preparation, 0.2 to 0.9 μm. The impact and validity of both the first and second assumptions, as well as the inferences to be drawn from these experiments are discussed in the next chapter.

References for Chapter 6

1. E.E. Underwood, "Applications of Quantitative Metallography," in Metals Handbook Eighth Edition, Vol 8, ASM (1973) 37-47.
2. P. Hirsch, A. Howie, R.B. Nicholson, D.W. Pashley, and M.J. Wheland, Electron Microscopy of Thin Crystals, Second Edition, Robert E. Krieger Publishing Co., Huntington, NY (1977) 422-424.
3. R.L. Sindelar, "A Comparison of the Response of 316 SS and the P7 Alloy to Heavy-Ion Irradiation," Ph.D. Thesis, University of Wisconsin-Madison (1985).

4. F.A. Garner and L.E. Thomas, "Production of Voids in Stainless Steel by High-Voltage Electrons," in Effects of Radiation on Substructure and Mechanical Properties of Metals and Alloys, ASTM STP 529 (1973) 303-325.

CHAPTER 7

DISCUSSION

A. Oxygen Effects on the Swelling Response

A.1. Void Number Density Trends

The variation in void density with temperature in the uninjected specimens shows an increase in density from 550 to 600°C followed by a decrease at 650°C, as shown in Fig. 6.14a. This trend becomes less pronounced closer to the damage peak. At a depth of 0.75 μm the void density varies by two orders of magnitude between 600 and 650°C.

The review of previous particle irradiation studies, summarized in Tables 4.1 and 4.2, shows that void density generally decreases with increasing temperature. However, several studies (ref. 41,43, 48,53,69,74,76 in Chapter 4) report void density behavior similar to that reported here for the unimplanted case. Farrell and Packan [1] report a slight increase in void density from $6.6 \times 10^{20}/m^3$ at 575°C to $9 \times 10^{20}/m^3$ at 625°C in a 4 MeV Ni-irradiated, 10 dpa Fe-17Cr-17Ni-2.5Mo alloy. At 675°C the void density drops an order of magnitude to $1.8 \times 10^{19}/m^3$.

According to theory, void nucleation rates and void densities should decrease with increasing irradiation temperature, as depicted in Figure 2.3. This prediction is common to all the void nucleation theories reviewed. Therefore, an increase in the observed void density must be attributed to stabilization of the void against collapse. Assuming that the majority of residual oxygen in the alloy

is bound at internal oxides and surfaces, e.g. grain boundaries, little gas remains to stabilize the voids. At low temperature, then, only a small fraction of the high terminal void density can be stabilized by oxygen. As the temperature increases, the thermal jump frequency [2] and the oxygen diffusivity [3] increase. Therefore, a higher probability exists for an oxygen atom to detrap and diffuse to and stabilize a void embryo. This probability increases with increasing temperature; however, the terminal void density decreases rapidly with increasing temperature. The void density data indicate that these competing mechanisms optimize around 600°C in this alloy.

Figure 6.14b shows that when oxygen is injected into the alloy prior to irradiation, the void density variations with temperature diminish, especially in the implanted region. The peak void density recorded at all temperatures in the 100 appm O injected specimens is about $1.5 \times 10^{21}/m^3$. However, when the temperature is fixed at 550°C and the preimplanted oxygen concentration is varied from 0 to 1000 appm, the peak void density varies significantly (see Fig. 6.9). These results indicates that the level of oxygen injected has a greater influence on void density than does temperature over the range 550 to 650°C. However, it is difficult to correlate precisely oxygen level to void density, because void growth and coaelescence alter the final void density.

A.2. Void Diameter Trends

Several points emerge when the void diameter trends as a function of oxygen level and temperature are considered. First, when the alloy is irradiated in the as-treated condition the average void diameter is nearly independent of temperature. Figure 6.11a indicates that the change in void diameter versus depth is the same at all temperatures. The sample irradiated at 650°C appears to have a slightly smaller average diameter than the other samples. Within the experimental error, however, the diameter at 550, 600, and 650°C at any given depth is the same. Review of Tables 4.1 and 4.2 shows that void diameter generally increases with temperature. However, the accumulated dose in this study, 5 dpa at a depth of 1 μm, is lower than most other studies. This is early in the void growth regime. Although temperature has an effect on void density during the nucleation period, it has little effect on void embryo size [4]. Once nucleation is completed, void growth and coalescence occur and temperature has a strong effect [5]. Because void growth is still relatively nascent at 5 dpa, not much difference exists in the reported void diameters in the uninjected specimens.

When oxygen is implanted before ion irradiation the situation changes with respect to void diameter versus temperature. Figure 6.11b reveals that the void diameter increases as a function of temperature when 100 appm oxygen is preinjected. Furthermore, Figure 6.5 shows that the void diameter remains unaltered regardless of the concentration of implanted oxygen at a single temperature.

These results indicate the voids nucleate almost immediately when oxygen is preimplanted. Thus nucleation terminates very early in the irradiation and void growth occurs during the majority of the irradiation. Thus void size becomes a function of temperature only in the oxygen preinjected specimens.

These results combined with the void density results indicate the strong effect free oxygen has on the response of the irradiated alloy. Further evidence for the direct role that oxygen plays are discussed in the next section.

B. VOID SUPPRESSION

B.1. Near-Surface Void Free Zone

Evaluation of the width of the void denuded regions at the surfaces of the irradiated specimens yields contradictory trends. For the specimens without oxygen preimplantation, the width of the zone increases with temperature. The opposite is true for the oxygen preimplanted samples. The reasons for this are discussed below.

Garner and Thomas [6] noted that a void free zone occurs at the surface of electron-irradiated 316 SS. They found that the average width of the surface void denuded zone, L_{vf}, depended on the vacancy diffusivity, D_v, and the displacement rate, P, according to

$$L_{vf} \sim \left(\frac{D_v}{P}\right)^{1/2} . \qquad (7.1)$$

According to Badger, et al. [2], the vacancy diffusivity in Fe-Ni-Cr

alloys with a composition near that of type 316 SS can be calculated by

$$D_v = \sum_x C_x a_o \left(\frac{\bar{E}_v^m}{M}\right)^{1/2} \exp\left(\frac{S_v^m(x)}{k}\right) \exp\left(\frac{-E_v^m(x)}{kT}\right) \qquad (7.2)$$

where C_x is the atomic fraction of element x, a_o is the lattice parameter, $\bar{E}_v^m$ is the average vacancy migration energy, M is the mass of the diffusing atom, $S_v^m(x)$ is the vacancy migration entropy of element x, $E_v^m(x)$ is the vacancy migration energy of element x, and kT is Boltzmann's constant times absolute temperature. The average vacancy migration energy is given by $\bar{E}_v^m = \sum_x C_x E_v^m(x)$.

Evaluation of equation (7.2) using the data in B. Badger and co-workers [2] for steel, the vacancy diffusivity is found to be $D_V = 0.19\ \mu m^2/sec$ at 550°C, $D_v = 0.59\ \mu m^2/sec$ at 600°C, and $D_v = 1.6\ \mu m^2/sec$ at 650°C. The vacancy migration energy used to determine these diffusivities is $\bar{E}_v^m = 1.37$ eV. Using these diffusivities and the displacement rates given in Table 6.1, the width of the near-surface void free zone, L_{vf}, can be calculated. A comparison of the measured L_{vf} and the calculated L_{vf} is given in Table 7.1.

For the uninjected samples the width of the measured void free zone, L_{vf}^{meas}, increases with increasing temperature. This trend is paralleled by the increase in the calculated width of the void free zone, L_{vf}^{calc}. There is a two order of magnitude disagreement concerning the value of L_{vf}^{meas} and L_{vf}^{calc}, but the trends are similar. This agreement indicates that the increase in vacancy diffusivity

Table 7.1. Comparison of Near-Surface Void Free Zone in Nickel-Irradiated Fe-17Ni-13Cr Using Vacancy Diffusivity Model

Without Injected Oxygen

Temp (°C)	D_v^{calc} ($\mu m^2/s$)	P ($10^{-4}/s$)	L_{vf}^{calc} (μm)	L_{vf}^{meas} (μm)	$L_{VF}^{calc}/L_{VF}^{meas}$
550	0.19	7	16	0.4	40
600	0.59	12	22	0.45	49
650	1.6	7	48	0.7	69

With Injected Oxygen

Temp (°C)	Injected Oxygen Level (appm)	D_v^{calc} ($\mu m^2/s$)	P ($10^{-4}/s$)	L_{vf}^{calc} (μm)	L_{vf}^{meas} (μm)	$L_{vf}^{calc}/L_{vf}^{meas}$
550	10	0.19	8.2	15	1.2	13
	100	0.19	8.8	15	0.9	17
	300	0.19	7.0	16	1.05	15
	1000	0.19	13.4	12	0.95	13
600	100	0.59	12	22	0.45	49
650	100	1.6	6	52	0.3	173

with rising temperature may be responsible for the widening extent of the void denuded zone near the surface. The influence of the surface as a point defect sink increases to greater depth as the mobilities of the point defects increase. This explanation, offered by Garner and Thomas, applies for the irradiated specimens that do not receive a preimplantation of oxygen.

This is in contrast to the case for the oxygen implanted specimens. Not only is there a difference in the value of L_{vf}^{meas} and L_{vf}^{calc} of one to two orders of magnitude, but there is also a complete disagreement in the trends with varying temperature. The calculated value of L_{vf} increases with increasing temperature whereas the measured values decrease with increasing temperature. This trend for the measured value of L_{vf} is true for both the unadjusted and adjusted swelling data. The observed decrease in the near surface void denuded zone cannot be explained by a variation in vacancy diffusivity.

One possible explanation for the decreasing void free zone width with increasing temperature in the oxygen injected specimens is that the implanted oxygen is unbound and, therefore, free to diffuse towards the surface. As the temperature increases the oxygen diffusivity increases. This allows the oxygen to diffuse a greater distance toward the surface in a given time and the observed void free zone will be smaller. The validity of this argument can be estimated as follows.

The injected oxygen is distributed over the range 1.2 to 2.2 μm, as shown in Figure 2.1b. Because all the implantations are carried out at room temperature, the oxygen distribution should be identical in all the preimplanted samples. Defining the minimum depth at which the oxygen comes to rest as L_o^{min}, the width of the void denuded zone at the surface, L_{vf}, can be estimated as

$$L_{vf} = L_o^{min} - \sqrt{Dt} \tag{7.3}$$

where D is the oxygen diffusion coefficient and t is the time required for the stable vacancy cluster population to form. The oxygen diffusion coefficient may be roughly estimated using the diffusion data of oxygen in γ-Fe [3],

$$D = 5.75 \exp\left(\frac{-40,300}{1.98T}\right) \text{ cm}^2/\text{sec} . \tag{7.4}$$

This diffusivity is valid only over a temperature range of 950 to 1350°C. However, the qualitative trends of oxygen diffusion in type 316 SS at lower temperatures may be evaluated using this expression.

Table 7.2 contains a comparison of the measured and predicted void free zone widths, L_{vf}, using equation (7.3). Good agreement is found between the L_{vf}^{meas} and L_{vf}^{calc} in all oxygen implanted cases for a cluster formation time of 6 seconds, which is an accumulated dose of about 0.005 dpa. Wehner and Wolfer [4] calculate that after 6 seconds of irradiation at $1x10^{-3}$ dpa/s the number density of void

Table 7.2. Comparison of Near-Surface Void Free Zone in Nickel-Irradiated Fe-17Ni-13Cr Using Oxygen Diffusion Model

Temp (°C)	Implanted Oxygen (appm)	L_o^{min} (μm)	D ($\mu m^2/s$)	L_{vf}^{calc} (μm)	L_{vf}^{meas} (μm)	$L_{vf}^{calc}/L_{vf}^{meas}$
550	10	1.2	.0126	.9	1.2	0.75
	100	1.2	.0126	.9	.9	1.0
	300	1.2	.0126	.9	1.05	0.86
	1000	1.2	.0126	.9	.95	0.95
600	100	1.2	.0513	0.6	.45	1.3
650	100	1.2	.1800	0.2	0.3	0.67

a) assume t_c=6 sec (dose ~ 0.005 dpa)

embryos containing 100 vacancies (r/b=2.5) is about $5x10^{21}/m^3$, as shown in Figure 2.2. Although this quantitative agreement is based on broad assumptions, such as the extension of diffusion data in γ-Fe at high temperature to austenitic steel at moderate temperature, the qualitative predictions should be sound and do agree well with the empirical results.

Equation (7.4) assumes that oxygen diffuses by a vacancy mechanism. Although the injected oxygen is initially located at interstitial sites, the binding energy of the oversized oxygen atom to a vacancy is probably quite large. Thus, the injected oxygen probably occupies a substitutional position as soon as irradiation begins. The fact that only six seconds is needed to obtain the required amount of diffusion indicates that the oxygen probably does diffuse substitutionally and interstitial diffusion need not be invoked. The experiments in this thesis do not address this issue.

The differences in the observations concerning the extent of the void free zone at the surface between the oxygen implanted and the unimplanted speciments strengthen the argument for the role of oxygen in void stability. As shown above, the oxygen implanted specimens contain oxygen that is free to diffuse. This unbound oxygen appears to migrate towards the specimen surface. It is also reasonable to expect it to migrate towards internal surfaces, such as grain boundaries or void embryos. Because in this study the average grain diameter is large (~ 20 μm) compared to the ion range (~ 2 μm), it is unlikely for a grain boundary to intersect the irradiated region.

Void embryos are formed immediately upon irradiation and are stabilized by these freely moving oxygen atoms. At higher temperatures the oxygen can diffuse faster and may, therefore, stabilize voids closer to the surface before the terminal void density is reached. Once the terminal void density is achieved, the voids grow and coalesce and nucleation of new voids becomes very unlikely.

In the uninjected specimens a different path to void stability is taken. In the as-treated material it is probable that the majority of residual oxygen (160 appm O) is bound to some degree to internal surfaces or to Fe and Cr complexes. The formation energy of an iron oxide or chromium oxide is much smaller than the free energy of oxygen in solution, as noted in Chapter 3. As the irradiation proceeds oxygen atoms become unbound by collision with energetic knock-ons or by thermal vibrations. The concentration of mobile oxygen atoms is much smaller than that of the oxygen injected case, even when only 10 appm oxygen is implanted. This is evident by the large difference in void density between the unimplanted and 10 appm O implanted specimens irradiated at 550°C (Figure 6.9b). As the irradiation proceeds in the unimplanted samples, a critical oxygen concentration is probably first accumulated at the damage peak, where the displacement rate is greatest. The voids nearest the damage peak are stabilized first and provide a sink for point defects as well as oxygen. Point defects are also being depleted at the specimen surface. The width of the void bearing zone continues to

widen as more oxygen becomes unbound until nucleation is terminated by the increasing void sink strength.

B.2. Void Suppression in the Oxygen Implanted Region

The effect of increasing oxygen concentration on the density of voids at 550°C points to the possibility that high gas contents may suppress swelling. Figure 6.9 shows that the visible void density initially increases with increasing oxygen implantation, then decreases at higher implanted oxygen levels. At 300 appm O and greater implantation concentrations, a region depleted of visible voids appears in the implanted region. The reduction of visible cavity density with increasing gas content has been previously reported for helium implantations in ion-irradiated nickel [7,8] and for ion irradiations in vanadium [10] with varying oxygen levels.

Bullen [7] reports the visible void density falls to zero in the helium implanted region in nickel preimplanted with 100 appm and 600 appm He at room temperature and subsequently irradiated with 14 MeV self-ions to a fluence of 1×10^{16} ions/cm^2 at 525 and 625°C. The helium in both samples is distributed over the first 1.25 μm by energy ramping between 200 and 700 kV. When the helium is mono-energetically preimplanted at room temperature and 700 kV to a depth of 1.0 to 1.25 μm in 14 MeV self-ion irradiated nickel at 525°C, the cavity density increases by an order of magnitude (~ 2×10^{23}/m^3) in the implanted zone and the mean cavity diameter is about 4.5 nm. Bullen, threfore, concludes that the apparent suppression of the void

density is due to the existence of a very high density of small cavities below the resolution of the microscope. This is one possible explanation for the apparent void density suppression in this study, as well. However, no voids were seen in the denuded zones at magnifications as high as 330,000 X.

Another explanation for the existence of a zone depleted of visible voids at high gas contents is that the gas atoms trap vacancies and, thereby, enchance recombination. It has been shown that helium is capable of trapping vacancies [9] as can oxygen [10]. Wechsler and Foster [11] have demonstrated that oxygen can be trapped at point defect clusters in vandium. This enhancement of the point defect recombination leads to the shift of the peak swelling toward higher temperatures when gas is implanted. It should be noted that helium is more effective at enhancing recombination than oxygen due to its greater binding energy to vacancies.

The decrease in observed void density with increasing gas content may also be explained in terms of an increase in sink density. The total number of point defects generated in every sample should be the same since the nickel ion fluence is the same. Therefore, the point defect partitioning depends on the density of sinks and the migration energy. For the specimens irradiated at 550°C the migration energy is the same for both control and implanted specimens. Therefore, the increasing sink density in the oxygen implanted zone is the only variable in these samples. With increasing oxygen content, a greater density of void embryos are stabilized against

collapse, as postulated in Chapter 3. On the average, the arrival rate of vacancies at an individual subcritical vacancy cluster is lower than for specimens with lower gas levels. This requires the accumulation of a greater dose before a typical cluster reaches critical size. This argument is similar to that of Lee and Mansur [12] for helium dilution by fine precipitate populations. Helium bubbles often accumulate at precipitates in stainless steels. When a high density of small precipitates can be maintained, a high density of fine helium bubbles can be obtained rather than coarse voids [12-14], resulting in a significant suppression of swelling. Lee and Mansur [12] argue that the increase in helium sinks reduces the probability that any particular gas bubble will accumulate a critical number of gas atoms for spontaneous growth.

For the case of oxygen preimplantation in this study, it is probable that the void suppressed region in the implanted zone probably contains a high density of sub-critical void embryos. It is possible that a high density of voids exist but are below the resolution limit of the microscope. One way to resolve this question might be by positron annihilation experiments.

C. Evaluation of the Uniformity of the End-of-Range

As noted in the previous chapter, several inconsistencies in the data are eliminated when the end of the void swelling region in every sample is assumed to occur at a single depth. The uncorrected data shows a variation in this end depth because of sample to sample

differences in the amount of surface material removed during post-irradiation handling. The validity of this assumption is considered below.

The target material and the bombarding species and energy used in this study are the same for all samples. As noted in Chapter 2, these are the variables used to determine ion range and stopping power. Further, there is no theoretical or empirical evidence that the ion range will vary over the temperature range (550 to 650°C) investigated. It has been suggested that there can be an extension in the damage range with increasing ion fluence [15]. However, the fluence is identical in all the irradiations in this thesis.

Another factor which can increase the ion range is the density changes due to swelling [16,17]. One study [16] examined the effect of swelling on ion range when the density change is averaged over the entire swelling range, while another [17] considered the discrete nature of the voids. In order to determine the extent that swelling affects range in this thesis, the sample that showed the greatest swelling, the 600°C uninjected sample, is considered. Using the average density change model, the ion range is calculated to increase by about 0.04 μm. The discrete-density change model yields an increase in ion range of less than 0.1 μm. These results along with the previous discussion lead to the conclusion that the ion range and damage profile in all the samples should be the same.

The fact that the ion range and damage profile are identical does not necessarily indicate that the swelling profile will be the

same. Certainly it is true that some samples show different swelling response near the surface and in the oxygen injected region. However, these differences in the void formation behavior are attributable to the existence of the surface or the injected oxygen. At the damage peak and beyond there are no surfaces or injected oxygen to affect the swelling behavior. It is energetically possible that knock-ons from the injected oxygen may be scattered into the peak damage region and beyond. If this possibility represents the actual case, the void bearing region should systematically widen with increasing oxygen content at constant temperature due to the increasing probability of an oxygen knock-on occurring. Table 6.3 indicates that this is not the case. The only variable between samples that is operative near the peak damage region is the difference in temperature.

As stated earlier, there is no evidence that there is an effect on the ion range or damage profile over such a limited temperature range as 550 to 650°C. However, there may be an effect on the swelling response at the end of range. Clearly the temperature range 550 to 650°C is completely within the swelling regime of this alloy, as the existence of voids at all temperatures indicates. However, at the peak damage region and beyond, the injected ions come to rest at interstitial sites. These injected interstitials may suppress void nucleation [2,18-20] and growth rate [21-22]. Void suppression by the injected interstitials is greatest where point defect recombination is dominant, which is at lower temperatures. Both theory [2]

and experiment [2,20] indicate that there is no injected interstitial suppression of void nucleation in type 316 austenitic stainless steel at temperatures ≥ 550°C. Therefore, it is concluded that none of the differences in the end of the void swelling region can be attributed to the temperature.

The previous discussion shows that the variation in the depth at which void formation ceases is not attributable to dose, dose rate, swelling, or temperature. As Figure 2.1b reveals, a significant dose is accumulated (~ 15 dpa) beyond the oxygen implanted zone and in all but one case, the 10 appm O implanted 550°C irradiated sample, voids occur beyond the oxygen injected region. As noted in Chapter 6, this sample has about 0.4 μm removed during the post-irradiation electroplating, twice the amount removed from the other samples. This indicates that voids occur at and beyond the peak damage zone, regardless of the injected oxygen, as expected. In all the samples irradiated in this study, the damage profile should be identical. Therefore, it appears valid to assume that the depth at which void formation ends should be the same in all cases in this study.

Acceptance of this assumption leads to a re-evaluation of the data, as indicated in Table 6.4. When the void swelling data is adjusted for the different amounts of surface material removed during post-irradiation specimen preparation, several trends emerge. These trends do not rely on the second assumption made in Chapter 6. This second assumption is that the depth at which void formation ends corresponds to the calculated end of range. This second assumption

appears to provide a reasonable estimate of the true depth at which the voids end.

Because the model used to calculate the damage profile is a Monte-Carlo based approach which follows 1000 histories, the predictions should be relatively accurate. This model shows a rapid decrease in damage at depths beyond the damage peak. As Figure 2.1a indicates, about the same damage level occurs at 2.6 μm as occurs at a depth of 1 μm. The end of range occurs at 2.7 μm. Therefore, if voids form at 1 μm in the as-treated material, it is reasonable to expect voids to form at 2.6 μm but not to form beyond 2.7 μm.

Further arguments in favor of the second assumption which equates the end of range with the end of the void formation region involve the success of predictions based on the calculated damage profile with experiment. As noted in Chapter 6, utilization of this second assumption shows that the maximum void diameter occurs within 0.2 μm of the depth at which the damage peaks for all cases in this study. Also, the depth at which the maximum void density or the void suppressed region occurs in the oxygen implanted specimens is within 0.3 μm of the peak of the oxygen deposition region. Finally, the near-surface void free zone becomes a systematic function of temperature only. Therefore, it appears reasonable to assume not only that the end of the void swelling region in all samples is identical but also that the end of this region corresponds to end of range.

D. Comparison of Experimental Results to Theory

The theory developed in Chapter 3 illustrates how oxygen affects void stability. This stability is achieved by oxygen adsorption onto the surface of the void embryos in contrast to helium effects, where bubbles form and convert to voids after a critical number of gas atoms accumulate. The theoretically determined levels of oxygen needed for stabilization of the entire terminal void density as a function of temperature are given in Figure 3.2. From 550 to 650°C, the minimum concentration required is calculated to be about 5 appm of atomic oxygen.

It is very difficult to achieve a level of residual oxygen lower than this in a pure Fe-Ni-Cr ternary. In order to lower the oxygen contents of steel, elements such as Si, C, P, Al, or Ti are normally added to the melt. The alloy used in this study contains an aluminum addition of about 30 wppm in an attempt to getter the residual oxygen without perturbing the alloy system. Unfortunately, the majority of aluminum seems to reside in inclusions rather than in solution, as noted in Chapter 6. Therefore, it would appear that not all of the 160 appm residual oxygen is bound by the aluminum. Thus a high void density is expected to occur in the unimplanted alloy if the model of Chapter 3 is quantitatively accurate.

The oxygen levels calculated in the model are for unbound oxygen interstitials that are free to diffuse. As stated earlier, oxygen in the as-treated alloy may also be bound at grain boundaries and internal oxides. Indirect evidence for assuming that this is the

case is the response of the alloy to irradiation when 10 appm O is preimplanted. The calculated terminal void density at 550°C is about $1x10^{22}/m^3$ for dose rate of 10^{-3} dpa/sec. The maximum void density in the 10 appm O injected specimen was measured to be about $3x10^{21}/m^3$. When no oxygen is implanted the void density at 550°C is about $7x10^{20}/m^3$. The addition of 10 appm of 'free' O to 160 appm of residual O results in a four-fold increase in void number density. The magnitude of this increase can only be attributed to the nature of the oxygen. And the fact that only 10 appm O is required indicates that the model developed in Chapter 3 provides relatively good quantitative results.

It may be argued that the injected oxygen produces damage, which is responsible for the increase in void nucleation. The injected oxygen produces a peak damage of about $6x10^{-4}$ dpa/appm. This is quite small compared to the damage done by the Ni irradiation. Furthermore, after implantation but before irradiation each sample was held at about 300°C for several hours, in vacuum, due to residual heating in the target chamber. This temperature corresponds to Stage III of recovery in this alloy, so that the vacancies as well as interstitials could migrate to sinks. However, at this temperature the oxygen is immobile. Further evidence that the oxygen is the main cause, rather than the damage done by implantation, is the fact that the near-surface void denuded zone decreases with temperature. If the damage done during implantation was responsible for the increased void density, then there should be no effect of temperature on the

extent of this zone because all implantations occurred at room temperature. The fact that the void denuded zone at the surface decreases with temperature indicates that it is the oxygen which is promoting void stability, as discussed earlier.

One conclusion of the model is that in austenitic steel void embryos will collapse to loops in the absence of gas. This conclusion remains unproven by this study. Other aspects of the model do seem to predict the experimental results. A low concentration of unbound oxygen will result in a high observed void density. No bubbles are observed up to 330,000 X. Overall, the experimental results agree with the model.

References for Chapter 7

1. K. Farrell and N.H. Packan, "Comparison of Neutron and Heavy-Ion Damage in a Single Phase Austenite," in Effects of Radiation on Materials: Eleventh Conference, ASTM STP 782 (1982) 906-916.
2. B. Badger, Jr., D.L. Plumton, S.J. Zinkle, R.L. Sindelar, G.L. Kulcinski, R.A. Dodd, and W.G. Wolfer, "Experimental Investigation of the Effect of Injected Interstitials on Void Formation," in Effects of Radiation on Materials: Twelfth International Symposium, ASTM STP 870 (1985) 297-316.
3. J.H. Swisher and E.T. Turkdogan, Trans. Met. Soc. AIME 239 (1967) 426-431.

4. M.F. Wehner and W.G. Wolfer, Phil. Mag. A 52 (1985) 189-205.

5. L.K. Mansur, Nucl. Tech. 40 (1978) 5-34.

6. F.A. Garner and L.E. Thomas, "Production of Voids in Stainless Steels by High-Voltage Electrons," in Effects of Radiation on Substructure and Mechanical Properties of Metals and Alloys, ASTM STP 529 (1973) 303-325.

7. D.B. Bullen, "The Effects of Implanted Hydrogen and Helium on Cavity Formation in Self-Ion Irradiated Nickel," Ph.D. Thesis, University of Wisconsin-Madison (1984).

8. L.M. Wang, R.A. Dodd, and G.L. Kulcinski, J. Nucl. Mat. 141-143 (1986) 713-717.

9. H. Ullmaier, Nucl. Fus. 24 (1984) 1039-1083.

10. S.C. Agarwal, D.I. Potter, and A. Taylor, Met. Trans. A 9 (1978) 569-576.

11. M.S. Wechsler and R.E. Foster, J. Nucl. Mat. 83 (1979) 160-165.

12. E.H. Lee and L.K. Mansur, J. Nucl. Mat 141-143 (1986) 695-702.

13. P.J. Maziasz and T.K. Roche, J. Nucl. Mat. 103 & 104 (1981) 797-802.

14. M.P. Shaw, B. Ralph, and W.M. Stobbs, J. Nucl. Mat 115 (1983) 1-10.

15. L.M. Wang and S. H. Han, private communication.

16. W.G. Wolfer and M.E. Benchick-Lehocine, "The Effect of Density Changes on the Energy and Ion Deposition Profiles," in Damage Analysis and Fundamental Studies, DOE/ER-0046/21 (1985) 130-133.

17. R.L. Sindelar, S.N. Farrens, and G.L. Kulcinski, "Effects of Cavitation on Damage Calculations in Ion-Irradiated P7 Alloys," in Damage Analysis and Fundamental Studies, DOE/ER-0046/22 (1985) 39-47.

18. F.A. Garner, J. Nucl. Mat. 117 (1983) 177-197.

19. D.L. Plumton and W.G. Wolfer, J. Nucl. Mat. 120 (1984) 245-253.

20. R.L. Sindelar, "A Comparison of the Response of 316 SS and the P7 Alloy to Heavy-Ion Irradiation," Ph.D. Thesis, University of Wisconsin-Madison (1985).

21. A.D. Brailsford and L.K. Mansur, J. Nucl. Mat. 71 (1977) 110-116.

22. E.H. Lee, L.K. Mansur, and M.H. Yoo, J. Nucl. Mat. 85 & 86 (1979) 577-581.

CHAPTER 8

CONCLUSIONS

A model has been developed and tested to examine the effect oxygen has on void swelling in irradiated materials. The model is based on a comparison of thermodynamic stability of vacancy cluster species, an examination of oxygen atom partitioning, and the ability of oxygen to chemisorb and thus alter the void surface energy. The conclusions to be drawn from the model are listed below.

1) Voids are calculated to be thermodynamically unstable in "Pure" 316 austenitic stainless steel.
2) Voids are calculated to be thermodynamically stable when the surface energy is lowered to 1.0 J/m^2.
3) The calculated driving force for the decrease in surface energy is the adsorption of a monolayer of oxygen to the surface of a void embryo.
4) Oxygen partitioning calculations indicate that an initial concentration of 4 to 5 appm oxygen in solution is capable of stabilizing a high density of voids (~ $10^{22}/m^3$) at 550 to 650°C.

An Fe-17Ni-13Cr alloy has been irradiated with 15 MeV nickel ions in order to test these conclusions. The alloy was irradiated at 550, 600 and 650°C. Some samples were preinjected with oxygen at room temperature to concentrations of 10, 100, 300 and 1000 appm O. The irradiated specimens were examined in cross-section in order to

study the entire damage and preinjected ranges. The following conclusions can be drawn from this experiment.

1) Preimplanting oxygen significantly affects the swelling response of the Fe-17Ni-Cr steel.

When no oxygen is preinjected:

2) Void density increases then decreases as temperature increases. This may be due to competion between decreasing terminal void nucleation densities and increasing oxygen detrapping.
3) Void diameter is not a systematic function of temperature.
4) The near-surface void denuded zone width increases with increasing temperature.

When oxygen is preinjected:

5) Void density is more a function of injected oxygen level rather than of temperature.
6) Void diameter is independent of injected oxygen concentration but, instead, depends on temperature in a classical manner.
7) Void formation is suppressed when 300 appm of oxygen or greater is preinjected. The suppression is probably due to an increase in the density of vacancy sinks.
8) The near-surface void denuded zone width decreases with increasing temperature. This decrease is probably due to oxygen diffusing from the implanted zone as the temperature increases.

9) As little as 10 appm preinjected oxygen can significantly affect void nucleation, even when the residual oxygen concentration is 160 appm.

Unfortunately, the contention that voids cannot form in a pure ternary steel in the absence of gas is not proven in this experiment. Lowering the residual gas content to less than 1 appm without the addition of significant solute concentrations has not yet been achieved. This capability to lower the residual gas contents without impurity additions is more likely in pure metals such as copper or nickel.

The model presented here can be more definitively tested in pure metals than in an alloy such as 316 SS.